

# Ultrasound Control and Imaging of Cellular Immunotherapy

Thesis by  
Justin Lee

In Partial Fulfillment of the Requirements for  
the Degree of  
Doctor of Philosophy in Bioengineering

The Caltech logo, featuring the word "Caltech" in a bold, orange, sans-serif font, centered within a light orange rectangular background.

CALIFORNIA INSTITUTE OF TECHNOLOGY  
Pasadena, California

2024  
(Defended August 08, 2023)

© 2024

Justin Lee

ORCID: 0000-0002-3657-4386

## ACKNOWLEDGEMENTS

First and foremost, I would like to thank my PhD advisor, Mikhail Shapiro, for welcoming me into his lab and guiding me throughout my graduate training. When I first began my MD/PhD training at UCLA, I was not supposed to conduct any part of my training at Caltech. But I found out about Mikhail's research which connected so well with my clinical interests, and I reached out to plan a summer rotation thinking I would eventually return to UCLA to complete my PhD. I could not have anticipated how much I would resonate with the research and the people within the lab. Perhaps most importantly, during my rotation, Mikhail was so generous with his time to teach me and cultivate new ideas with me, I knew I wanted to join his lab. He personally wrote a letter to the MD/PhD program directors asking their permission for me to train with him, and I will forever be thankful for his support. This gesture was a sign for things to come, as throughout my training, Mikhail was always available to help with fellowship applications or to discuss career planning and thoughts about life more broadly. His constant encouragement still amazes me, and I find myself aspiring to be more like him, both as a scientist and as a person.

I would also like to thank all the brilliant people I have had the privilege of learning from and working with in the Shapiro lab. Arash Farhadi and Mohamad Abedi were my two first mentors in lab, and they taught me foundational skills that I used throughout my PhD. Mohamad inspired me to apply for the PD Soros Fellowship, and I am forever thankful for how much he changed my life for the better. Bill Ling, Ernesto Criado-Hidalgo, Zhiyang Jin, Ann Liu, Kaiwen Luo, and Tom Duan were wonderful peers and collaborators whose input are seen throughout the projects I undertook. Shirin Shivaie also generously shared lentiviral constructs critical for gas vesicle expression in THP-1 cells. Mei Yi was an amazing

undergrad I had the privilege of mentoring. Erik Schrunk, Yuxing Yao, Claire Rabut, Cameron Smith, and Abdullah Farooq, thank you for being amazing friends. Lab would not have been the same environment without you. Ruby Zhang, Peirina Barturen, Rosie Zedan, and Margaret Swift are some of the most amazing lab technicians/managers I have ever worked with, and the lab truly would not run without them.

I am also so grateful for all the mentorship from Jeremy Chae, who was my graduate student mentor, when I was just starting biomedical research as an undergrad. I am also so thankful for previous research advisors, Professors Jennifer Elisseeff and Ben Park who both inspired me to embark on this journey to train as a physician-scientist and showed me the potential in understanding both medicine and research.

I would also like to express my deepest gratitude for my family. It was a privilege to train in Pasadena, where I grew up, near my parents and siblings. Their constant love and unwavering support fueled me during the challenging parts of my training. My family has been an incredible source of joy in my life, and I will always be grateful for my parents, sisters, brother-in-laws, and nephews.

Most importantly, I am so thankful for Hannah, my best friend and loving wife. Thank you for being my balance. Your kindness and patience amaze me to this day. I am inspired by how deeply you care for others. You have helped me put so many things into perspective. It is hard to be negative when I see you extending your love and happiness to those around you. I am so thankful for your unending encouragement. It is hard to imagine going through my training without you, and I am so excited to continue our journey through life together with all its ups and downs.

## ABSTRACT

Biomedical ultrasound-based therapeutics and diagnostics are becoming an increasingly important clinical tool. Techniques like focused ultrasound tissue heating and microbubble-enhanced ultrasound imaging have enabled new ways to noninvasively treat and detect diseases cost-effectively and safely. While these are great leaps forward in ultrasound technology, leveraging synthetic biology tools to engineer cells with the capabilities to interact with ultrasound in novel ways may enable even more avenues for ultrasound to address important clinical challenges.

In this thesis, we explore the potential in engineering immune cells with various genetic elements which interact with either therapeutic or diagnostic ultrasound in novel ways. In Chapter 2, we engineer T-cells capable of sensing increases in temperature and responding by activating expression of therapeutic proteins to potentially increase safety of cell-based immunotherapies by controlling their spatiotemporal activation. In Chapters 3 and 4, we develop monocytes as ultrasound reporter cells for cancer detection by engineering them to express gas vesicles (GVs), a class of air-filled protein nanostructures natively found in certain aquatic microbes, which have been demonstrated to produce ultrasound contrast. We demonstrate the potential to confine GV expression to certain disease related signals to create ultrasound reporter cells. Together, these findings highlight the potential of engineering cells to activate in certain locations in response to ultrasound heating or serve as sentinel cells for disease detection.

## PUBLISHED CONTENT AND CONTRIBUTIONS

Abedi, M.H., **Lee, J.**, Piraner, D.I., Shapiro, M.G. Thermal Control of Engineered T-cells. *ACS Synthetic Biology* 9, 8, 1941-1950 (2020) doi: 10.1021/acssynbio.0c00238

J.L. conducted experiments evaluating pHSP candidates in primary T-cells, characterizing optimal parameters for activation, assisted in developed genetic circuits for sustained thermal activation, developed temperature activated cytokine release, characterized auto sustained thermally induced CAR expression, in addition to analyzing data, and assisting in manuscript preparation.

Ling, B., **Lee, J.**, Maresca, D., Lee-Gosselin, A., Malounda, D., Swift, M.B., Shapiro, M.G. Biomolecular Ultrasound Imaging of Phagolysosomal Function. *ACS Nano* 14, 12210-12221 (2020). doi: 10.1021/acsnano.0c05912

J. L. conducted experiments labeling gas vesicles, internalizing them within macrophages, tracking phagocytosed gas vesicle, imaging internalized gas vesicles in macrophages using ultrasound, in addition to analyzing data, and assisting in manuscript preparation.

## TABLE OF CONTENTS

Acknowledgements .....	iii
Abstract .....	v
Published Content and Contributions .....	vi
Table of Contents .....	vii
List of Illustrations .....	ix
List of Tables.....	xi
Chapter I: Synthetic Biology Techniques to Expand	
the Capabilities of Ultrasound Therapeutics and Diagnostics .....	1
1.1 Introduction.....	1
1.2 Therapeutic Ultrasound .....	1
1.3 Developing Heat-Sensitive Immunotherapies.....	2
1.4 Diagnostic Ultrasound .....	4
1.5 Macrophages as Ultrasound Reporter Cells for Cancer Detection .....	6
1.6 Synergies between Ultrasound and Synthetic Biology .....	8
Chapter II: Thermal Control of Engineered T-cells.....	
2.1 Introduction.....	12
2.2 Results .....	14
2.3 Discussion .....	28
2.4 Methods.....	29
2.5 Supplementary Information.....	32
2.6 References .....	35
Chapter III: Biomolecular Ultrasound Imaging of Phagolysosomal Function ..	
3.1 Abstract .....	39
3.2 Introduction.....	40
3.2 Results and Discussion .....	43
3.3 Conclusion .....	56
3.4 Methods.....	58

3.5 Supplementary Information .....	66
3.6 References .....	74
Chapter IV: Engineering Monocytes as Ultrasound Reporter Cells for Cancer Detection.....	78
4.1 Introduction .....	78
4.2 Results .....	79
4.3 Discussion .....	91
4.4 Methods.....	92
4.5 Supplementary Information .....	96
4.6 References .....	102
Chapter V: Conclusions and Future Directions.....	104
5.1 Genetic Circuit Design Consideration.....	105
5.2 Cost Considerations for Adoptive Cell Transfer.....	106
5.3 Future Directions for Monocyte-based Ultrasound Reporter Cells ...	107

## LIST OF ILLUSTRATIONS

<i>Number</i>	<i>Page</i>
2-1 Evaluating candidate pHSPs in primary T-cells .....	15
2-2 Thermal parameters for pHSP activation in human T-cells.....	17
2-3 Genetic Circuits for amplified and sustained thermal activation.....	20
2-4 Temperature-activated cytokine release.....	23
2-5 Dependence on pHSP-driven circuits on T-cell activation.....	25
2-6 Auto-sustained thermally induced tumor cell killing.....	27
2-S1 Thermally induced shift in gene expression .....	32
2-S2 Expression of a transduction marker to control for variability.....	32
2-S3 Bait cell count for the HSP CAR killing experiment .....	33
2-S4 CAR expression from constitutive and induced constructs.....	33
2-S5 Assessing the proliferative capacity of stimulated T-cells .....	34
2-S6 Thermally induced CAR expression.....	34
3-1 Ultrasound imaging of GV clearance and elimination .....	44
3-2 Liver uptake of GVs .....	47
3-3 Lysosomal degradation of GVs .....	50
3-4 Pharmacokinetic modeling.....	52
3-5 Diagnostics by imaging phagolysosomal function .....	55
3-S1 Circulation half-life .....	66
3-S2 Ultrasound contrast in C57BL/6 mice .....	66
3-S3 Image segmentation with ilastik .....	67
3-S4 Ultrasound contrast vs. GV concentration.....	68
3-S5 Time courses for pharmacokinetic fitting.....	69
3-S6 Macrophage counting workflow .....	70
3-S7 GV uptake by LSEC.....	71
3-S8 Liver clearance saturation .....	71

3-S9 Influence of age on pharmacokinetic parameters .....	72
4-1 Optimizing GV expression in THP-1 cells .....	80
4-2 Migration potential following GV expression .....	82
4-3 Macrophage GV expression and phagocytosis .....	85
4-4 Hypoxia induced GV expression .....	87
4-5 Antigen induced GV expression .....	90
4-S1 Lentiviral Stoichiometry and transduction efficiency .....	96
4-S2 Lentiviral Stoichiometry and GV expression .....	97
4-S3 THP-1 viability during GV expression .....	98
4-S4 Kinetics of GV expression .....	98
4-S5 GV clusters visible via light microscopy .....	99
4-S6 Phagocytosed bead distance to nearest membrane .....	99
4-S7 Effects of hypoxia on GV expression .....	100
4-S8 Optimization of antiCD19-synNotch induction.....	101

## LIST OF TABLES

<i>Number</i>	<i>Page</i>
Table 3-S1 Pharmacokinetic constants.....	73
Table 4-S1 THP-1 cell migration cell counts.....	99

*Chapter 1***SYNTHETIC BIOLOGY TECHNIQUES TO EXPAND THE  
CAPABILITIES OF ULTRASOUND THERAPEUTICS AND  
DIAGNOSTICS****1.1 Introduction**

Biomedical ultrasound is an essential clinical tool and has enabled clinicians to noninvasively diagnose and treat a range of conditions.<sup>1</sup> By employing sound waves at frequencies above those audible to humans (>20,000 Hz), ultrasound interacts with biological tissue in real time safely and precisely.<sup>2</sup> Diagnostic and therapeutic ultrasound represent two distinct capabilities of biomedical ultrasound, but further expanding the capabilities of both ultrasound modalities will require innovations in synthetic biology and molecular imaging.<sup>3</sup> In this chapter, we provide an overview of the fundamental principles underlying biomedical ultrasound and introduce synthetic biology technologies that synergize with ultrasound techniques to expand their potential in treating and diagnosing disease.

**1.2 Therapeutic Ultrasound**

While ultrasound is often thought of as an imaging modality, ultrasounds are mechanical acoustic waves which can induce both thermal and mechanical effects in the body.<sup>4</sup> Part of the ultrasonic energy is absorbed by tissue which is dissipated as heat, or the wave can deposit momentum into mediums resulting in mechanical forces known as acoustic radiation forces.<sup>5</sup> Ultrasonic energy can be focused at a single point in tissue, and high intensity focused

ultrasound (HIFU) can result in a rapid temperature rise in tissues to 60°C.<sup>6</sup> Clinically, HIFU procedures have been used for therapies like tissue thermal ablation and neuromodulation.<sup>7-9</sup> Its non-invasive nature, low-cost, and reduced toxicity when compared to other ablation modalities has increased the use of therapeutic ultrasound. However, focused ultrasound can also enable spatiotemporal control of heating to non-ablative temperatures around 42°C which can be used as a method for non-invasively actuating cells which has the potential to improve safety of current immunotherapies.<sup>10,11</sup>

### **1.3 Developing Heat-Sensitive Immunotherapies**

Engineered cell-based therapies have shown great promise in improving health outcomes.<sup>12</sup> Adoptive T-cell therapy is a new class of non-invasive immunotherapies where T-cells are harvested from patients' blood, expanded, and engineered with chimeric antigen receptor (CAR) which are reinfused into patients to seek and destroy cancer cells.<sup>13</sup> By leveraging the molecular specificity of CAR engagement to cancer antigen, CAR T-cells have shown significant potential in irradiating hematologic malignancy where traditional therapies like surgery, radiation, and chemotherapies have fallen short.<sup>14</sup>

CAR T-cells have cured patients of blood-based malignancy and immunotherapies in general have emerged as a fourth pillar of cancer therapies. However, the molecular specificity and robust cancer cell killing has leveraged a crucial advantage when treating B-cell malignancies: B-cells are the only cells in the human body which express the extracellular CD19 antigen, and every B-cell expresses this antigen.<sup>15</sup> Furthermore, even if B-cells are completely irradiated, humans can replace a part of their function through regular immunoglobulin injection.<sup>16</sup> When CAR T-cells have been developed for solid tumor

treatment, unlike the CD19 antigen in B-cell cancer, there are no antigen targets constrained specifically to the tumor that are expressed throughout the tumor tissue.<sup>17</sup> As a result, CARs targeting antigen which are overexpressed in the tumor have been used in the hopes that CARs will naturally target cells with the highest concentration of antigen, but off-target effects using this strategy have resulted in significant adverse events in patient, including death.<sup>18</sup>

Unfortunately, the advantage of immune cells naturally seeking cancer cells for cell-mediated tumor cell killing decreases the level of control a physician has on this therapy once it is infused into the patient. Researchers have used synthetic biology tools to create systems requiring engagement of multiple tumor associated antigens to reduce the potential for runaway off-target activation against healthy tissue, but off-target activation is not the only parameter of importance in solid tumor treatment.<sup>19</sup> CAR T-cells also face an immunosuppressive environment where T-cell inactivation and exhaustion becomes more likely. Decreasing CAR T-cell killing efficacy by requiring multiple activation inputs may not be optimal.

As a result, maintaining tumor killing potential, but constraining activation to certain locations may be beneficial in solid tumor treatment. In order to control cell behavior once engineered cells are in the body, methods like optogenetics achieve precise temporal control, but require invasive procedures to reach deep tissue.<sup>20</sup> Unlike photons which are scattered on the millimeter scale of tissue, ultrasound waves are capable of targeting deep tissue while maintaining spatial and temporal coherence.<sup>21</sup> In order to take advantage of the benefits of therapeutic ultrasound, synthetic biology tools which confer the ability for cells to respond to gentle tissue heating may enable spatiotemporal, noninvasive control of adoptive therapies

to improve safety *in vivo*, and we will develop thermally sensitive primary T-cells which are capable of specifically expression a therapeutic protein payload upon thermal stimulation, which will be highlighted in Chapter 2.

## 1.4 Diagnostic Ultrasound

Ultrasound imaging is a well-established medical imaging technique that utilizes ultrasonic waves to provide real-time, quantitative anatomical and physical information of internal body structures.<sup>22</sup> It relies on a pulse-echo principle, where a piezoelectric ultrasound transducer emits soundwaves at frequencies greater than 1MHz towards the issue of interest.<sup>2</sup> The pulses are partially reflected by tissues and some reflections return to the transducer. Sound waves are strongly reflected when there are acoustic impedance changes, for example at organ boundaries, while smaller structures like cells and extracellular matrix produce weak reflections. The returning echoes are converted to electrical pulses which are processed and reconstructed into a digital image.<sup>23</sup>

Various imaging modes, probe, and machine settings have increased the clinical utility of ultrasound. B-mode imaging, the most common modality method, utilizes an array of transducer elements to scan a plane through tissue which results in a two-dimensional image. In this mode, pixel values correspond to the backscattered signal's voltage amplitude.<sup>24</sup> Nonlinear imaging modes like amplitude modulation and pulse inversion amplify higher frequency components of the backscattered imaging which helps distinguish contrast agents from surrounding tissues which are often linear scatterers.<sup>25,26</sup> Doppler imaging measures the frequency shift of returning echoes when the medium of interest, like

blood, is moving towards or away from the transducer.<sup>27</sup> This has enabled visualization of vasculature and quantification of blood flow dynamics.

In addition to the various imaging modes, contrast agents have been developed to improve ultrasound imaging functionality. Gas-filled microbubbles have been particularly useful as ultrasound contrast agents due to the large difference in acoustic impedance between gas and surrounding tissue and their ability to produce nonlinear echoes due to their compressibility when interacting with ultrasound waves.<sup>28</sup> These microbubbles have been used systemically to image pathology ranging from atherosclerosis and aneurysm formation to risk stratification of myocardial infarction and stroke.<sup>29-31</sup> They are also being developed for additional application like tumor vasculature imaging.<sup>32</sup>

While microbubbles have great utility when imaging the vascular system and related tissues, an entirely new application space would be opened with the capability of in situ production of ultrasound contrast. Gas vesicles (GVs) are genetically encoded air-filled protein nanostructures which have emerged as a next-generation ultrasound contrast agent. GV's are produced natively by aquatic microbes to regulate buoyancy in the water column and thus access to light for photosynthesis.<sup>33</sup> These protein nanostructures take advantage of a highly hydrophobic internal surface which allows gas exchange but prevents condensation which creates a stable pocket of air of approximately 250nm. Importantly, the air-liquid interface produced by these GV's strongly scatter ultrasound waves and produce ultrasound contrast.<sup>34</sup>

As these proteins are genetically encoded, significant work has gone towards producing GV's in both nonnative bacteria and mammalian cells.<sup>35-37</sup> In addition, to expanding the repertoire of potential chassis to produce gas vesicles, there have been

advances in the application of GVs. New ultrasound pulse sequences have been developed to detect GVs by relying on unique GV properties like protein shell buckling and collapse which produces nonlinear ultrasound echoes.<sup>25,38</sup> GVs have enabled the development of ultrasound reporter cells which may produce ultrasound contrast in response to certain pathologies like cancer, which will be illustrated in the following section.

### **1.5 Macrophages as Ultrasound Reporter Cells for Cancer Detection**

Early disease detection generally results in improved health outcomes, and there has been significant investment into developing improved diagnostic methods. This has been especially important for diseases like cancer where ~50% of patients are diagnosed at an advanced stage where disease burden is greater and remission is less likely.<sup>39</sup> Public health initiatives including screening recommendations for mammography have improved early detection of breast cancer, but tumor size remains a limiting factor on imaging: some cancers will not be visible on mammography until they reach >70mm.<sup>40</sup>

To address these challenges, there has been significant focus in two novel classes of cancer screening tools including endogenous biomarkers and systemically administered cancer-sensitive probes. Endogenous biomarkers like circulating tumor DNA and cells can now be detected using next generation PCR techniques, but these endogenous biomarkers exist in low circulating concentrations and have a short half-life in blood.<sup>41</sup> Probes that specifically interact with proteases in the tumor microenvironment face difficulties trafficking to solid tumors due to dysregulated tumor vasculature and also face challenges in

off-target activation—while tumor microenvironments overexpress certain proteases, they are also found in normal tissue throughout the body.<sup>42</sup>

Unlike these previously described technologies, certain immune cells, specifically monocytes, actively migrate to solid tumors where they take residence and perform both anti- and pro-tumorigenic functions.<sup>43</sup> Furthermore, monocytes and the macrophages they differentiate into are capable of sensing the tumor microenvironment, and through natural secondary signal cascade or synthetic gene amplifiers, are capable of amplifying these signals into distinct cellular responses.<sup>44</sup> This ability to migrate and amplify tumor signals have been leveraged to develop murine macrophages as a potential tool for early cancer detection, but the previous studies used bioluminescence as the reporter of choice.<sup>45</sup> While this protein output is useful for imaging in smaller model organisms like mice, due to the scattering of light by tissue, our goal is to develop a cancer-sensing ultrasound reporter using a human monocytic cell line as a model system.

Initial attempts to develop a macrophage ultrasound reporter are highlighted in Chapter 3. We developed a method to leverage macrophage phagocytosis of GVs and demonstrated ultrasound contrast produced by GVs within macrophages following phagocytosis. However, due to the nature of the phagolysosomal system, phagocytosed GVs were quickly degraded, and ultrasound contrast production was subsequently lost. Attempts to delay GV degradation in the lysosome reduced cell viability, but this phenomenon was instead used as a marker for *in vivo* liver function. While GV loading into macrophages was not effective as a cell-based reporter system, we leveraged the ability for mammalian cells to express GV through transduction of monocytes with GV transgenes, characterized cell

phenotype following GV expression, and through transcriptional control, tethered GV expression to cancer associated signals.

## 1.6 Synergies between Ultrasound and Synthetic Biology

This thesis will investigate how synthetic biology techniques can unlock new methods of interacting with both therapeutic and diagnostic ultrasound. First by exploring how developing heat shock promoter-based genetic circuits enables the control of primary T-cells through ultrasound heating and then exploring how GVs can be utilized to non-invasively image cells in the body through either loading of cells with GV or intracellular production via mARG expression. Our objective is to better understand how synthetic biology can unlock novel ways to leverage the benefits of ultrasound and in doing so, address important translational challenges including controlling adoptive therapies *in vivo* to improve safety, and using engineered immune cells to develop a platform for cancer-activated ultrasound reporter cells.

## References

1. Carovac, A., Smajlovic, F. & Junuzovic, D. Application of Ultrasound in Medicine. *Acta Inform. Medica* **19**, 168–171 (2011).
2. Abu-Zidan, F. M., Hefny, A. F. & Corr, P. Clinical ultrasound physics. *J. Emerg. Trauma Shock* **4**, 501–503 (2011).
3. Suri, J. S. *Advances in Diagnostic and Therapeutic Ultrasound Imaging*. (Artech House, 2008).
4. ter Haar, G. Therapeutic applications of ultrasound. *Prog. Biophys. Mol. Biol.* **93**, 111–129 (2007).
5. Miller, D. *et al.* Overview of Therapeutic Ultrasound Applications and Safety Considerations. *J. Ultrasound Med. Off. J. Am. Inst. Ultrasound Med.* **31**, 623–634 (2012).
6. Izadifar, Z., Izadifar, Z., Chapman, D. & Babyn, P. An Introduction to High Intensity Focused Ultrasound: Systematic Review on Principles, Devices, and Clinical Applications. *J. Clin. Med.* **9**, 460 (2020).

7. Haar, G. T. & Coussios, C. High intensity focused ultrasound: physical principles and devices. *Int. J. Hyperther. Off. J. Eur. Soc. Hyperthermic Oncol. North Am. Hyperther. Group* **23**, 89–104 (2007).
8. Fry, W. J., Mosberg, W. H., Barnard, J. W. & Fry, F. J. Production of focal destructive lesions in the central nervous system with ultrasound. *J. Neurosurg.* **11**, 471–478 (1954).
9. Kubanek, J. Neuromodulation with transcranial focused ultrasound. *Neurosurg. Focus* **44**, E14 (2018).
10. Abedi, M. H., Lee, J., Piraner, D. I. & Shapiro, M. G. Thermal Control of Engineered T-cells. *ACS Synth. Biol.* **9**, 1941–1950 (2020).
11. Miller, I. C., Gamboa Castro, M., Maenza, J., Weis, J. P. & Kwong, G. A. Remote Control of Mammalian Cells with Heat-Triggered Gene Switches and Photothermal Pulse Trains. *ACS Synth. Biol.* **7**, 1167–1173 (2018).
12. Weber, E. W., Maus, M. V. & Mackall, C. L. The Emerging Landscape of Immune Cell Therapies. *Cell* **181**, 46–62 (2020).
13. June, C. H. & Sadelain, M. Chimeric Antigen Receptor Therapy. *N. Engl. J. Med.* **379**, 64–73 (2018).
14. Five-Year Outcomes for Refractory B-Cell Lymphomas with CAR T-Cell Therapy | NEJM. <https://www.nejm.org/doi/full/10.1056/nejmc2030164>.
15. Chen, G. M., Melenhorst, J. J. & Tan, K. B cell targeting in CAR T cell therapy: Side effect or driver of CAR T cell function? *Sci. Transl. Med.* **14**, eabn3353 (2022).
16. Hill, J. A., Giralt, S., Torgerson, T. R. & Lazarus, H. M. CAR-T– and a side order of IgG, to go? – Immunoglobulin Replacement in Patients Receiving CAR-T Cell Therapy. *Blood Rev.* **38**, 100596 (2019).
17. Marofi, F. *et al.* CAR T cells in solid tumors: challenges and opportunities. *Stem Cell Res. Ther.* **12**, 81 (2021).
18. Morgan, R. A. *et al.* Case Report of a Serious Adverse Event Following the Administration of T Cells Transduced With a Chimeric Antigen Receptor Recognizing ERBB2. *Mol. Ther.* **18**, 843–851 (2010).
19. Caruso, H. G., Heimberger, A. B. & Cooper, L. J. N. Steering CAR T cells to distinguish friend from foe. *Oncoimmunology* **8**, e1271857 (2019).
20. Segev, E. *et al.* Patterned photostimulation via visible-wavelength photonic probes for deep brain optogenetics. *Neurophotonics* **4**, 011002 (2016).
21. Maresca, D. *et al.* Biomolecular Ultrasound and Sonogenetics. *Annu. Rev. Chem. Biomol. Eng.* **9**, 229–252 (2018).
22. Lele, P. P. Application of Ultrasound in Medicine. <http://dx.doi.org/10.1056/NEJM197206152862411>  
<https://www.nejm.org/doi/pdf/10.1056/NEJM197206152862411> (2010)  
doi:10.1056/NEJM197206152862411.
23. Moran, C. M. & Thomson, A. J. W. Preclinical Ultrasound Imaging—A Review of Techniques and Imaging Applications. *Front. Phys.* **8**, (2020).
24. Zander, D. *et al.* Ultrasound Image Optimization (“Knobology”): B-Mode. *Ultrasound Int. Open* **6**, E14–E24 (2020).
25. Maresca, D. *et al.* Nonlinear ultrasound imaging of nanoscale acoustic biomolecules. *Appl. Phys. Lett.* **110**, 073704 (2017).

26. Shen, C.-C., Chou, Y.-H. & Li, P.-C. Pulse Inversion Techniques in Ultrasonic Nonlinear Imaging. *J. Med. Ultrasound* **13**, 3–17 (2005).
27. Evans, D. H., Jensen, J. A. & Nielsen, M. B. Ultrasonic colour Doppler imaging. *Interface Focus* **1**, 490–502 (2011).
28. Lee, H. *et al.* Microbubbles used for contrast enhanced ultrasound and theragnosis: a review of principles to applications. *Biomed. Eng. Lett.* **7**, 59–69 (2017).
29. Punjabi, M. *et al.* Ultrasound Molecular Imaging of Atherosclerosis With Nanobodies. *Arterioscler. Thromb. Vasc. Biol.* **39**, 2520–2530 (2019).
30. Dirk-André, C., Kerstin, S., CHEN, M., ZHU, Q. & Maximilian, R. Role of contrast enhanced ultrasound in detection of abdominal aortic abnormalities in comparison with multislice computed tomography. *Chin. Med. J. (Engl.)* **122**, 858–864 (2009).
31. Jangjou, A. *et al.* The promising shadow of microbubble over medical sciences: from fighting wide scope of prevalence disease to cancer eradication. *J. Biomed. Sci.* **28**, 49 (2021).
32. Korpanty, G., Carbon, J. G., Grayburn, P. A., Fleming, J. B. & Brekken, R. A. Monitoring Response to Anticancer Therapy by Targeting Microbubbles to Tumor Vasculature. *Clin. Cancer Res.* **13**, 323–330 (2007).
33. Pfeifer, F. Distribution, formation and regulation of gas vesicles. *Nat. Rev. Microbiol.* **10**, 705–715 (2012).
34. Shapiro, M. G. *et al.* Biogenic gas nanostructures as ultrasonic molecular reporters. *Nat. Nanotechnol.* **9**, 311–316 (2014).
35. Bourdeau, R. W. *et al.* Acoustic reporter genes for noninvasive imaging of microbes in mammalian hosts. *Nature* **553**, 86–90 (2018).
36. Farhadi, A., Ho, G. H., Sawyer, D. P., Bourdeau, R. W. & Shapiro, M. G. Ultrasound imaging of gene expression in mammalian cells. *Science* (2019) doi:10.1126/science.aax4804.
37. Hurt, R. C. *et al.* Genomically Mined Acoustic Reporter Genes Enable In Vivo Monitoring of Tumors and Tumor-Homing Bacteria. 2021.04.26.441537  
<https://www.biorxiv.org/content/10.1101/2021.04.26.441537v2> (2021)  
 doi:10.1101/2021.04.26.441537.
38. Sawyer, D. P. *et al.* Ultrasensitive ultrasound imaging of gene expression with signal unmixing. *Nat. Methods* **18**, 945–952 (2021).
39. Crosby, D. *et al.* Early detection of cancer. *Science* **375**, eaay9040 (2022).
40. Wang, J. *et al.* Mammographic sensitivity as a function of tumor size: A novel estimation based on population-based screening data. *Breast Off. J. Eur. Soc. Mastology* **55**, 69–74 (2020).
41. Cell-free DNA analysis in current cancer clinical trials: a review | British Journal of Cancer. <https://www.nature.com/articles/s41416-021-01696-0>.
42. Kirkpatrick, J. *et al.* Noninvasive lung cancer detection via pulmonary protease profiling. *Sci. Transl. Med.* **12**, eaaw0262 (2020).
43. Solinas, G., Germano, G., Mantovani, A. & Allavena, P. Tumor-associated macrophages (TAM) as major players of the cancer-related inflammation. *J. Leukoc. Biol.* **86**, 1065–1073 (2009).

44. Wang, B., Barahona, M. & Buck, M. Engineering modular and tunable genetic amplifiers for scaling transcriptional signals in cascaded gene networks. *Nucleic Acids Res.* **42**, 9484–9492 (2014).
45. Aalipour, A. *et al.* Engineered immune cells as highly sensitive cancer diagnostics. *Nat. Biotechnol.* **37**, 531–539 (2019).

**THERMAL CONTROL OF ENGINEERED T-CELLS**

Abedi, M.H.; Lee, J.; Piraner, D.I.; Shapiro, M. G. Thermal Control of Engineered T-cells.

*ACS Synthetic Biology*, 2020, 9(8), 1941–1950.

This chapter is a reformatted version of the above publication. My contributions to the work were assisting in all experiments, analyzing data, and preparing the manuscript together with the other authors.

**2.1 Introduction**

Unlike small molecule and biologic therapies, cells have a natural ability to navigate, persist, and proliferate within the body, providing the potential for more targeted and sustained disease treatment. This potential is enhanced by the capacity of cells to probe, process, and respond to their environment and carry out a wide range of sophisticated behaviors, which can be engineered using the tools of synthetic biology<sup>1</sup>. Among the cell types being developed for therapy, T-cells are one of the most promising due to their central role in cancer, infectious disease, and autoimmune disorders, along with their relative ease of isolation, genetic modification, and re-engraftment. For example, this potential has been realized in T-cells engineered to express modularly targeted chimeric antigen receptors (CARs), allowing them to specifically eradicate cancers such as lymphomas bearing the CD19 antigen<sup>2,3,4,5</sup>. Unfortunately, it has been challenging to translate these successful results into solid tumors, where CAR T-cells encounter a more immunosuppressive environment<sup>6</sup> and the risk of sometimes fatal on-target off-tumor toxicity due to the presence of tumor-

overexpressed epitopes in healthy tissues<sup>7,8</sup>. Likewise, emerging approaches in which T-cells are used to treat autoimmune disease through local immunosuppression carry the risk of reducing important immune system activity outside the target tissues<sup>9</sup>. Existing strategies seeking to reduce off-target toxicity use additional target recognition elements<sup>10,11</sup> or chemically triggered kill switches<sup>12,13,14</sup>. However, it can be difficult to ensure perfect recognition solely through molecular markers, and premature termination of T-cell therapy using kill-switches turns off their beneficial therapeutic action.

Here we describe a cellular engineering approach to regulate the activity of therapeutic T-cells with greater specificity through a combination of molecular and physical actuation. This approach is designed to take advantage of the ability of technologies such as focused ultrasound (FUS) and magnetic hyperthermia to non-invasively deposit heat at precise locations in deep tissue<sup>15–18</sup>. By engineering thermal bioswitches that allow T-cells to sense small changes in temperature and use them as inputs for the actuation of genetic circuits, we enable these penetrant forms of energy to spatially control T-cell activity. Our approach is based on heat shock promoters (pHSP), which have been shown to drive gene expression in response to FUS-delivered heating<sup>19–21</sup>, but have not been tested in primary human T-cells. This is important because the behavior of pHSPs varies greatly between cell types and cellular states. In this study, we screen a library of pHSPs in primary T-cells and engineer gene circuits providing transient and sustained activation of gene expression in response to brief thermal stimuli within the well-tolerated temperature range of 37–42°C<sup>22–24</sup>. Our circuits incorporate feed-forward amplification, positive feedback, and recombinase-based state switches. We demonstrate the use of these circuits to control the secretion of a therapeutic cytokine, expression of a CAR, and killing of target tumor cells.

## 2.2 Results

### 2.2.1 Evaluating Candidate pHSPs in Primary T-cells

To enable thermal control of T-cell activity, we required a pHSP with robust switching behavior in primary human T-cells. Given the variability in pHSP responses between cell types<sup>25</sup>, we decided to systematically evaluate the activity of 13 different pHSPs in response to a 1-hour incubation at 42°C. This thermal stimulus was chosen based on its tolerability by most tissues<sup>24</sup>, and the convenience of relatively short treatment durations in potential clinical scenarios. Our panel of pHSPs included nine human, three mouse, and one *C. elegans* promoter. The human promoters included four naturally occurring sequences (HSPB, HSPB'2, HSP A/A, HSP A/B), two modifications of HSPB'2 generated by varying the 5' UTR (HSPB'1, HSPB'3), and three rational modifications of HSPB'2 (SynHSPB'1, SynHSPB'2, SynHSPB'3) inspired by a previously developed sensor of cellular stress<sup>26</sup>. Truncating HSPB'2 and leaving 192 base pairs resulted in SynHSPB'1. To lower potential baseline activity, the AP-1 binding site in SynHSPB'1 was mutated leading to SynHSPB'2. Duplicating SynHSPB'2 four times to increase the number of heat shock elements (HSE) resulted in SynHSPB'3. The three mouse-derived pHSPs were naturally occurring promoters. HSP16, derived from *C. elegans*, was first described in 1986 and is rationally modified to form a minimal bidirectional promoter encompassing four HSE binding sites<sup>27</sup>. HSP16 excludes other transcription factor binding sites that typically exist in human promoters. We incorporated each pHSP into a standardized lentiviral construct in which the pHSP drives the expression of a green fluorescent protein (GFP), with a constitutively expressed blue fluorescent protein (BFP) serving as a marker of transduction (Figure 4-1a).

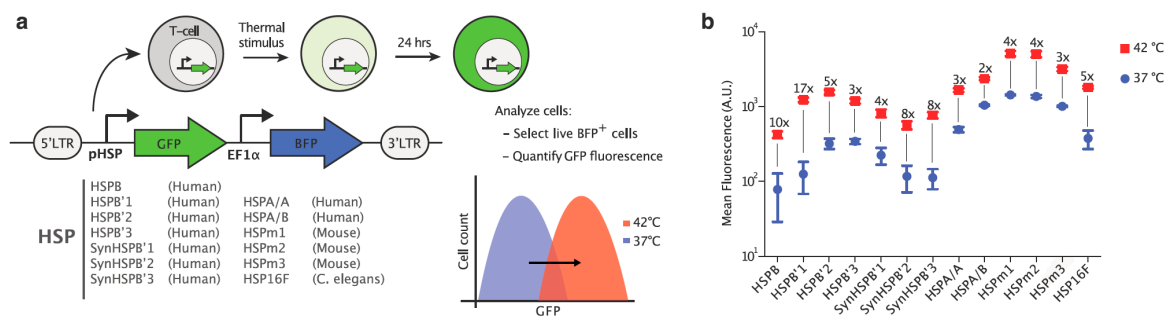


**Figure 2-1:** Evaluating candidate pHSPs in primary T-cells. **(a)** Illustration of the screening strategy used to characterize the behavior of pHSPs. The viral construct used to assay pHSPs is shown, along with the promoters tested. LTR, long terminal repeat. **(b)** Mean fluorescence intensity 24 hours after a 1-hour incubation at 37°C or 42°C, as measured via flow cytometry. The fold change between 37°C and 42°C is listed above each sample. Where not seen, error bars ( $\pm$ SEM) are smaller than the symbol. N=3 biological replicates for each sample.

Once stimulated, all of the promoters displayed a uniform level of activation across the cell population allowing us to use mean fluorescence as a metric of fold induction (Fig. 4-S1). Of our 13 promoters, HSPB had the lowest baseline expression at 37°C (Fig. 4-1b), an important property for minimizing activity in the absence of the thermal trigger. HSPB'1 showed the largest fold-change in gene expression, reflecting a combination of relatively low baseline expression and strong promoter activity when stimulated. Among the rationally engineered HSPB'2 variants, SYNHSPB'3 had a lower baseline than the natural promoter, albeit with lower maximum expression on activation. The rest of the human and mouse-derived promoters exhibited high baseline activity, resulting in their elimination from further experiments. Finally, the *C. elegans* minimal promoter exhibited acceptable performance and was included in further testing to investigate whether its minimal composition would be advantageous for specific activation in response to temperature. Based on these factors, we chose HSPB, HSPB'1, SynHSPB'3, and HSP16 as our starting points for further circuit engineering.

### 2.2.2 Thermal Parameters for pHSP Activation

After identifying four candidate pHSPs, we tested their response to a range of induction parameters. To search for temperatures that provide rapid induction with minimal thermal burden to the cells, we incubated pHSP-transduced T-cells at temperatures ranging from 37°C to 44°C for 1 hour. All four promoters exhibited a significant increase in activity starting at 42°C (Fig. 4-2a). Increasing the induction temperature beyond this point resulted in a significant enhancement of transcriptional activity, but compromised cell viability (Fig. 4-2b). To optimize induction with minimal cell damage, we chose 42°C for further experiments. We note that unlike the gradual increase in gene expression observed with the mammalian promoters above 42°C, HSP16 exhibited a large jump between this temperature and 43°C, which may make it useful in future circuit engineering applications.

To reduce the effect of thermal exposure on cell viability, we tested a pulsatile heating scheme with a 50% duty cycle<sup>28</sup>. In this scheme, cells underwent repeated cycles of heating to 42°C for a fixed duration and an equal amount of time at 37°C, adding up to a total of one hour at 42°C over a two-hour treatment period. We varied the stimulation period between one minute and continuous heating for 60 min. This experiment revealed a trade-off between promoter activity (Fig. 4-2c) and cell viability (Fig. 4-2d), with shorter pulses reducing the former while increasing the latter. For the purposes of T-cell therapy, in which cells can expand after activation, we decided that a 40% decrease in cell viability was a suitable tradeoff for improved activation, therefore selected a continuous heating paradigm. This paradigm also simplifies the application of heating during therapy. We also investigated continuous stimulation durations ranging from 15 to 120 minutes. Shorter induction enhanced viability (Fig. 4-2e) at the expense of lower gene expression (Fig. 4-2f), with a

one-hour stimulation providing a reasonable balance. While the optimal stimulation scheme would heavily depend on the promoter used, circuit design, targeted tissue, and therapeutic dose required, we chose a one-hour continuous stimulus at 42°C as our heating paradigm for our subsequent experiments to maximize our chances of getting a meaningful response despite some damage to the cells.

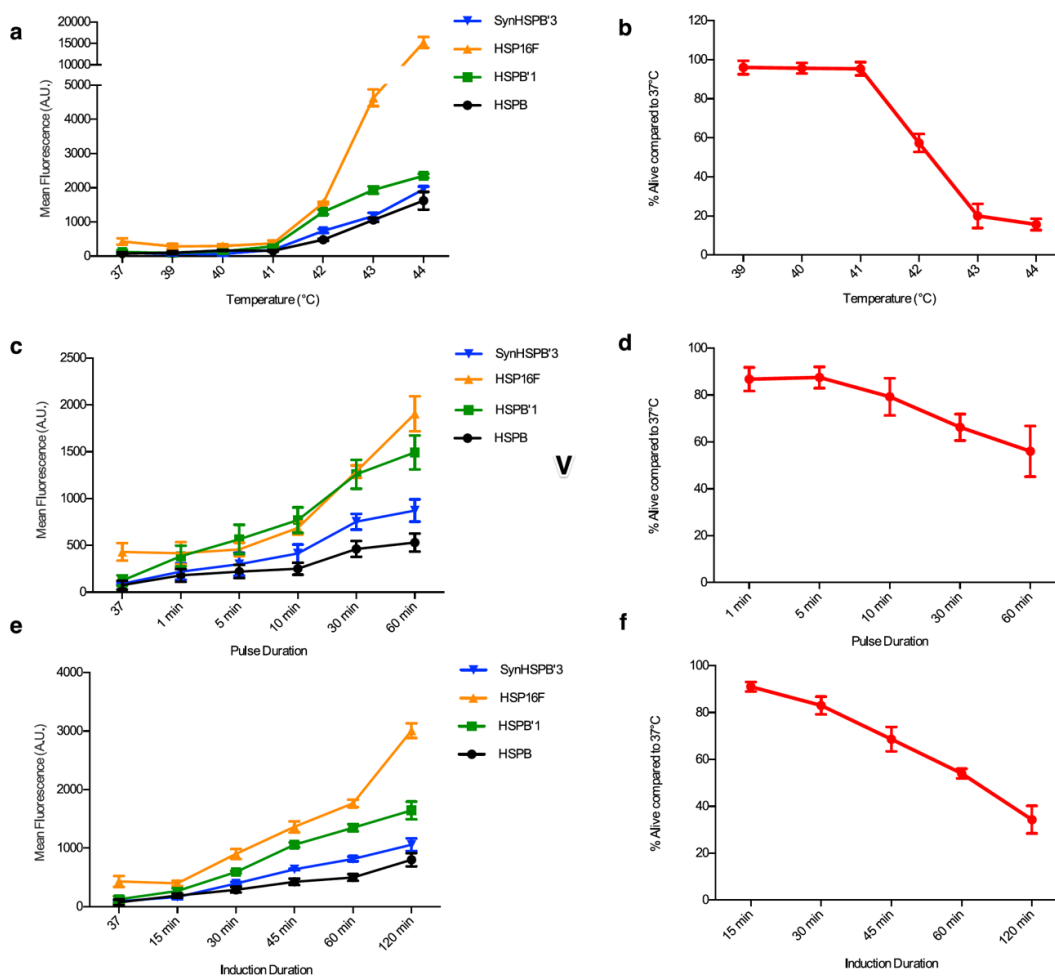


**Figure 2-2:** Thermal parameters for pHSP activation in primary human T-cells. GFP expression from constructs driven by the HSPB, HSPB'1, SynHSPB'3, and HSP16F promoters (**a, c, e**) and Tcell viability (**b, d, f**) as a function of (**a, b**) induction temperature for a continuous 1 hour stimulus, (**c, d**) pulse duration of stimuli delivered with a 50% duty cycle alternating between 37°C and 42°C for a fixed thermal exposure of 1 hour, and (**e, f**) induction duration for continuous heating at 42°C. Where not seen, error bars ( $\pm$ SEM) are smaller than the symbol. N=3 biological replicates for each sample.

### 2.2.3 Genetic Circuits for Amplified and Sustained Thermal Activation

On their own, pHSPs drove a relatively small amount of transient protein expression upon induction. To enable the use of pHSPs in T-cell therapy applications, it is useful to amplify the output of pHSP-driven circuits. This would enable cells to, for example, release a relatively large therapeutic bolus after a single thermal stimulus. To achieve this goal, we implemented a feed-forward amplification circuit in which the pHSP drives an rtTA transactivator, which produces stronger transcriptional activation tunable with doxycycline. In addition, LNGFR was constitutively expressed to identify virally transfected cells (Fig. 4-3a). Amplification circuits incorporating HSPB, HSPB'1, SynHSPB'3, and HSP16 all exhibited a substantial increase in their fold-induction, while only modestly elevating baseline expression. HSPB showed the best performance, suggesting that in the context of feed-forward amplification driving the maximum expression level, a promoter with lower leakage (Fig. 4-1b) is preferable. The expression of a constitutive transduction marker was similar across constructs (e.g., Fig. 4-S2), indicating that infection levels did not affect their relative performance. To further tune the performance of the HSPB amplifier circuit, we designed constructs with reduced translation of the GFP by varying the Kozak sequence or inserting a micro open reading frame upstream<sup>29</sup> (Fig. 4-3b). These modifications enabled the tuning of both the baseline expression and the maximal activation level.

In some therapeutic scenarios, it is critical to prolong the therapeutic action of T-cells following a thermal induction treatment. This would eliminate the need to apply repeated stimuli to maintain treatment efficacy. To develop this capability, we established a positive feedback amplifier circuit by rearranging the elements of our feed-forward amplifier such that rtTA could drive its own expression in the presence of doxycycline (Fig. 4-3c). A similar

design was previously tested in human cervical cancer HeLa cells<sup>30</sup>. The HSPB feedback circuit maintained its thermal induction level, and we were able to reduce baseline activity by tuning the Kozak sequence upstream of rtTA. In the current design, the output of the positive feedback circuit is lower than that of the feed-forward amplifier, as expected from the GFP payload being placed after an IRES element. While we envision that such “low but steady” activity is desirable in many applications, a “high and steady” mode could in principle be achieved by exchanging the IRES for a 2A element. The dynamic expression profiles of our direct, feed-forward, and feedback HSPB circuits are compared in Fig. 4-3d, demonstrating prolonged expression with positive feedback.

While the positive feedback circuit sustained expression for several days, this circuit can eventually turn off amid dilution or fluctuating expression of the transactivator. To establish a permanent thermal switch, we tested gene circuits in which we placed the expression of CRE recombinase under the control of candidate pHSPs (Fig. 4-3e). In these circuits, the pHSP-driven expression of CRE permanently toggles the circuit from expressing RFP to expressing anti-CD19 CAR by recombining the target vector. When tested in a Jurkat T-cell line, these circuits demonstrated robust activation and minimal leakage (Fig. 4-3f). However, when tested in primary T-cells, we observed significantly higher levels of background activation (Fig. 4-3f). This may arise from the fact that immune stimulation is used to maintain primary T-cells in culture and our finding, discussed below, that pHSPs show significant background activity in stimulated primary T-cells. Taken together, these results suggest that in primary T-cells, feed-forward and feed-back amplification provide robust methods for thermal control of gene expression, while pHSP-controlled CRE

recombination may produce an unacceptable level of irreversibly accumulating background activation.

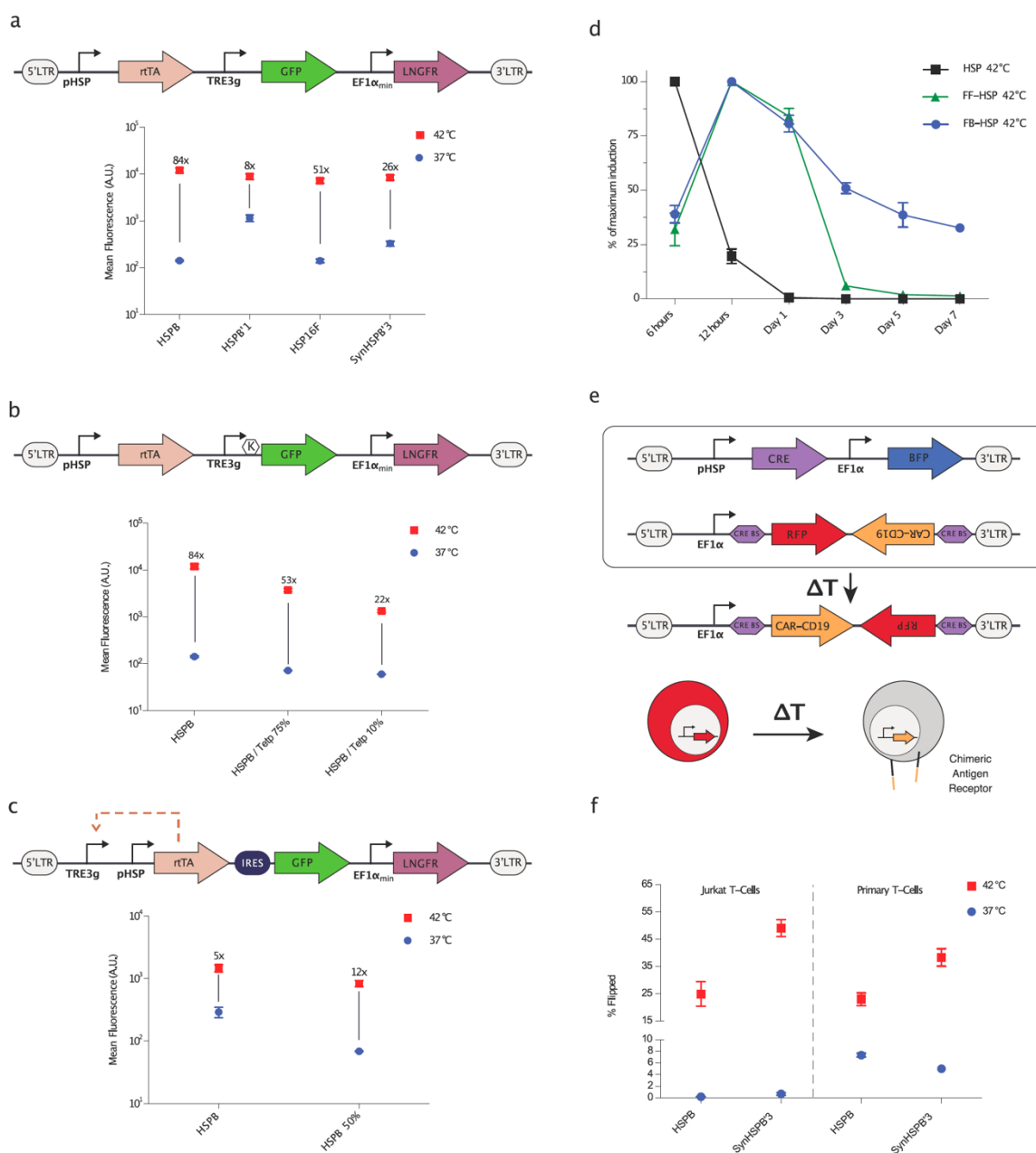


**Figure 2-3:** Genetic circuits for amplified and sustained thermal activation. **(a)** Diagram illustrating the thermally triggered feed-forward circuit (top). Fluorescence analyzed 24 hours post a 1-hour induction at 37° or 42°C for cells supplemented with doxycycline (bottom). **(b)** Diagram illustrating a feed-forward circuit driven by HSPB,  $\langle K \rangle$  indicates varying kozak strength (top). Fluorescence analyzed 24 hours post a 1-hour induction at 37° or 42°C for cells supplemented with doxycycline (bottom). The HSPB data is the same as in panel **(a)**, and is re-shown here to facilitate comparisons.

(c) Diagram illustrating the thermally triggered positive feedback circuit (top). Fluorescence analyzed 24 hours post a 1-hour induction at 37° or 42°C for cells supplemented with doxycycline (bottom). (d) Normalized expression monitored over seven days after a 1-hour induction at 42°C for direct HSPB-driven, feed-forward HSPB, and positive-feedback HSPB circuits. Circuits have been modified to replace GFP with a destabilized version of the protein. (e) Illustration of the CRE-based thermally triggered permanently stable switch designed to express CAR-CD19 upon induction. (f) Cells were either incubated at 37°C or thermally stimulated for 1 hour at 42°C and analyzed 24 hours later to determine the number of activated cells. Where not seen, error bars ( $\pm$ SEM) are smaller than the symbol. N=3 biological replicates for each sample.

## 2.2d: Temperature-activated Cytokine Release

To demonstrate the ability of our positive feedback circuit to sustain a therapeutically relevant function after thermal induction, we connected its output to the production of a cytokine. The local delivery of cytokines from engineered T-cells would be useful in cancer immunotherapy by allowing T-cells to secrete immune-stimulatory factors to remodel the tumor microenvironment and reduce immunosuppression. It would also be useful in treatments of autoimmune disease by allowing T-cells to secrete factors locally downregulating the activity of endogenous immune cells. As a model cytokine, we selected IL-21, which has potential utility in cancer immunotherapy due to its ability to stimulate NK cells and CD8<sup>+</sup> T-cells<sup>31,32</sup>. We incorporated human IL-21 in place of GFP in our positive feedback circuit (Fig. 4-4a). Without thermal induction, primary T-cells transduced with this circuit produced minimal IL-21. Once stimulated, the cells rapidly secreted IL-21, reaching a near-maximal level by 12 hours, and sustained activity for at least 5 days (Fig. 4-4a). The dependence of continued circuit function on doxycycline provides an additional layer of control, allowing the termination of therapy production at a desired time by removing doxycycline. To demonstrate this capability, we removed doxycycline 24 hours after cell induction, resulting in the abrogation of cytokine production by day five. The ability to

chemically terminate the activity of our circuit enhances its safety profile in potential therapeutic applications.

In some scenarios, it would be useful for cytokine release to be triggered from a T-cell constitutively expressing a CAR, allowing the cytokine to locally boost immune activation during CAR-directed killing. To test this possibility, we co-transduced primary T-cells with our positive IL-21 circuit and a constitutively expressed anti-CD19 CAR (Fig. 4-4b). In the absence of target Raji bait cells expressing CD19, IL-21 release was well-controlled by thermal induction (Fig. 4-4b). However, co-incubation with bait cells resulted in the activation of IL-21 release after 3 days in co-culture even in the absence of a thermal treatment (Fig. 4-4b). These results suggested that HSP activity may be driven by T-cell stimulation, as evidenced by IL-21 release. However, since certain subsets of T-cells have been shown to release endogenous IL-21 when stimulated<sup>33</sup>, we set out to directly test the induction of pHSP upon T-cell stimulation using a non-cytokine output, as discussed below.

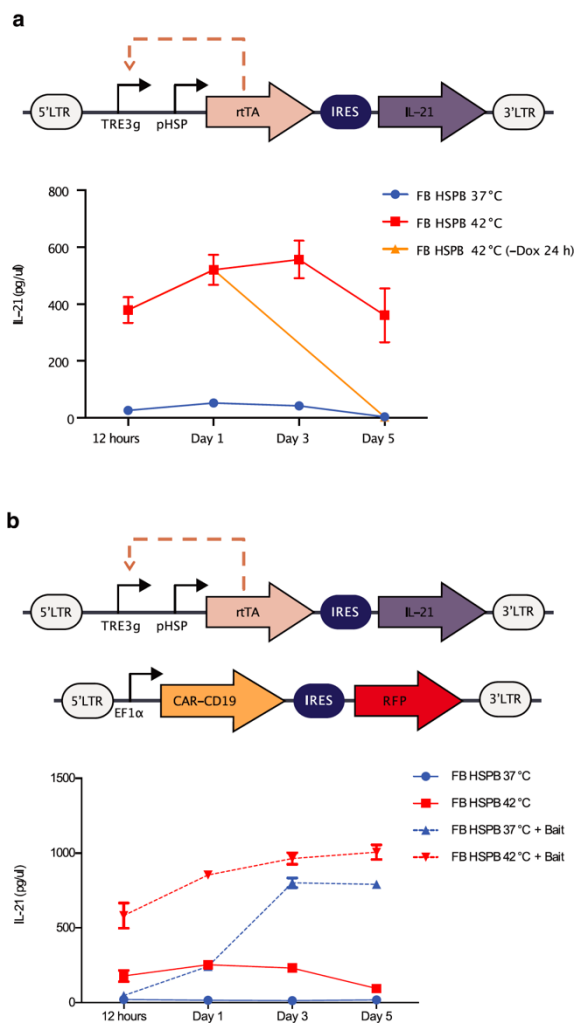


**Figure 2-4:** Temperature-activated cytokine release. **(a)** Diagram illustrating the positive feedback circuit used to express IL-21 (top). Cumulative IL-21 release from 1-hour induction at 37° or 42°C. In one sample, doxycycline was removed after 24 hours (bottom). **(b)** Illustration of the constructs used to assay the ability of CAR activity to trigger expression of IL-21 in the feedback pHSP circuit (top). Cells were either incubated at 37°C or thermally stimulated for 1 hour at 42°C with and without bait cells (bottom). Media was collected and frozen at each time point and all samples were analyzed simultaneously at the end of collection. Cumulative IL-21 expression was quantified by using an IL-21 ELISA. Where not seen, error bars ( $\pm$ SEM) are smaller than the symbol. N=3 biological replicates for each sample.

### **2.2e: Dependence of pHSP-driven Circuits on T-cell Activation**

To directly examine the possibility that pHSPs are turned on in response to CAR-driven T-cell activation, we tested the expression of pHSP-driven GFP in constitutively CAR expressing T-cells (Fig. 4-5a) upon exposure to a thermal stimulus or bait cells. We found that both thermal stimulation and CAR engagement led to pHSP-driven gene expression (Fig. 4-5b). This response occurred in cells expressing circuits based on HSPB, SynHSPB'3, and HSPmin promoters. Because SynHSPB'3 lacks the AP-1 site present in wild-type pHSPs such as HSPB, and HSPmin is composed of only HSE binding sites driving a minimal promoter, these results suggest that pHSP induction takes place via an HSF1-mediated mechanism. This unexpected finding suggests that activated T-cells experience cellular stress--for example due to rapid proliferation--potentially resulting in an increased number of mis-folded proteins, leading to HSP upregulation. This provides an important insight for the design of thermally inducible immunotherapies.

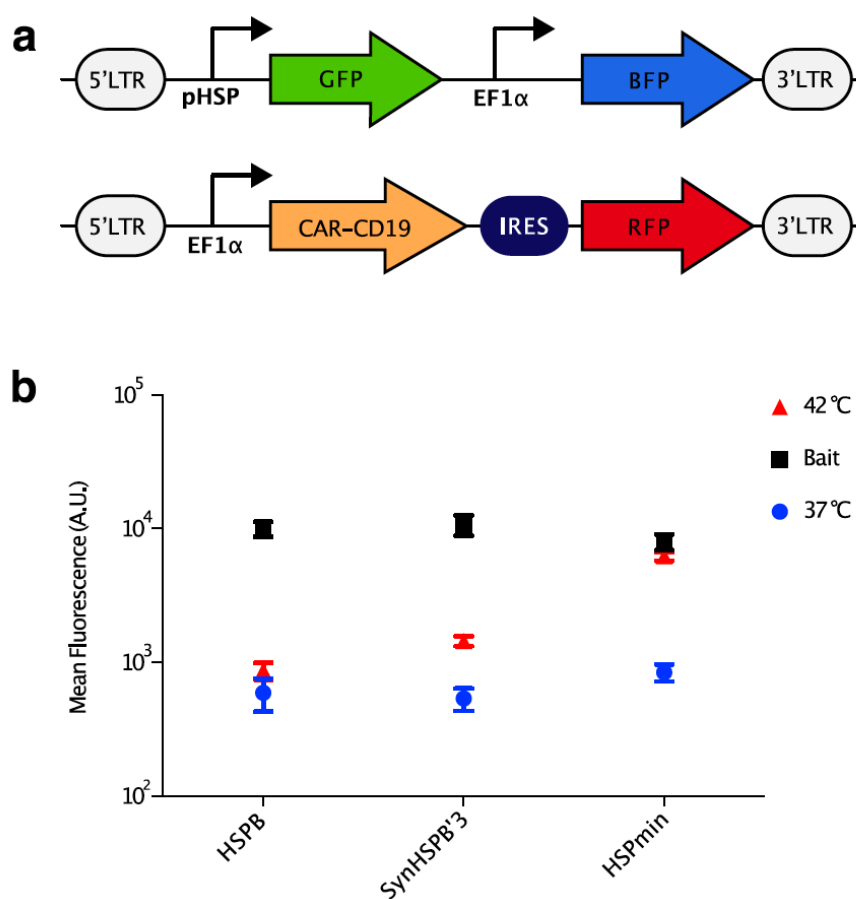


**Figure 2-5:** Dependence of pHSP-driven circuits on T-cell activation. **(a)** Illustration of the constructs used to assay the ability of CAR activity to trigger pHSP. **(b)** Cells were either incubated at 37°C, thermally stimulated for 1 hour at 42°C, or incubated with CD19<sup>+</sup> bait cells. pHSP triggered activity was determined by quantifying GFP expression 24 hours after induction. Where not seen, error bars ( $\pm$ SEM) are smaller than the symbol. N=3 biological replicates for each sample.

### 2.2f: Auto-Sustained Thermally Induced Tumor Killing

Our finding that CAR engagement drives pHSP activity suggested that a simple, auto-sustained gene circuit could drive CAR-mediated killing in response to the combination of a thermal stimulus and the presence of target cells. In particular, we hypothesized that placing CAR expression under the control of a pHSP (Fig. 4-6a) would result in T-cells with no

initial CAR expression or activity, even in the presence of target cells. Upon thermal induction, CAR would become transiently expressed. If the CAR target is present in the vicinity of T-cells, these cells would become activated, driving sustained expression of additional CAR from the pHSP and target cell killing.

As predicted, this pHSP-CAR circuit showed no baseline CAR expression in primary T-cells but began to express CAR when thermally stimulated (Fig. 4-6a). CAR expression was greatly reduced after 24 hours in the absence of target engagement (Fig. 4-6b). When cultured with CD19<sup>+</sup> bait cells (Fig. 4-6c), thermally activated pHSP-CAR T-cells eliminated the bait cells after 9 days in co-culture (Fig. 4-6d, Fig. 4-S3). This killing was as complete as with positive control T-cells carrying a constitutively expressed CAR driven by the EF1 $\alpha$  promoter, albeit over a longer time span. This difference may be due to the maximum level of pHSP-driven CAR expression being lower than the level observed with a constitutive EF1 $\alpha$  promoter (Fig. 4-S4). When pHSP-CAR T-cells and bait cells were co-incubated without thermal stimulation, no apparent killing took place. While the initial thermal stimulus results in some cell death, T-cells maintain their proliferative capacity and rapidly make up for the initial loss in T-cells (Fig. 4-S5). These results suggest that a thermal stimulus can kick-start a positive feedback loop of activation-driven expression of CAR from pHSP, leading to effective bait cell elimination. This activation paradigm could help with mitigating off-target toxicity since CAR expression will be abrogated once T-cells leave the tumor site.

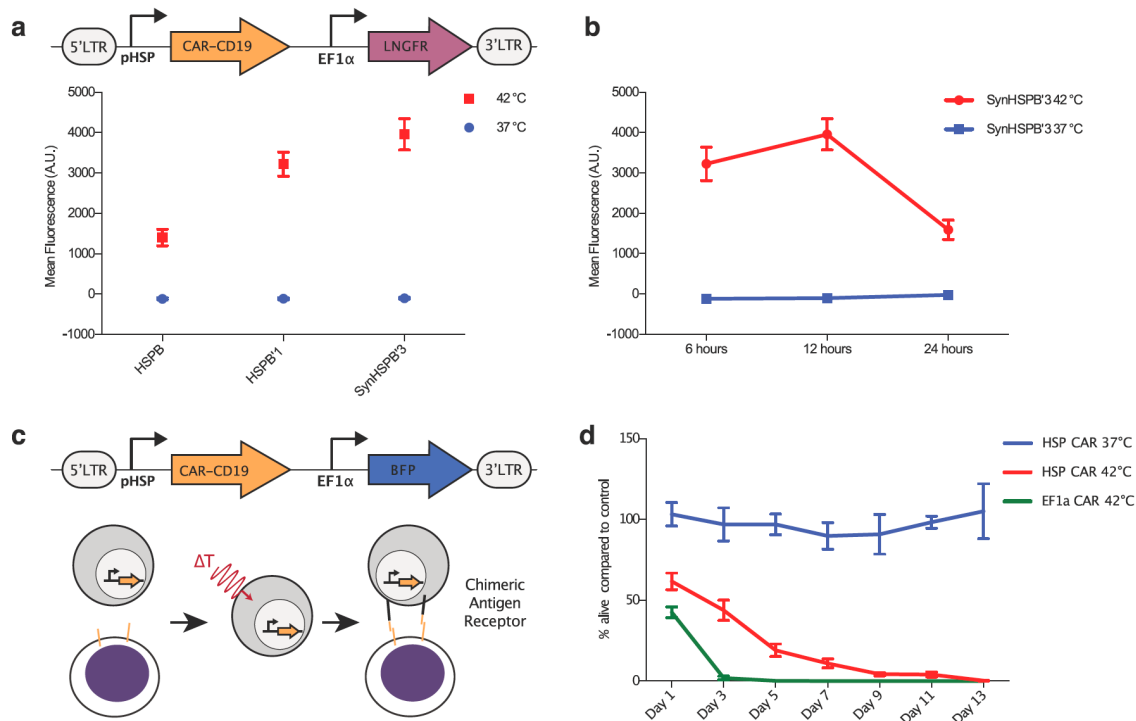


**Figure 2-6:** Auto-sustained thermally induced CAR expression and tumor cell killing. **(a)** Illustration of the viral construct used to assay pHSP (SynHSPB'3)-driven expression of CAR-CD19. Cells were either incubated at 37°C or thermally stimulated for 1 hour at 42°C, and pHSP-triggered CAR-CD19 expression was quantified by surface staining of an HA tag appended to the CAR 12 hours after induction. N=3 biological replicates. **(b)** CAR-CD19 expression 6, 12, and 24 hours after 1-hour induction with 37°C or 42°C. N=3 biological replicates. Negative values in 37°C samples result from subtraction of signal acquired from wild-type T-cells. Raw data is provided in (Fig. S6). **(c)** Illustration of the viral construct and assay used to test the ability of pHSP-inducible CAR expression to conditionally kill bait cells. Cells were either incubated at 37°C or thermally stimulated for 1 hour at 42°C before being incubated with CD19+ bait cells. **(d)** Unmodified T-cells and T-cells constitutively expressing CAR-CD19 were used as a negative and positive control respectively. pHSP (SynHSPB'3)-triggered killing activity was quantified by counting the % of bait cells alive compared to the negative control for a duration of 13 days. N= 3 biological replicates for two T-cell collections from different patients, total N=6. Where not seen, error bars ( $\pm$ SEM) are smaller than the symbol.

## 2.3 Discussion

Our results demonstrate that engineered bioswitch circuits using pHSP can provide control of T-cell therapy with mild hyperthermia. While it has been previously shown that light-switchable proteins could also confer spatiotemporal control over T-cell activity<sup>34</sup>, light has poor penetration into tissues, limiting the utility of such tools. On the other hand, temperature can be elevated at arbitrary depth and with high spatial precision using non-invasive methods such as FUS or magnetic hyperthermia<sup>15-18</sup>.

Our study showed that temperatures in the well-tolerated range of 37-42°C<sup>35,36</sup> can provide control over T-cell function, including the synthesis and release of a cytokine and the CAR-mediated killing of cancer cells in vitro, with minimal baseline activity. In future studies, this performance must be characterized and optimized in the in vivo setting. In particular, it will be useful to optimize the thermal requirements of ultrasound activation. While thermal tissue damage is not a major concern in tumor therapy (where it can be synergistic), damage to healthy tissues in non-tumor applications could be detrimental<sup>35,36</sup>. It would also be desirable to shorten the FUS treatment duration to substantially less than the 1 hour heat pulse used in this study. Further promoter engineering, protein engineering, and thermal pulse optimization could broaden the range of applications for this technology.

Despite their name, pHSPs can respond to a variety of stimuli such as heat, hypoxia, heavy metals, cytokines, and cell division<sup>37,38</sup>. Therefore, the context in which these promoters are being used must be carefully considered. In this work, we capitalized on non-thermal pHSP induction by the T-cell receptor pathway to generate sustained killing circuits. In other contexts where the promiscuous responsiveness of pHSPs presents an un-exploitable

hindrance, it may be desirable to develop thermal response mechanisms based on orthogonal molecular bioswitches<sup>22,23</sup>.

## **2.4 Methods**

### **Plasmid Construction and Molecular Biology**

All plasmids were designed using SnapGene (GSL Biotech) and assembled via reagents from New England Biolabs for KLD mutagenesis (E0554S) or Gibson Assembly (E2621L). After assembly, constructs were transformed into NEB Turbo (C2984I) and NEB Stable (C3040I) *E. coli* for growth and plasmid preparation. The CAR-CD19 gene containing the CD28 and CD3z signaling domain was a kind gift from the Laboratory of David Baltimore (Caltech). Integrated DNA Technologies synthesized other genes, the pHSP, and all PCR primers. Kozak used in Figure 3B: CGG-ATG for 75% and ACCATGGGTTGAGCC-ATG for 10%. The original Kozak was ACC-ATG.

### **Cell Lines**

Raji cells (CCL-86) were obtained from ATCC and cultured in RPMI 1640 media (Thermo Fisher Scientific) with 1x Penicillin/Streptomycin (Corning). 1000 ng/ml of doxycycline was used for induction of the Tet promoter. GFP<sup>+</sup> Raji cells were constructed via viral infection of a GFP driven by the EF1a promoter. Lentivirus was prepared using a third-generation viral vector and helper plasmids (gifts of D. Baltimore). Virus was packaged in HEK293T cells grown in 10 cm dishes. After 3 days of transfection, viral particles were concentrated via ultracentrifugation. Infection was performed by following the “RetroNectin” (T100B Takara Bio) reagent protocol. Experiments were performed at least two weeks after infection. Primary T-cells T-cells were isolated with the EasySep Human T-cell isolation Kit (STEMCELL Technologies 17951) from frozen human peripheral blood mononuclear cells obtained from healthy donors. T-cells were stimulated with CD3/CD28 Dynabeads (Thermo Fisher Scientific 11132D) at 1:1 cell:bead ratio for 1 day before viral transduction. Dynabeads were removed on day seven and the cells were allowed to rest until day fourteen before proceeding with experiments. This delay was designed to avoid any activation

interference with HSP activity. T-cells were cultured in RPMI supplemented with 50 U/ml IL-2 (Miltenyi Biotech 130-097-744) and 1 ng/ml IL-15 (Miltenyi Biotech 130-095-762) every other day. T-cells were enriched by LNGFR magnetic bead based sorting (Miltenyi Biotech 130-091-330) when appropriate.

### **Thermal Regulation Assay**

Thermal stimulation of T-cells was performed in a Bio-Rad C1000 thermocycler. T-cells at 1-2 million/ml were supplemented with doxycycline, if needed, and mixed well before transferring 50  $\mu$ l into a sterile PCR tube. The temperature and duration of stimulation was varied based on the experimental procedure. Upon completion of thermal stimulation, cells were moved back into a mammalian incubator and supplemented 1:1 with fresh media containing cytokines and in some cases doxycycline. Cells were typically incubated for 24 hours unless stated otherwise before assaying with a flow cytometer (MACSQuant VYB). Dead cells were typically excluded via FSC/SSC gating for routine assays. In Figure 2, a LIVE/DEAD viability/cytotoxicity kit (Thermo Fisher L3224) was used for a more accurate quantification of cell state. Live cells were further gated via a transfection marker to isolate virally infected cells for further analysis. The change in mean fluorescence of the cell population was used to characterize the fold change of pHSP constructs. To account for cellular auto-fluorescence, the mean fluorescence signal from non-transduced T-cells was collected in each experiment and subtracted from the mean fluorescence of experimental T-cells. Anti-HA antibodies (Miltenyi Biotech 130-120-722) were used to stain for CAR expression, and V450 Mouse Anti-human CD271 was used to stain LNGFR (BD biosciences 562123). IL-21 expression was measured using a human IL-21 DuoSet ELISA (R&D systems DY8879-05).

### **T-cell Bait Assay**

Raji and GFP<sup>+</sup> Raji cells were used as bait cells for CAR-CD19 T-cells. Bait assays were initiated by mixing T-cells with bait cells at a 3:1 ratio. This ratio was established to avoid excessive bait cell growth before T-cell engagement. To assess T-cell killing of bait cells, GFP<sup>+</sup> Raji were used and the count of GFP<sup>+</sup> cells was tracked over time.

**Data and Code Availability**

Plasmids will be made available through Addgene upon publication. All other materials and data are available from the corresponding author upon reasonable request.

## 2.5 Supplementary Figures

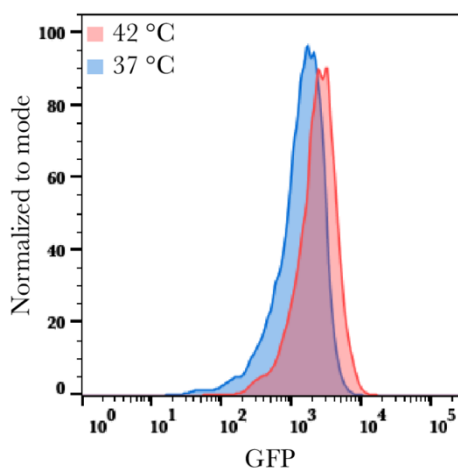


**Figure 2-S1:** Thermally induced shift in gene expression. T-cells were transfected with the HSPB'1 promoter viral vector from Figure 1. The histogram represents the green fluorescence intensity of infected cells 24 hours after a 1-hour incubation at 37°C or 42°C, as measured via flow cytometry. Thermal induction led to a uniform increase in gene expression across the cell population.

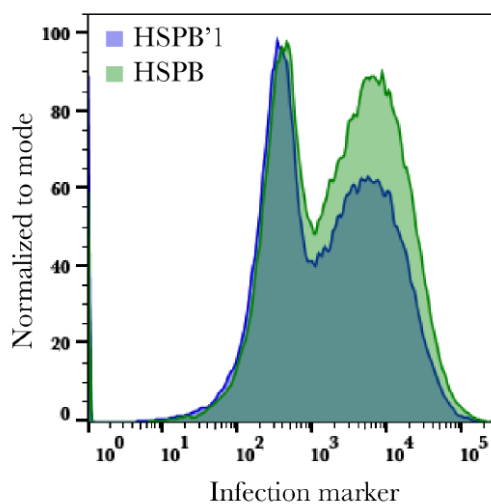


**Figure 2-S2:** Expression of a transduction marker to control for variability in infection. Constructs in our experiments carried an infection marker that was used to assess any differences in viral integration efficiency. In this example, T-cells were infected with the HSPB and HSPB'1 feedforward circuits from Figure 3A. Both constructs had similar expression levels of the infection marker and comparable transduction efficiency HSPB (63%) and HSPB'1 (54%).

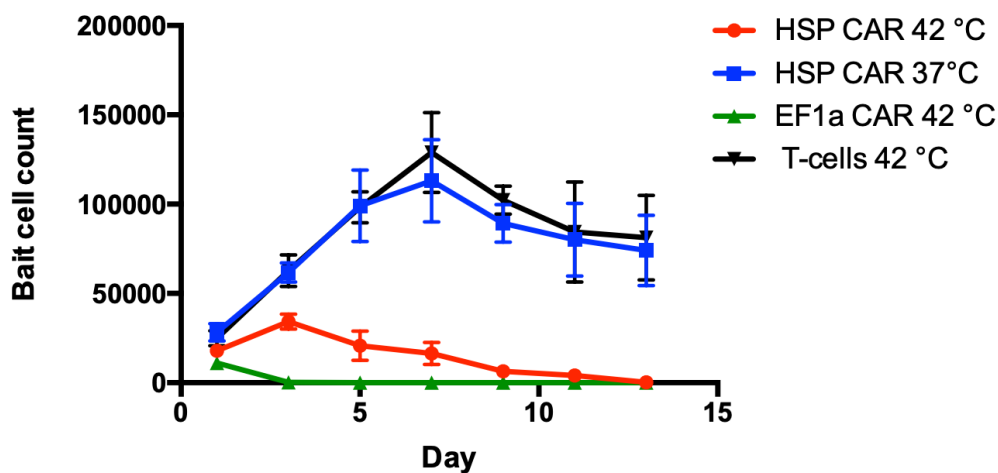


**Figure 2-S3:** Bait cell count for the HSP CAR killing experiment. Primary T-cells were either incubated at 37°C or thermally stimulated for 1 hour at 42°C before being incubated with CD19+ bait cells. Unmodified T-cells and T-cells constitutively expressing CAR-CD19 were used as a negative and positive control, respectively. HSP (SynHSPB'3) triggered killing activity was quantified by counting the number of bait cells alive over 13 days. N= 3 biological replicates. Where not seen, error bars ( $\pm$ SEM) are smaller than the symbol.

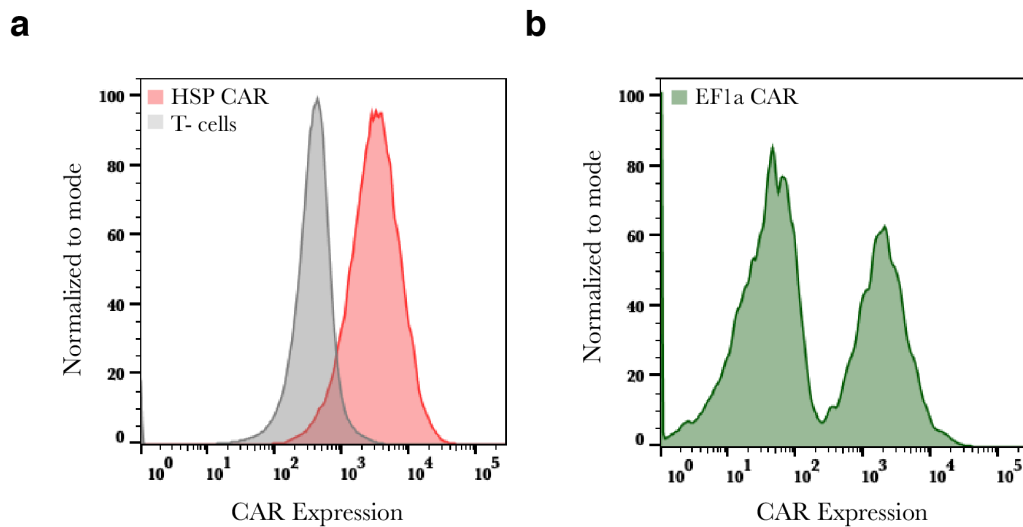


**Figure 2-S4:** CAR expression from constitutive and induced constructs. **(a)** Primary T-cells infected with SynHSPB'3 were thermally stimulated for 1 hour at 42 °C. CAR expression was assessed 12 hours post stimulation by using an Anti-HA antibody. Cells were gated based on a transfection marker before CAR expression analysis. **(b)** Primary T-cells constitutively expressing CAR-CD19 were used as a positive control. Cells in panel **(b)** were not gated with a transfection marker. The left peak represents uninfected cells.

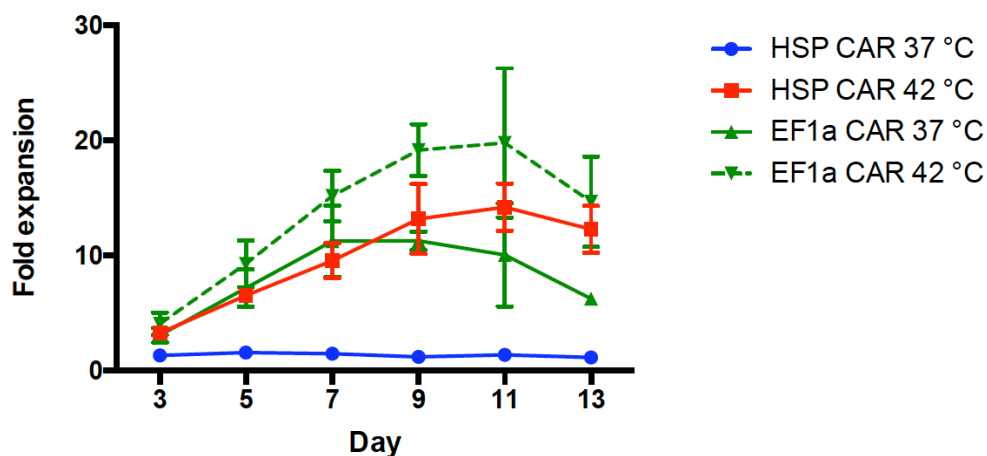


**Figure 2-S5:** Assessing the proliferative capacity of stimulated T-cells. T-cells constitutively expressing CAR-CD19 were used as a control, and SynHSPB'3 was used for HSP T-cells. Cells were either incubated at 37°C or thermally stimulated for 1 hour at 42°C before being incubated with CD19<sup>+</sup> bait cells. T-cell proliferation was quantified by counting the number of T-cells alive and comparing it to day 1 to establish fold change. N= 3 biological replicates. Where not seen, error bars ( $\pm$ SEM) are smaller than the symbol.

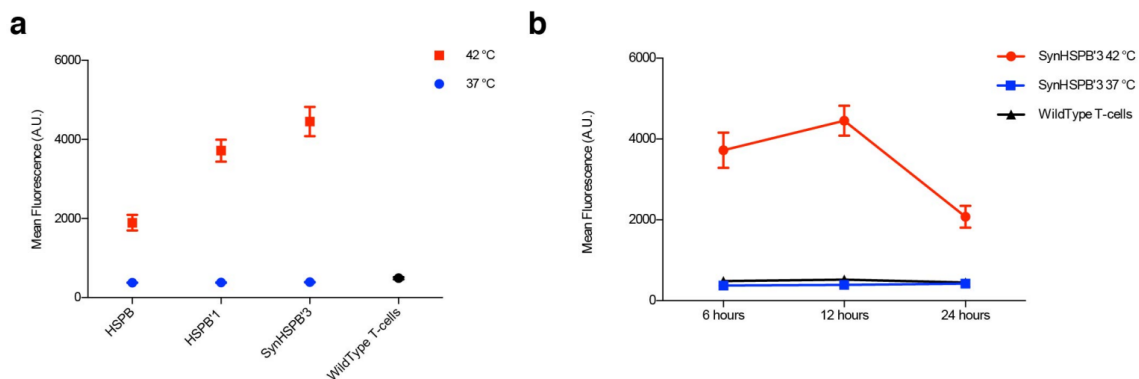


**Figure 2-S6:** Thermally induced CAR expression. Raw measurements underlying the data shown in Figure 6 (a, b), including the fluorescence of wild-type T-cells. This background value was subtracted from the experimental cell measurements to generate the plots in Figure 6 (a, b). (a) Cells were either incubated at 37°C or thermally stimulated for 1 hour at 42°C and pHSP-triggered CAR CD19 expression was quantified by surface staining of an HA tag appended to the CAR 12 hours after induction. N=3 biological replicates. (b) CAR-CD19 expression 6, 12, and 24 hours after 1-hour induction with 37°C or 42°C. Where not seen, error bars ( $\pm$ SEM) are smaller than the symbol.

## 2.6: References

- (1) P Teixeira, A., and Fussenegger, M. (2019) Engineering mammalian cells for disease diagnosis and treatment. *Curr. Opin. Biotechnol.* 55, 87–94.
- (2) Brentjens, R. J., Davila, M. L., Riviere, I., Park, J., Wang, X., Cowell, L. G., Bartido, S., Stefanski, J., Taylor, C., Olszewska, M., Borquez-Ojeda, O., Qu, J., Wasielewska, T., He, Q., Bernal, Y., Rijo, I. V., Hedvat, C., Kobos, R., Curran, K., Steinherz, P., Jurcic, J., Rosenblat, T., Maslak, P., Frattini, M., and Sadelain, M. (2013) CD19-Targeted T Cells Rapidly Induce Molecular Remissions in Adults with Chemotherapy-Refractory Acute Lymphoblastic Leukemia. *Sci. Transl. Med.* 5, 177ra38-177ra38.
- (3) Turtle, C. J., Hanafi, L.-A., Berger, C., Gooley, T. A., Cherian, S., Hudecek, M., Sommermeyer, D., Melville, K., Pender, B., Budiarto, T. M., Robinson, E., Steevens, N. N., Chaney, C., Soma, L., Chen, X., Yeung, C., Wood, B., Li, D., Cao, J., Heimfeld, S., Jensen, M. C., Riddell, S. R., and Maloney, D. G. (2016) CD19 CAR-T cells of defined CD4+:CD8+ composition in adult B cell ALL patients. *J. Clin. Invest.* 126, 2123–2138.
- (4) Brentjens, R. J., Riviere, I., Park, J. H., Davila, M. L., Wang, X., Stefanski, J., Taylor, C., Yeh, R., Bartido, S., Borquez-Ojeda, O., Olszewska, M., Bernal, Y., Pegram, H., Przybylowski, M., Hollyman, D., Usachenko, Y., Pirraglia, D., Hosey, J., Santos, E., Halton, E., Maslak, P., Scheinberg, D., Jurcic, J., Heaney, M., Heller, G., Frattini, M., and Sadelain, M. (2011) Safety and persistence of adoptively transferred autologous CD19-targeted T cells in patients with relapsed or chemotherapy refractory B-cell leukemias. *Blood* 118, 4817–4828.
- (5) Kochenderfer, J. N., Wilson, W. H., Janik, J. E., Dudley, M. E., Stetler-Stevenson, M., Feldman, S. A., Maric, I., Raffeld, M., Nathan, D.-A. N., Lanier, B. J., Morgan, R. A., and Rosenberg, S. A. (2010) Eradication of B-lineage cells and regression of lymphoma in a patient treated with autologous T cells genetically engineered to recognize CD19. *Blood* 116, 4099–4102.
- (6) Zhang, Y., and Ertl, H. C. J. (2016) Starved and Asphyxiated: How Can CD8(+) T Cells within a Tumor Microenvironment Prevent Tumor Progression. *Front. Immunol.* 7, 32.
- (7) Morgan, R. A., Chinnasamy, N., Abate-Daga, D., Gros, A., Robbins, P. F., Zheng, Z., Dudley, M. E., Feldman, S. A., Yang, J. C., Sherry, R. M., Phan, G. Q., Hughes, M. S., Kammula, U. S., Miller, A. D., Hessman, C. J., Stewart, A. A., Restifo, N. P., Quezado, M. M., Alimchandani, M., Rosenberg, A. Z., Nath, A., Wang, T., Bielekova, B., Wuest, S. C., Akula, N., McMahon, F. J., Wilde, S., Mosetter, B., Schendel, D. J., Laurencot, C. M., and Rosenberg, S. A. (2013) Cancer regression and neurological toxicity following anti-MAGE-A3 TCR gene therapy. *J. Immunother.* 36, 133–151.
- (8) Morgan, R. A., Yang, J. C., Kitano, M., Dudley, M. E., Laurencot, C. M., and Rosenberg, S. A. (2010) Case Report of a Serious Adverse Event Following the Administration of T Cells Transduced With a Chimeric Antigen Receptor Recognizing ERBB2. *Mol. Ther.* 18, 843–851.
- (9) Ellebrecht, C. T., Bhoj, V. G., Nace, A., Choi, E. J., Mao, X., Cho, M. J., Zenzo, G. D., Lanzavecchia, A., Seykora, J. T., Cotsarelis, G., Milone, M. C., and Payne, A. S. (2016) Reengineering chimeric antigen receptor T cells for targeted therapy of autoimmune disease. *Science* 353, 179–184.

- (10) Zah, E., Lin, M.-Y., Silva-Benedict, A., Jensen, M. C., and Chen, Y. Y. (2016) T Cells Expressing CD19/CD20 Bispecific Chimeric Antigen Receptors Prevent Antigen Escape by Malignant B Cells. *Cancer Immunol. Res.* 4, 498–508.
- (11) Roybal, K. T., Rupp, L. J., Morsut, L., Walker, W. J., McNally, K. A., Park, J. S., and Lim, W. A. (2016) Precision Tumor Recognition by T Cells With Combinatorial Antigen-Sensing Circuits. *Cell* 164, 770–779.
- (12) Traversari, C., Marktel, S., Magnani, Z., Mangia, P., Russo, V., Ciceri, F., Bonini, C., and Bordignon, C. (2007) The potential immunogenicity of the TK suicide gene does not prevent full clinical benefit associated with the use of TK-transduced donor lymphocytes in HSCT for hematologic malignancies. *Blood* 109, 4708–4715.
- (13) Di Stasi, A., Tey, S.-K., Dotti, G., Fujita, Y., Kennedy-Nasser, A., Martinez, C., Straathof, K., Liu, E., Durett, A. G., Grilley, B., Liu, H., Cruz, C. R., Savoldo, B., Gee, A. P., Schindler, J., Krance, R. A., Heslop, H. E., Spencer, D. M., Rooney, C. M., and Brenner, M. K. (2011) Inducible apoptosis as a safety switch for adoptive cell therapy. *N. Engl. J. Med.* 365, 1673–1683.
- (14) Tey, S.-K., Dotti, G., Rooney, C. M., Heslop, H. E., and Brenner, M. K. (2007) Inducible caspase 9 suicide gene to improve the safety of allodepleted T cells after haploidentical stem cell transplantation. *Biol. Blood Marrow Transplant.* 13, 913–924.
- (15) Thiesen, B., and Jordan, A. (2008) Clinical applications of magnetic nanoparticles for hyperthermia. *Int. J. Hyperthermia* 24, 467–474. (16) Huang, X., El-Sayed, I. H., Qian, W., and El-Sayed, M. A. (2006) Cancer Cell Imaging and Photothermal Therapy in the Near-Infrared Region by Using Gold Nanorods. *J. Am. Chem. Soc.* 128, 2115–2120.
- (17) Piraner, D. I., Farhadi, A., Davis, H. C., Wu, D., Maresca, D., Szablowski, J. O., and Shapiro, M. G. (2017) Going Deeper: Biomolecular Tools for Acoustic and Magnetic Imaging and Control of Cellular Function. *Biochemistry* 56, 5202–5209.
- (18) Haar, G., and Coussios, C. (2007) High intensity focused ultrasound: Physical principles and devices. *Int. J. Hyperthermia* 23, 89–104.
- (19) Guilhon, E., Voisin, P., Zwart, J. A. de, Quesson, B., Salomir, R., Maurange, C., Bouchaud, V., Smirnov, P., Verneuil, H. de, Vekris, A., Canioni, P., and Moonen, C. T. W. (2003) Spatial and temporal control of transgene expression in vivo using a heat-sensitive promoter and MRI guided focused ultrasound. *J. Gene Med.* 5, 333–342.
- (20) Deckers, R., Quesson, B., Arsaut, J., Eimer, S., Couillaud, F., and Moonen, C. T. W. (2009) Image-guided, noninvasive, spatiotemporal control of gene expression. *Proc. Natl. Acad. Sci. U. S. A.* 106, 1175–1180.
- (21) Kruse, D. E., Mackanos, M. A., Connell-Rodwell, C. E., Contag, C. H., and Ferrara, K. W. (2008) Short-duration-focused ultrasound stimulation of Hsp70 expression in vivo. *Phys. Med. Biol.* 53, 3641–3660.
- (22) Piraner, D. I., Abedi, M. H., Moser, B. A., Lee-Gosselin, A., and Shapiro, M. G. (2017) Tunable thermal bioswitches for in vivo control of microbial therapeutics. *Nat. Chem. Bio.* 13, 75–80.
- (23) Piraner, D. I., Wu, Y., and Shapiro, M. G. (2019) Modular Thermal Control of Protein Dimerization. *ACS Synth. Biol.* 8, 2256–2262.
- (24) Hildebrandt, B., Wust, P., Ahlers, O., Dieing, A., Sreenivasa, G., Kerner, T., Felix, R., and Riess, H. (2002) The cellular and molecular basis of hyperthermia. *Crit. Rev. Oncol. Hemat.* 43, 33–56.

- (25) Rome, C., Couillaud, F., and Moonen, C. T. W. (2005) Spatial and temporal control of expression of therapeutic genes using heat shock protein promoters. *Methods* 35, 188–198.
- (26) Wada, K.-I., Taniguchi, A., and Okano, T. (2007) Highly sensitive detection of cytotoxicity using a modified HSP70B' promoter. *Biotechnol. Bioeng.* 97, 871–876.
- (27) Kay, R. J., Boissy, R. J., Russnak, R. H., and Candido, E. P. (1986) Efficient transcription of a *Caenorhabditis elegans* heat shock gene pair in mouse fibroblasts is dependent on multiple promoter elements which can function bidirectionally. *Mol. Cell. Biol.* 6, 3134–3143.
- (28) Miller, I. C., Gamboa Castro, M., Maenza, J., Weis, J. P., and Kwong, G. A. (2018) Remote Control of Mammalian Cells with Heat-Triggered Gene Switches and Photothermal Pulse Trains. *ACS Synth. Biol.* 7, 1167–1173.
- (29) Ferreira, J. P., Overton, K. W., and Wang, C. L. (2013) Tuning gene expression with synthetic upstream open reading frames. *Proc. Natl. Acad. Sci. U. S. A.* 110, 11284–11289.
- (30) Yamaguchi, M., Ito, A., Okamoto, N., Kawabe, Y., and Kamihira, M. (2012) Heat-inducible transgene expression system incorporating a positive feedback loop of transcriptional amplification for hyperthermia-induced gene therapy. *J. Biosci. Bioeng.* 114, 460–465.
- (31) Sndergaard, H., and Skak, K. (2009) IL-21: roles in immunopathology and cancer therapy. *Tissue Antigens* 74, 467–479.
- (32) Singh, H., Figliola, M. J., Dawson, M. J., Huls, H., Olivares, S., Switzer, K., Mi, T., Maiti, S., Kebriaci, P., Lee, D. A., Champlin, R. E., and Cooper, L. J. N. (2011) Reprogramming CD19- Specific T Cells with IL-21 Signaling Can Improve Adoptive Immunotherapy of B-Lineage Malignancies. *Cancer Res.* 71, 3516–3527.
- (33) Parrish-Novak, J., Dillon, S. R., Nelson, A., Hammond, A., Sprecher, C., Gross, J. A., Johnston, J., Madden, K., Xu, W., West, J., Schrader, S., Burkhead, S., Heipel, M., Brandt, C., Kuijper, J. L., Kramer, J., Conklin, D., Presnell, S. R., Berry, J., Shiota, F., Bort, S., Hambly, K., Mudri, S., Clegg, C., Moore, M., Grant, F. J., Lofton-Day, C., Gilbert, T., Raymond, F., Ching, A., Yao, L., Smith, D., Webster, P., Whitmore, T., Maurer, M., Kaushansky, K., Holly, R. D., and Foster, D. (2000) Interleukin 21 and its receptor are involved in NK cell expansion and regulation of lymphocyte function. *Nature* 408, 57–63.
- (34) Xu, Y., Hyun, Y.-M., Lim, K., Lee, H., Cummings, R. J., Gerber, S. A., Bae, S., Cho, T. Y., Lord, E. M., and Kim, M. (2014) Optogenetic control of chemokine receptor signal and T-cell migration. *Proc. Natl. Acad. Sci. U.S.A.* 111, 6371–6376.
- (35) McDannold, N. J., King, R. L., Jolesz, F. A., and Hynynen, K. H. (2000) Usefulness of MR Imaging-Derived Thermometry and Dosimetry in Determining the Threshold for Tissue Damage Induced by Thermal Surgery in Rabbits. *Radiology* 216, 517–523.
- (36) McDannold, N., Vykhodtseva, N., Jolesz, F. A., & Hynynen, K. (2004) MRI investigation of the threshold for thermally induced blood-brain barrier disruption and brain tissue damage in the rabbit brain. *Magn. Reson. Med.* 51, 913–923.
- (37) Kregel, K. C. (2002) Invited Review: Heat shock proteins: modifying factors in physiological stress responses and acquired thermotolerance. *J. Appl. Physiol.* 92, 2177–2186.

(38) Morimoto, R. I. (1998) Regulation of the heat shock transcriptional response: cross talk between a family of heat shock factors, molecular chaperones, and negative regulators. *Genes Dev.* 12, 3788–3796.

*Chapter 3*BIOMOLECULAR ULTRASOUND IMAGING OF PHAGOLYSOSOMAL  
FUNCTION

Ling, B.; Lee, J.; Maresca, D.; Lee-Gosselin, A.; Malounda, D.; Swift, M. B.; Shapiro, M. G. Biomolecular ultrasound imaging of phagolysosomal function. *ACS Nano*, 2020, 14 (9), 12210-12221.

This chapter is a reformatted version of the above publication. My contributions to the work were conceiving and performing *in vitro* macrophage gas vesicle loading and characterization, analyzing data, and preparing the manuscript together with the other authors.

**3.1 Abstract**

Phagocytic clearance and lysosomal processing of pathogens and debris are essential functions of the innate immune system. However, the assessment of these functions *in vivo* is challenging because most nanoscale contrast agents compatible with non-invasive imaging techniques are made from non-biodegradable synthetic materials that do not undergo regular lysosomal degradation. To overcome this challenge, we describe the use of an all-protein contrast agent to directly visualize and quantify phagocytic and lysosomal activities *in vivo* by ultrasound imaging. This contrast agent is based on gas vesicles (GVs), a class of air-filled protein nanostructures naturally expressed by buoyant microbes. Using a combination of ultrasound imaging, pharmacology, immunohistology and live-cell optical microscopy, we show that after intravenous injection, GVs are cleared from circulation by liver-resident macrophages. Once internalized, the GVs undergo lysosomal degradation, resulting in the

elimination of their ultrasound contrast. By non-invasively monitoring the temporal dynamics of GV-generated ultrasound signal in circulation and in the liver and fitting them with a pharmacokinetic model, we can quantify the rates of phagocytosis and lysosomal degradation in living animals. We demonstrate the utility of this method by showing how these rates are perturbed in two models of liver dysfunction: phagocyte deficiency and non-alcoholic fatty liver disease. The combination of proteolytically-degradable nanoscale contrast agents and quantitative ultrasound imaging thus enables non-invasive functional imaging of cellular degradative processes.

### **3.2 Introduction**

The reticuloendothelial system (RES), also known as the mononuclear phagocyte system, is a network of phagocytic immune cells that is essential for organismal development and homeostasis; malfunctions in this system may lead to increased susceptibility to infections<sup>1,2</sup> and are associated with the pathogenesis of a variety of conditions, including neurodegeneration,<sup>3,4</sup> chronic liver disease<sup>5</sup> and many others.<sup>6</sup> Cells of the RES, such as monocytes, macrophages and dendritic cells, continuously sample their surroundings, mediating the recognition and clearance of abnormal and senescent cells, debris and foreign particulates.<sup>7,8</sup> Additionally, they interface with the adaptive immune system by presenting lysosomally-processed antigens to lymphocytes and secreting cytokines to stimulate the proper inflammatory response.<sup>8-10</sup> Phagocytosis and lysosomal degradation are thus vital processes of RES-mediated immunoregulation.

Non-invasive functional imaging of phagocytosis and lysosomal activities will enable early detection and monitoring of non-alcoholic fatty liver disease (NAFLD) and other conditions

resulting from RES dysfunction. NAFLD currently affects over 25% of the global population and its progression is associated with chronic hepatic inflammation.<sup>11</sup> Due to the large patient population and broad range of outcomes which include hepatitis, cirrhosis, fibrosis and hepatocellular carcinoma, rapid and non-invasive diagnostic methods are needed to stratify patients into defined risk groups.<sup>5,11</sup> Ultrasound is well suited for this task due to its wide availability, portability, low operational costs and high tissue penetrance.<sup>12</sup> Based on *in vitro* observations that pro-inflammatory macrophages suppress phagocytosis<sup>13</sup> and lysosomal degradation,<sup>14,15</sup> one would expect livers in patients with NAFLD to exhibit reduced accumulation and extended persistence of intravenously-administered nanoscale contrast agents. Indeed, clinical studies have confirmed the former.<sup>16,17</sup> However, the latter cannot be evaluated with currently available technologies because agents compatible with non-invasive imaging modalities are typically made from synthetic materials which do not undergo regular lysosomal degradation.<sup>7,8</sup>

Here, we describe the use of an all-protein nanoscale contrast agent to visualize and quantify both phagocytic clearance and lysosomal degradation *in vivo* using ultrasound imaging. This contrast agent is based on gas vesicles (GVs), a class of air-filled protein nanostructures natively formed inside certain photosynthetic microorganisms as a means to regulate buoyancy.<sup>18</sup> GVs comprise a rigid, 2 nm-thick protein shell allowing the free exchange of gas but preventing the internal condensation of liquid water, thereby forming a thermodynamically stable capsule of air with a hydrodynamic diameter of approximately 250 nm.<sup>19</sup> They are easily isolated from cultures of their native cyanobacterial hosts<sup>20</sup> and can be expressed heterologously in bacteria<sup>21,22</sup> and mammalian cells.<sup>23</sup> Because sound waves are strongly reflected by air-water interfaces, GVs have been developed as contrast agents for

ultrasound imaging.<sup>19, 24-27</sup> Due to their innate stability, GVs are able to withstand repeated insonation without loss of contrast.<sup>19</sup> However, when the GV shell is compromised by mechanical or chemical disruption, the gaseous contents it encloses rapidly and irreversibly dissolve into the surrounding media, leading to the elimination of ultrasound contrast.<sup>19,21,27</sup> Based on their nanoscale dimensions and all-protein composition, which distinguishes them from other classes of ultrasound contrast agents<sup>28-31</sup>, we hypothesized that we could use GVs as a contrast agent to non-invasively visualize the phagocytic and lysosomal functions of hepatic macrophages *in vivo*. Previous studies have shown that intravenously injected GVs are rapidly taken up by the liver.<sup>32,33</sup> If this uptake is mediated by macrophages and the internalized GVs undergo lysosomal proteolysis, this would manifest in the initial transfer of ultrasound contrast from the bloodstream to the liver, followed by its elimination with kinetics representative of natural RES clearance and degradation. Measurement of these processes would thus provide a quantitative picture of the complete phagocytic and lysosomal degradation pathways. This rate-based approach would improve upon previous Kupffer cell imaging techniques<sup>16,34-36</sup> which are limited to the assessment of phagocytosis. In this study, we test this hypothesis by visualizing the temporal dynamics of GV ultrasound contrast in the blood and liver, establishing the cellular and molecular pathways mediating GV uptake and degradation, and developing a pharmacokinetic model to parametrize RES activity from hemodynamic and liver ultrasound signals. Finally, we demonstrate the diagnostic utility of functional imaging of macrophage phagolysosomal activity in two models of liver disease: clodronate-mediated macrophage deficiency and diet-induced NAFLD.

### 3.3 Results and Discussion

#### 3.3.1 Gas vesicle blood clearance, liver uptake and degradation can be monitored by ultrasound

We started by quantifying the kinetics of GV uptake and degradation in healthy C57BL/6 mice (**Fig. 3-1a**). We first visualized intravascular GVs with ultrafast power Doppler imaging, leveraging the ability of intravenously (IV) injected GVs to enhance blood flow contrast.<sup>25</sup> We chose the brain as our target organ due to its practical advantages in mouse experiments: hemodynamic signals can be conveniently measured through intact skin and skull<sup>25,37</sup> and head-fixation reduces motion artifacts. We acquired images of a single coronal plane at a center frequency of 15 MHz and frame rate of 0.25 Hz (**Fig. 3-1b**). Following a 300-s baseline, we IV injected 100  $\mu\text{L}$  of purified GVs isolated from *Anabaena flos-aquae* ( $\text{OD}_{500}30$ , corresponding to  $2.1 \times 10^{11}$  particles<sup>20</sup>) and tracked the ensuing distribution and clearance (**Fig. 3-1c**). As expected, the introduction of GVs caused a marked increase in hemodynamic signal, peaking at approximately 100 s after injection, and returning to baseline with an apparent circulation half-life of 232 s (**Fig. 3-1c, Fig. 3-S1**).

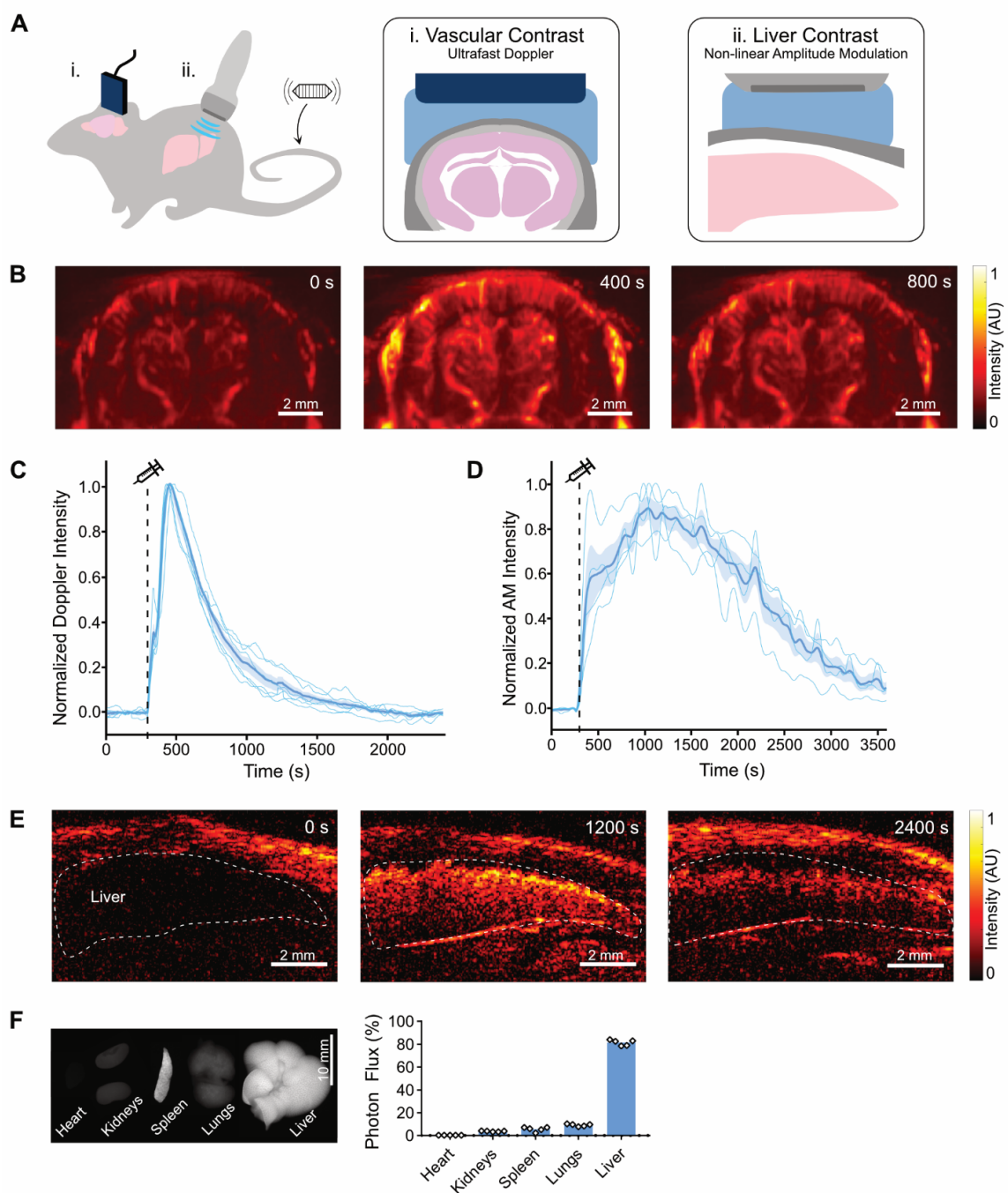


**Figure 3-1:** Non-invasive ultrasound imaging of GV clearance and elimination in vivo. **A)** Diagram of imaging setups used to measure GV contrast in the blood and liver. Inset i, intravascular persistence of purified GVs was visualized by ultrafast power Doppler imaging of the brain. Inset ii, hepatic persistence of GVs modified to produce non-linear contrast was visualized by amplitude modulation imaging of the liver. **B)** Representative power Doppler images of a coronal cross section of the brain following GV injection. Scale bars, 2 mm. **C-D)** Normalized time courses of ultrafast Doppler signal enhancement in the brain (**C**,  $N = 6$ ) and AM signal in the liver (**D**,  $N = 4$ ). Dashed lines, time of GV

injection (300 s); thin lines, individual trials; thick lines, mean; shaded areas,  $\pm$  SEM. **E)** Representative AM images of a liver cross section following GV injection. Scale bars, 2 mm. **F)** Biodistribution of fluorescently-labeled GVs 1 h after IV injection. Representative fluorescence image of excised organs (left; scale bar, 10 mm). Percentage of total collected photons originating from each organ (right). N = 5. Error bars not shown.

Next, we quantified GV uptake and degradation in the liver by imaging this organ during and after IV injection (**Fig. 3-1a**). To maximize GV specificity, we injected GVs modified to produce non-linear ultrasound contrast<sup>27</sup> and imaged with a non-linear amplitude modulation (AM) pulse sequence<sup>24</sup> (**Fig. 3-1, d-e**). Following injection of 100  $\mu$ L GVs at OD<sub>500</sub> 30, we observed the accumulation of non-linear contrast in the liver—reaching a maximum after approximately 10 min—followed by a gradual loss of signal until only 10% remained at the end of one hour (**Fig. 3-1d**). Notably, the maximum occurs just as contrast in the blood returns to baseline (**Fig. 3-S2**). The apparent half-life of GVs in the liver—20 min—is substantially longer than their circulation time, and on a timescale consistent with lysosomal processing.<sup>38-40</sup> To independently confirm liver uptake, we acquired fluorescence images of mouse organs excised 1h after IV injection of GVs labeled with a far-red fluorescent dye (**Fig. 3-1f**). In line with previous investigations of GV biodistribution,<sup>32,33</sup> the liver was the dominant organ for GV uptake, emitting 81.4% of collected photons. The lungs (7.8%) and spleen (5.5%) had minor roles in GV clearance, while the heart and kidneys had no discernible role.

### 3.3.2 GVs are primarily cleared by liver macrophages

To identify the cells involved in GV clearance, we performed immunofluorescence imaging of liver sections obtained from mice perfused 1h after IV injection of fluorescently-labeled

GVs (**Fig. 3-2a**). Based on the apparent active degradation of GVs, as suggested by the gradual decline of liver ultrasound contrast, we hypothesized that GVs would be taken up by Kupffer cells—resident macrophages lining the hepatic sinusoids which are implicated in the clearance of many nanoparticles.<sup>7</sup> We tested this hypothesis by defining antibody-stained F4/80<sup>+</sup> Kupffer cell regions through image segmentation by Ilastik<sup>41</sup> and quantifying the localization of GVs with respect to these borders (**Fig. 3-S3**). On average, 60% of GV-containing pixels resided within Kupffer cells (**Fig. 3-2b**).

To confirm the role of Kupffer cells in GV clearance, we ablated phagocytic cells by IV administration of 30 mg/kg liposome-encapsulated clodronate<sup>42</sup> (**Fig. 3-2c**). 48h later, we measured GV circulation times with hemodynamic ultrasound (**Fig. 3-2d**). Compared to mice treated with saline-filled control liposomes, clodronate-treated mice had a nearly 7-fold enhancement in GV circulation time, with half-life increasing from 274 s to 1670 s (**Fig. 3-S2**). Our results are in line with previous observations that treatment with 50 mg/kg clodronate increased the circulation half-life of 100 nm gold nanoparticles 13-fold.<sup>1</sup> Taken together, our data shows that GVs are mainly filtered from the blood by Kupffer cells.

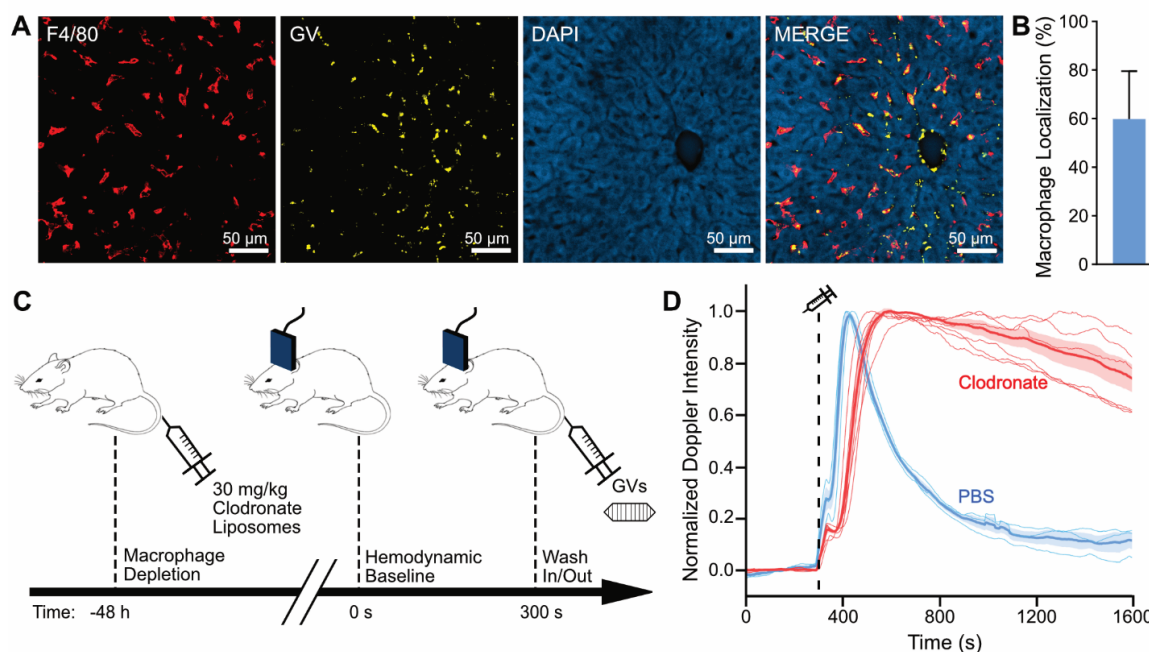


**Figure 3-2:** Liver macrophages are the primary mediators of GV clearance. **A)** Immunofluorescent confocal micrographs of 75- $\mu\text{m}$  sections of liver tissue obtained from healthy mice 1h after IV injection of fluorescently-labeled GVs. Sections were stained with anti-F4/80 (macrophages) and DAPI. Scale bars, 50  $\mu\text{m}$ . **B)** Percentage of detected GVs found within macrophage regions based on segmentation with ilastik. Error bars indicate  $\pm$  SD. N = 3 biological replicates, 78 total fields of view. **C)** Experimental timeline. Macrophages were depleted by IV injection of 30 mg/kg liposomal clodronate 48 h before GV injection. **D)** Normalized Doppler signal enhancement time courses following IV injection of GVs in mice pre-treated with clodronate (red, N = 6) or saline liposomes (blue, N = 3). Dashed line, time of GV injection (300 s); thin lines, individual trials; thick lines, mean; shaded areas,  $\pm$  SEM.

### 3.3.3 GVs are degraded in the lysosome following phagocytosis

Having established their uptake by liver macrophages, we next studied what happens to GVs following phagocytosis. Macrophages typically internalize nanoparticles into membrane-bound organelles—phagosomes—that are then trafficked along the phagolysosomal pathway. During this maturation process, the phagosomes acquire v-ATPase proton pumps to acidify their contents prior to fusion with the lysosome;<sup>43</sup> this low pH environment is required for lysosomal enzyme activity. To visualize the movement of GVs along this

pathway *in vitro*, we incubated murine macrophages (RAW264.7) with a dilute suspension of GVs dually-labeled with Alexa Fluor (AF647) and pHrodo Red—a pH-sensitive dye that fluoresces weakly at pH 7 and brightly at pH 3—and imaged them with live-cell confocal optical microscopy (**Fig. 3-3a**). Focusing on individual cells, we initially observed punctate spots of AF647 signal, likely corresponding to GVs concentrated within phagosomes, which matured over the next several minutes to produce strong pHrodo signal, indicating acidification of their environment (**Fig. 3-3b**). Zooming out to observe population-level dynamics revealed that the proportion of GVs in acidified compartments, as parametrized by the ratio of pHrodo to AF647 signal, grew continuously during a 1-hour incubation (**Fig. 3-3, c-d**). This rise was abolished when v-ATPase was inhibited by pretreatment with 100 nM bafilomycin A1 (BafA1),<sup>44</sup> thereby confirming that GVs undergo phagolysosomal processing in macrophages.

Lysosomal proteolysis is expected to break down the GV shell, resulting in GV collapse, gas dissolution and the disappearance of ultrasound contrast. To confirm this effect *in vitro*, we exposed RAW264.7 cells to GVs for 30 min. At predetermined time intervals, we detached the cells from their solid substrate and loaded them into an agarose phantom for imaging with a non-linear cross-propagating amplitude modulation pulse sequence (xAM)<sup>26</sup> (**Fig. 3-3e**). In control cells pretreated with 0.01% v/v dimethyl sulfoxide (DMSO), the signal declined with a half-life of approximately 3 h (**Fig. 3-3, f-g**). Conversely, in cells pretreated with BafA1 to block the activity of the pH-dependent lysosomal enzymes, we observed signal that persisted for at least 5 h without decay. These results confirm that GVs are digested within macrophage lysosomes in a process that can be monitored with non-linear ultrasound imaging. The reason

that this process happens somewhat more slowly in vitro compared to the liver may be the accelerated rate of phagosome maturation in primary macrophages<sup>45</sup>.

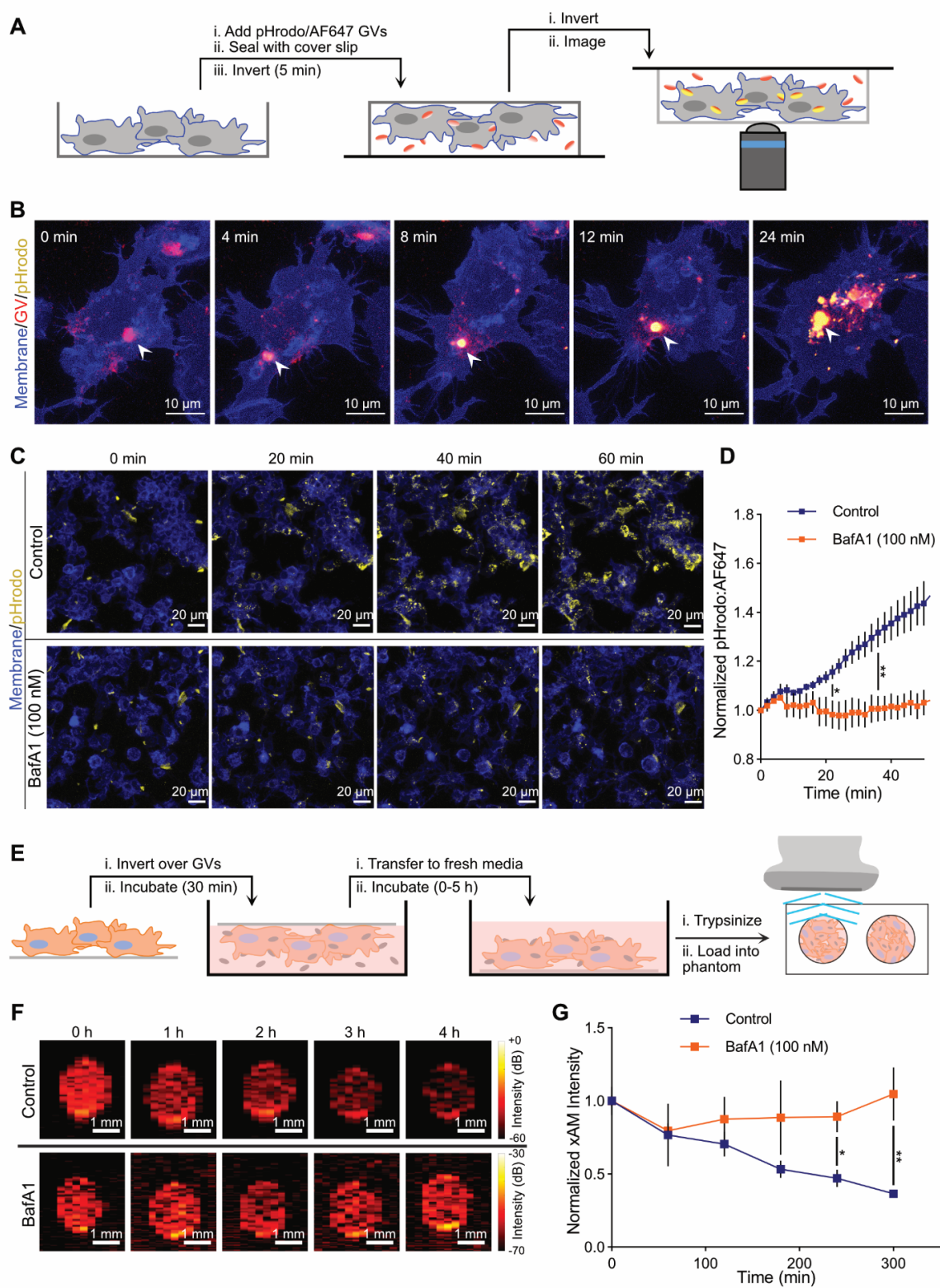


**Figure 3-3:** Internalized GVs are degraded within lysosomes, resulting in loss of ultrasound contrast. **A)** Diagram of live cell confocal microscopy protocol. Murine macrophages (RAW264.7) expressing membrane-localized fluorescent protein (blue) were incubated with GVs dually-labeled with AF647 (red) and pHrodo (yellow) to track localization and pH, respectively. **B)** Representative images of a single cell at different time points following GV uptake. A phagosome maturation event is indicated by the white arrows. Scale bars, 10  $\mu\text{m}$  (63x objective). **C)** Representative population-level images of cells pre-treated with DMSO (top) or 100 nM bafilomycin A1 (bottom) following GV uptake. The AF647 channel is not shown. Scale bars, 20  $\mu\text{m}$  (20x objective). **D)** Ratio of pHrodo to AF647 signals in images from **c**, normalized to the initial timepoint. Error bars represent  $\pm$  SEM. N = 4. Welch's t test (\*:  $p < 0.05$ ; \*\*:  $p < 0.001$ ). **E)** Diagram of uptake protocol for ultrasound imaging. RAW264.7 cells were incubated for 30 min with GVs modified to produce non-linear signal, transferred to GV-free media for predetermined periods of time, and loaded into an agarose phantom for non-linear xAM imaging. **F)** Representative xAM images of cell pellets pre-treated with DMSO (top) or 100 nM bafilomycin A1 (bottom) at the indicated times after GV uptake. Scale bars, 1 mm. **G)** Time course of xAM signal intensity in cell pellets, normalized to the initial timepoint. Error bars represent  $\pm$  SEM. N = 4-10 per timepoint. Welch's t-test (\*:  $p < 0.05$ ; \*\*:  $p < 0.01$ ).

### 3.3.4 GV pharmacokinetics can be used to monitor disease progression

The results presented thus far confirm that upon IV injection, GVs are filtered from the blood by liver macrophages and subsequently catabolized in the lysosome (**Fig. 3-4a**). This process can be described with a two-compartment pharmacokinetic model comprising the blood and liver, whose rate constants parametrize the concurrent processes of phagocytosis and lysosomal degradation (**Fig. 3-4b**), with contrast enhancement linearly proportional to intact GV concentration in each compartment (**Fig. 3-S4**). By fitting this model to the dynamics of GV ultrasound contrast in the vasculature and liver *in vivo*, we can thus non-invasively quantify macrophage phagolysosomal function (**Fig. 3-4c**, input data shown in **Fig. 3-S5**). The assumption that ultrasound signal time courses are representative of true pharmacokinetics is based on two key observations: GVs are stable under our imaging parameters, so changes in signal are due to active biological processes; and GVs are primarily taken up by liver macrophages, with increases in liver AM contrast matched by decreases in brain Doppler contrast. For simplicity, we further assume each process to be first-order and

neglect the initial distribution dynamics during GV infusion by considering timepoints occurring after the peak in Doppler signal. Using this approach, we calculated rates of  $0.167 \text{ min}^{-1}$  and  $0.041 \text{ min}^{-1}$  for uptake and degradation, respectively, in healthy mice (**Fig. 3-4d**, **Table 3-S1**).

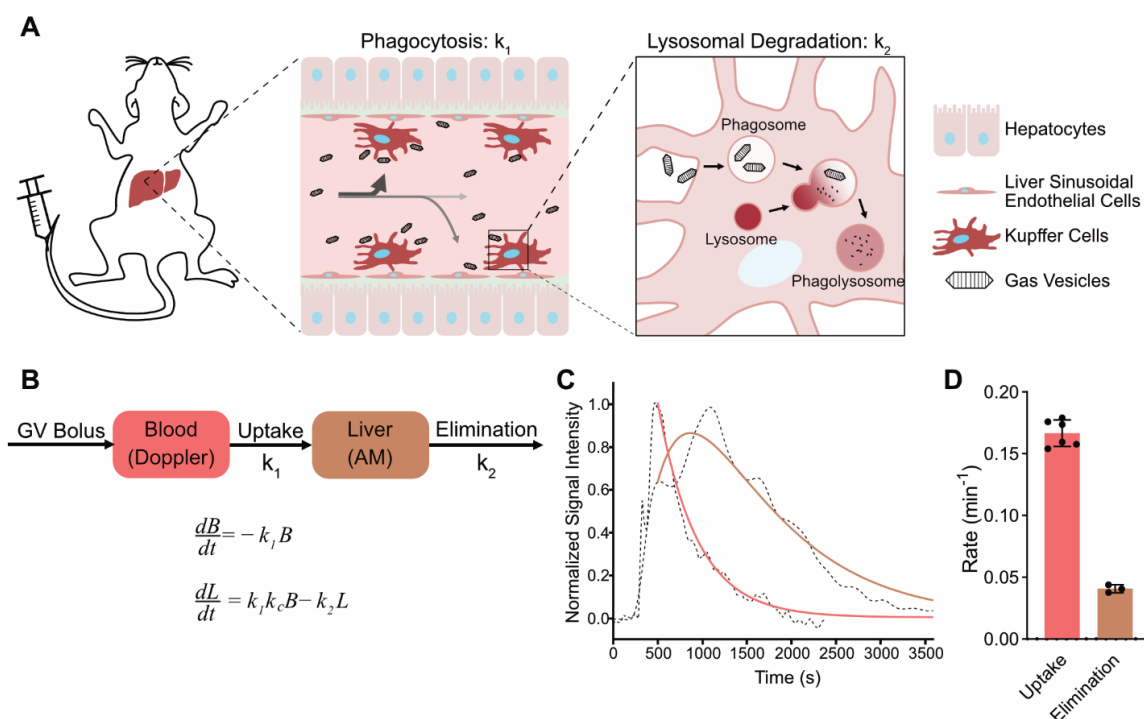


**Figure 3-4:** Quantification of phagocytic and lysosomal activities in mouse liver macrophages. **A)** Proposed GV clearance pathway. Upon IV infusion, GVs are phagocytosed from the blood by liver-resident macrophages and degraded by lysosomal proteolysis. **B)** Pharmacokinetic model of GV clearance. Fitting this model to GV signal time courses enables quantification of macrophage function. Uptake and degradation rates are represented by  $k_1$  and  $k_2$ , respectively, and  $k_c$  is a correction factor that enables conversion between the two imaging modes and accounts for uptake in other tissues. **C)** Representative plot of vascular and liver ultrasound signal time courses in healthy mice (dashed lines) and corresponding fitted curves (solid lines). **D)** Uptake and elimination rates obtained by fitting model to data from Fig. 3-1, c-d. Error bars represent  $\pm$  SD.

Having established a method to quantify liver macrophage function, we next evaluated its ability to detect pathological disruption of the RES. First, we administered two doses of liposomal clodronate— $0.40 \text{ mg/kg}$  and  $30 \text{ mg/kg}$ —to partially or fully deplete Kupffer cells

in the liver. Histological evaluation confirmed that 31% of the Kupffer cell population remained at the lower dose, decreasing to 16% at the higher dose (**Fig. 3-5a**; **Fig. 3-S6**). Interestingly, *ex vivo* imaging of organ fluorescence revealed that most GVs are still cleared by the liver (**Fig. 3-5b**). However, closer inspection of liver sections with immunofluorescence showed GVs tending to localize to the sinusoidal margins, suggesting uptake by liver sinusoidal endothelial cells (LSECs) (**Fig. 3-S7**). This is consistent with a recent study showing that LSECs upregulate phagocytic activity upon depletion of nearby Kupffer cells.<sup>7</sup> Based on these results, we expected that GVs would circulate longer in the blood in clodronate-treated animals due to diminished phagocytic potential, and that their residence time in the liver would increase due to less efficient lysosomal degradation by non-macrophage cells. Indeed, fitting our model to the normalized hemodynamic Doppler (**Fig. 3-5c**) and liver AM (**Fig. 3-5d**) signal time courses yielded uptake and degradation rates substantially lower than those of healthy mice (**Fig. 3-5e**). Specifically, phagocytosis rates were reduced by 66% and 82% at the low and high doses of clodronate, while proteolysis rates were reduced by 27% and 57%, respectively. Notably, phagocytosis rates were proportional to the macrophage population.

For our second model of RES dysfunction, we imaged mice with NAFLD. This disease is characterized by liver infiltration of pro-inflammatory M1-polarized macrophages<sup>5,46</sup> which have lower phagocytic<sup>13,17,34,47</sup> and lysosomal activities<sup>15</sup> than the normally anti-inflammatory Kupffer cells.<sup>48</sup> We induced NAFLD by feeding mice with a methionine- and choline-deficient (MCD) diet<sup>5,49</sup> and performed ultrasound imaging after 4 weeks of this treatment (**Fig. 3-5f**). Histological evaluation confirmed the appearance of widespread steatosis, a hallmark of NAFLD (**Fig. 3-5f**). In line with our hypothesis, diseased mice had

significantly suppressed phagocytic and lysosomal functions: uptake rate was reduced by 35% while degradation rate was reduced by 58% (**Fig. 3-5, g-i**). We verified that these differences are not due to saturation of the smaller livers of MCD mice<sup>50</sup> by GVs (**Fig. 3-S8**). When we simulated therapeutic intervention by reverting to a control diet for 3 additional weeks, the steatosis subsided (**Fig. 3-5f**) and phagolysosomal activity returned to its original level (**Fig. 3-5, g-i**). Compared to age-matched litter-mate controls, these “recovered” mice showed a slight decrease in degradation rate but no discrepancies in uptake rate (**Fig. 3-S9, Table 3-S1**). Taken together, our results demonstrate the capability of GV-enhanced ultrasound to non-invasively visualize macrophage malfunction as a biomarker of disease.

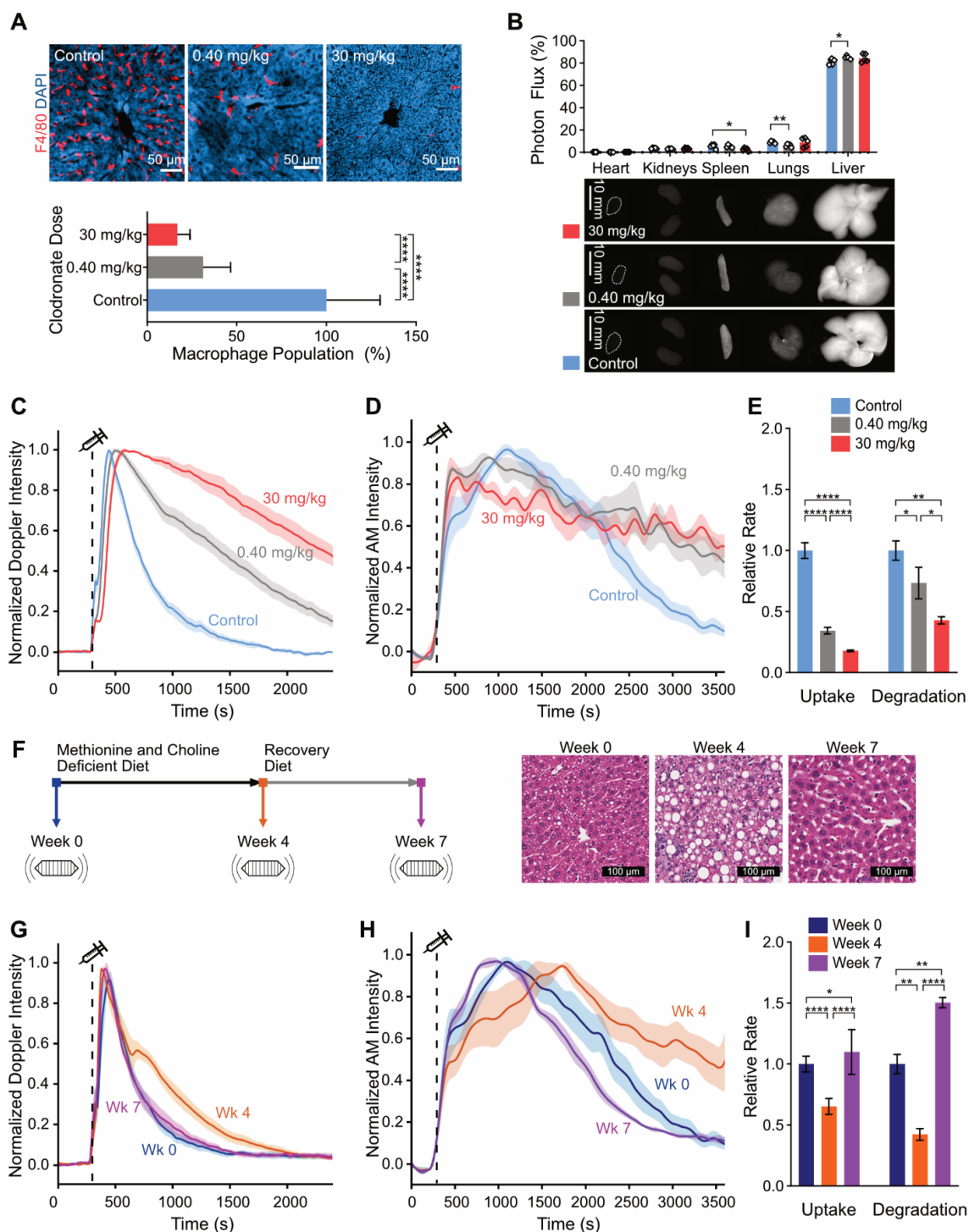


**Figure 3-5:** Monitoring disease progression by functional imaging of phagolysosomal activity. **A)** Macrophage population in response to clodronate dose. Top: Representative immunofluorescence confocal micrographs of liver sections labeled with anti-F4/80 (macrophages) and DAPI. Scale bars, 50  $\mu$ m. Bottom: Macrophage population determined by segmentation with ilastik, normalized to the mean from control livers. Error bars represent  $\pm$  SD. N = 3 biological replicates, >100 total

fields of view. Welch's t-test (\*\*\*\*:  $p < 0.0001$ ). **B**) Biodistribution of fluorescently-labeled GVs 1h after injection. Bottom: Representative fluorescence images of excised organs. Due to their low fluorescence, the hearts are circled with dashed lines. Scale bars, 10 mm. Top: Percentage of collected photons originating from each organ. Error bars not shown.  $N = 5$ . Welch's t-test (\*:  $p < 0.05$ ; \*\*:  $p < 0.001$ ). **C-D**) Normalized time courses of Doppler signal enhancement in the brain (**C**) and AM signal in the liver (**D**) following GV injection in clodronate-treated mice. Dashed lines, time of GV injection (300 s); thick lines, mean; shaded areas,  $\pm$  SEM.  $N = 4-6$ . **E**) Uptake and degradation rates obtained by fitting the model in Fig. 4b to each distinct combination of time courses from **C** and **D**, normalized to those of healthy mice. Error bars represent  $\pm$  SD. Welch's t-test (\*:  $p < 0.05$ ; \*\*:  $p < 0.01$ ; \*\*\*:  $p < 0.001$ ; \*\*\*\*:  $p < 0.0001$ ). **F**) Left: Timeline of NAFLD induction. Mice were fed with a methionine and choline deficient diet for 4 weeks, followed by an additional 3 weeks with a control diet. Right: Representative images of H&E stained liver sections. Scale bars, 100  $\mu$ m. **G-H**) Normalized time courses of Doppler signal enhancement in the brain (**G**) and AM signal in the liver (**H**) following GV injection in mice with NAFLD. Dashed lines, time of GV injection (300 s); thick lines, mean; shaded areas,  $\pm$  SEM.  $N = 4-5$ . **I**, Uptake and degradation rates obtained by fitting the model in Fig. 4b to the time courses in **G** and **H**, normalized to those of healthy (Week 0) mice. Error bars represent  $\pm$  SD. Welch's t-test (\*\*:  $p < 0.01$ ; n.s:  $p > 0.05$ ).

### 3.4 Conclusions

GVs are advantageously positioned to image *in vivo* phagolysosomal function due to their inherent stability at ambient conditions, susceptibility to natural proteolytic degradation and dependence on shell integrity for ultrasound contrast. When combined with a simple pharmacokinetic model, GV imaging makes it possible to parametrize macrophage activity in terms of phagocytosis and lysosomal degradation rates, clearly delineating healthy and disease states, as demonstrated in two models of RES deficiency.

The diagnostic power of macrophage functional imaging arises from the dependence of phagolysosomal kinetics on cellular phenotype which, in turn, reflects the local tissue and inflammatory microenvironment. Moving forward, this capability could be refined by application of GVs engineered to display surface ligands,<sup>27</sup> as phenotype-specific responses to certain particle-bound domains may augment differences in degradative behavior.<sup>51</sup> Methods to alter GV biodistribution would enable targeting and functional assessment of

macrophages in tissues other than the liver. Additionally, the ability to genetically express GVs<sup>23</sup> could enable study of intracellular proteolytic processes, such as autophagy and proteasomal degradation.

To maximize the translational utility of this technology, three aspects could be improved. First, imaging parameters should be optimized for clinical use. In this study, we separately acquired ultrafast Doppler and non-linear AM images to maximize signal specificity. However, simultaneous multiplexed imaging of blood and liver signals would greatly streamline diagnostic use. This could be accomplished by intercalating amplitude modulation images with Doppler images of the liver, enabling GV quantitation in both compartments with a single, stationary transducer. Second, while GV administration at doses similar to those used in our experiments does not result in acute, adverse health effects in mice,<sup>19</sup> clinical translation would require formal studies of dose-limiting and long-term toxicity. In addition, to support long-term monitoring of individual subjects, it would be useful to better understand the immunogenicity of GVs and the impact of repeated injections, as the development of antibodies may skew clearance kinetics.<sup>52</sup> Finally, in some applications it may be useful to image GVs with other imaging modalities, such as magnetic resonance imaging<sup>28,29</sup> and optical coherence tomography;<sup>53</sup> adaptation of phagolysosomal imaging to these modalities would facilitate applications where the efficacy of ultrasound may be limited.

In summary, the combination of nanoscale, lysosomally-degradable contrast agents and quantitative ultrasound imaging enables non-invasive assessment of macrophage function as a disease-relevant biomarker. This technology will broaden the diagnostic capabilities of

biomolecular ultrasound and motivate further methods for non-invasive characterization of cellular function.

### 3.5 Methods

#### GV preparation and quantification

Native gas vesicles (GVs) were isolated from *Anabaena flos-aquae* as previously described.<sup>20</sup> Concentrations were measured by optical density (OD) at 500 nm using a spectrophotometer (NanoDrop ND-1000, Thermo Scientific). Stripped GV s were prepared by treatment of native GV s with 6M urea solution followed by two rounds of centrifugally-assisted flotation and removal of the supernatant.<sup>20</sup> Fluorescently-labeled gas vesicles were prepared by mixing GV s at OD 10 in 1x phosphate-buffered saline (PBS) with 6  $\mu$ M Alexa Fluor 647 NHS Ester (Invitrogen, prepared as 10 mM solution in dimethyl sulfoxide). Dually-labeled GV s were prepared by mixing GV s at OD10 with 6  $\mu$ M pHrodo Red succinimidyl ester (Invitrogen, prepared as 10 mM solution in dimethyl sulfoxide) and 18  $\mu$ M Alexa Fluor 647 NHS Ester (Invitrogen, prepared as 10 mM solution in dimethyl sulfoxide). After rotating in the dark at 25°C for 1 h, the reactions were quenched with Tris-HCl. Prior to use, all GV s were buffer exchanged into 1x PBS by two rounds of overnight dialysis through a regenerated cellulose membrane (12-14 kD MWCO, Repligen).

#### Cell culture

RAW264.7 (TIB-71) and HEK293T (CRL-3216) cells were ordered from the American Type Culture Collection (ATCC). Cells were cultured on tissue culture treated 10-cm dishes in Dulbecco's Modified Eagle Medium (DMEM) supplemented with 10% Fetal Bovine Serum and 1% penicillin/streptomycin.

*Lentiviral transduction.* Plasmid constructs were designed with SnapGene (GSL Biotech) and assembled with Gibson Assembly reagents from New England Biolabs. Briefly, mWasabi<sup>54</sup> was inserted downstream of a 20-AA palmitoylation tag from GAP43 and expressed under the EF-1 $\alpha$  promoter (gift from Dan I. Piraner<sup>55</sup>). This plasmid was then transfected along with third-generation lentiviral vector and helper plasmids (kind gifts from

the laboratory of David Baltimore) into HEK293T cells using polyethyleneimine (PEI). Following a 12 h incubation, PEI-containing media was replaced with fresh media supplemented with 10 mM sodium butyrate (Sigma Aldrich). Viral particles were concentrated 48 h later *via* ultracentrifugation. RAW264.7 cells were transduced by spinfection. Briefly, concentrated virus was added to non-tissue culture treated 24-well plates coated with RetroNectin (Takara Bio). Following centrifugation (2,000xg, 2h),  $4 \times 10^5$  RAW264.7 cells in 1 mL media were added to each well. The plates were spun again at 900xg for 50 min before transferring to the incubator. The brightest 10% of cells were selected with a BD FACSAria III (BD Biosciences) at the City of Hope Analytical Cytometry Core Facility.

*Preparation of fibronectin-treated cover slips.* Ethanol sterilized square (22 mm x 22 mm) #1.5H glass cover slips (Thorlabs) were individually placed into the wells of a 6-well plate and immersed in 2 mL PBS containing 10  $\mu$ g fibronectin from bovine plasma (Sigma Aldrich) for 2h at room temperature. The fibronectin solution was then aspirated and the plates stored at 4°C until use. Sterile glass-bottom 35mm dishes (MatTek) were similarly coated with 2.5  $\mu$ g fibronectin in 500  $\mu$ L PBS.

### **Animal preparation and disease models**

All *in vivo* experiments were performed on male C57BL/6J mice (The Jackson Laboratory) under protocols approved by the Institutional Animal Care and Use Committee at the California Institute of Technology.

*Macrophage depletion.* Liposome-encapsulated clodronate (Clodrosome, Encapsula NanoSciences) was administered through the lateral tail vein 48 h prior to imaging. Mice receiving a dose of 30 mg/kg were injected with undiluted liposome suspension, while mice receiving the lower dose of 0.40 mg/kg were injected with liposomes diluted 1:100 with sterile saline. Control mice were injected with the equivalent volume of undiluted PBS liposomes (Encapsome, Encapsula NanoSciences).

*Diet-induced nonalcoholic fatty liver disease.* 8-week old mice were free fed with either a methionine and choline deficient diet (5ADJ, TestDiet) or control diet (5CC7, TestDiet) for up to 4 weeks. Afterwards, all mice were fed the control diet for an additional 3 weeks. Because this dietary protocol often results in dramatic weight loss, the mice were monitored weekly for signs of adverse health. GV pharmacokinetics were measured at 2 weeks, 4 weeks and at the conclusion of the study. Immediately after ultrasound imaging, the mice were fixed *via* sequential transcardial perfusion of PBS and 10% neutral buffered formalin (Sigma Aldrich), and the livers were removed for histological assessment by the UCLA Translational Pathology Core Laboratory. Briefly, 4- $\mu$ m sections were cut from paraffin-embedded organs, stained with hematoxylin & eosin, and imaged at 20x with a Leica Aperio slide scanner.

### **Ultrasound imaging**

*Transcranial ultrafast Doppler imaging.* Mice (8-10 weeks old) were maintained under 1.5% isoflurane anesthesia on a temperature-controlled imaging platform with a rectal probe (Stoelting Co.). Following head depilation (Nair) and insertion of a catheter with a 30-g needle into the lateral tail vein (fixed in place with GLUture), the mice were head-fixed in a stereotaxic frame inside a light- and sound-proofed box on an optical table. A 16 MHz transducer (Vermon) connected to a programmable ultrasound scanner (Verasonics Vantage) was coupled to the head through a column of ultrasound gel (centrifuged at 2000xg, 10 min to remove bubbles). The transducer was positioned to capture a full coronal section at an arbitrary plane along the rostrocaudal axis. Once the internal temperature of the mouse stabilized at 37°C, power Doppler images were acquired every 4 s for up to 60 min using a previously described functional ultrasound script with slight modifications.<sup>25</sup> Briefly, the pulse sequence consisted of 11 tilted plane waves (varying from -10 to 10 degrees), each containing 8-half-cycle emissions at a voltage of 15V (900 kPa peak positive pressure measured in free water tank). An ensemble of 250 coherently compounded frames, collected at a framerate of 500 Hz, was then processed through a singular value decomposition filter to isolate blood signals from tissue motion and generate a single power Doppler image. 300 s after the start of imaging, 100  $\mu$ L OD30 native GVs were infused over 10 s by syringe pump. Pixel-wise signal enhancement was calculated as the ratio of intensity at each time

point relative to its mean intensity in the first 75 frames. Time courses were then extracted by averaging signal enhancement within a manually defined region of interest encompassing the whole brain, processed with a 10-sample moving mean filter and normalized to the global maximum.

*Liver amplitude modulation imaging.* Mice (10-14 weeks) were maintained under 2% isoflurane anesthesia on a mouse heating pad controlled by a rectal probe (TCAT-2LV, Physitemp Instruments). After depilation of the abdomen (Nair) and insertion of a 30-g tail vein catheter, the mice were secured in a supine position with surgical tape. Ultrasound imaging was performed with an 18 MHz, 128-element linear array transducer (L22-14v, Verasonics) mounted on a custom-made manual translation stage and positioned such that the liver was at approximately 8 mm in depth. Once the internal temperature of the mouse stabilized at 37°C, B-mode and amplitude modulation images were simultaneously acquired every 4 s for up to 90 min. All images were reconstructed from 128 focused beam ray lines. Each ray line was transmitted at 18 MHz from a 32-element active aperture with a focal depth of 8 mm and peak positive pressure of 600 kPa (measured in free water tank). B-mode images were reconstructed from a single pulse, while amplitude modulation was implemented by first transmitting a single pulse from the full active aperture, followed by two pulses where the even and odd elements in the active aperture are sequentially silenced.<sup>24</sup> Stripped GV's (OD 30, 100  $\mu$ L) were manually injected as a bolus after 300 s. Image processing and display were performed by internal Verasonics programs. Time courses were calculated as the average signal intensity within a manually defined rectangular region of interest encompassing the liver. To enable comparison, the time courses were smoothed by robust locally weighted-regression using linear least squares, baseline corrected with respect to the first 75 time points and normalized to the global maximum.

*In vitro macrophage imaging.* Wild-type RAW264.7 cells were seeded onto fibronectin-coated cover slips (2e6 cells/2mL DMEM). After 24 h, the culture media was exchanged with fresh DMEM containing bafilomycin A1 (100 nM) or vehicle (0.01% v/v DMSO). Media of the same composition was used for all subsequent steps. Following a 1 h

pretreatment, a GV suspension composed of 320  $\mu\text{L}$  fresh media and 80  $\mu\text{L}$  stripped GVs (OD10 in PBS) was dropped at the center of a UV-sterilized Parafilm-lined 6-well plate and a cover slip was floated on top, cell-side down. This GV suspension was freshly prepared immediately prior to uptake. After incubation at 37°C for 30 min, the cover slips were transferred to pre-warmed fresh media and incubated for the desired amount of time. The media was then aspirated and the cover slips were gently washed once with 2 mL room temperature PBS. Cells were detached with 500  $\mu\text{L}$  0.25% trypsin-EDTA (Genesee Scientific), neutralized with 1 mL media, and pelleted by centrifugation (300xg, 5 min, 4°C). From this point on, special care was taken to minimize exposure of the cells to temperatures above 4°C. The pellet was washed once with 1.4 mL ice-cold PBS and resuspended in 50  $\mu\text{L}$  cold serum-free DMEM with 25 mM HEPES before loading into an ultrasound phantom (1% agarose in PBS). Cell densities were manually counted by hemocytometer.

The phantoms were imaged with a 128-element linear array transducer (L10-4v, Verasonics) mounted on a custom manual translation stage using a previously described cross-propagating amplitude modulation pulse sequence<sup>26</sup> that was modified to acquire single frames. Briefly, each frame consisted of 64 ray lines transmitted at 4V (400 kPa peak positive pressure in water) and 6 MHz from a 65-element aperture. Within the active aperture, amplitude modulation was implemented by sequentially sending a plane wave angled at 19.5° from the first 32 elements, a plane wave angled at -19.5° from the last 32 elements, followed by simultaneous emission of both plane waves. The first 3 frames were saved along with a post-collapse image (after 10 insonations at 30 V). Signal intensities were extracted from manually selected circular regions of interest with diameters of 1.8 mm, baseline corrected by subtraction of signal from the post-collapse image, and adjusted for cell density. The time courses from each run were then normalized to the mean intensity from the samples harvested immediately after uptake ( $t=0$ ).

*GV contrast measurement.* Phantoms were constructed as previously described.<sup>19</sup> Briefly, phantoms were made by embedding stripped GVs in 1% agarose in PBS and imaged with

the same parameters used for liver imaging. Signal intensities were extracted from manually defined regions of interest.

### **Fluorescence imaging**

*Whole organ fluorescence.* Mice were prepared as described above for transcranial neuroimaging, with the only modification being that the GVs were fluorescently-labeled with Alexa Fluor 647. Ninety minutes after GV injection, the mice were transcardially perfused with 30 mL of cold heparinized PBS (10 U/mL, Sigma Aldrich). The heart, lungs, kidneys, spleen, and liver were then carefully excised and stored in ice-cold Fluorobrite DMEM (Gibco) prior to analysis. Images were acquired on a Bio-Rad ChemiDoc MP imaging system using red epi-illumination and a 695/55 nm filter with an exposure time of 0.5 s. Integrated intensities were then calculated using the built-in “Analyze Particles” function in FIJI.

*Immunofluorescence.* Mice were prepared as described above for whole organ fluorescence. Ninety minutes after GV injection, the mice were transcardially perfused with 30 mL of cold heparinized PBS, followed immediately by 20 mL 10% neutral buffered formalin. The liver and spleen were removed and immersed in formalin overnight (4°C). Each organ was then sectioned with a vibrating microtome (75 µm, Compressstome, Precisionary Instruments). Slices were blocked and permeabilized (2h, rt) with PBS containing 10% goat serum (Sigma Aldrich), 0.2% Triton X-100 (Fisher Scientific), and 0.1% sodium azide (Sigma Aldrich). Each slice was stained for macrophages with rat anti-mouse F4/80 (BioLegend, 1:200 dilution, overnight, 4°C) and Alexa Fluor 594 goat anti-rat IgG secondary antibody (2h, rt, 1:400 dilution). The sections were mounted with ProLong Diamond with DAPI (Invitrogen) and allowed to harden overnight before imaging with a Zeiss LSM 800 confocal microscope through a 10x or 20x objective. Imaging parameters prioritized signal specificity over speed. Confocal microscopy images of entire liver slices were background subtracted in FIJI (20 px, rolling ball method). Randomly selected 500 px by 500 px regions of interest—simulating the sampling of arbitrary fields of view—were exported to Ilastik<sup>41</sup> for processing. The “Density Counting” workflow was used to count macrophages (**Fig. S6**). Images were

also segmented into macrophage and non-macrophage regions with the “Pixel Classification” workflow and loaded into MATLAB for colocalization analysis (**Fig. S3**).

*Live-cell imaging.*  $1 \times 10^5$  RAW264.7 cells expressing palmitoylated mWasabi were seeded on fibronectin-treated 35mm glass-bottom dishes. After 24 h, the culture media was exchanged with serum-free Fluorobrite DMEM containing 25 mM HEPES and either 100 nM bafilomycin A1 (Cayman Chemical) or vehicle (0.01% v/v DMSO). Following a 1 h incubation, this media was replaced with a 200  $\mu$ L freshly-prepared suspension of OD 1.2 dually-labeled GVs. The well was then sealed with a UV-sterilized 18mm circular glass cover slip and inverted for 5 min at 37°C to allow for contact and uptake.

Laser scanning confocal images were acquired every 2 min for 1h on a Zeiss LSM 800 microscope with a large incubation chamber maintained at 37°C. High magnification images were acquired through a 63x oil immersion objective. Population level images were acquired through a 20x objective. In both cases, acquisition parameters were set to optimize speed. Image files were loaded into FIJI, visualized by maximum intensity projection, de-speckled with a 1-px median filter and quantified by integration of signal intensities across the entire field of view.

### **Pharmacokinetic modeling**

A two-compartment pharmacokinetic model was implemented in MATLAB as the following system of ordinary differential equations:

$$(1) \frac{dB}{dt} = -k_1 B$$

$$(2) \frac{dL}{dt} = k_1 k_c B - k_2 L$$

where B represents GV contrast in the blood and L represents GV contrast in the liver. These variables were then directly parametrized with normalized Doppler and AM signal time courses, respectively, and the constants were derived by non-linear least squares curve fitting with initial values of 0 and bounds of 0 to 1.  $k_1$  and  $k_2$  represent rates of phagocytosis and lysosomal degradation, respectively.  $k_c$  is a constant relating the blood Doppler signal to the

liver nonlinear signal. Input data were all distinct combinations of Doppler and AM time courses from each biological condition. Output values are tabulated in **Table 4-S1**.

### **Statistical analysis**

Sample sizes were chosen based on preliminary experiments to yield sufficient power for the proposed comparisons. Statistical methods are described in applicable figure captions.

### 3.6 Supplementary Information

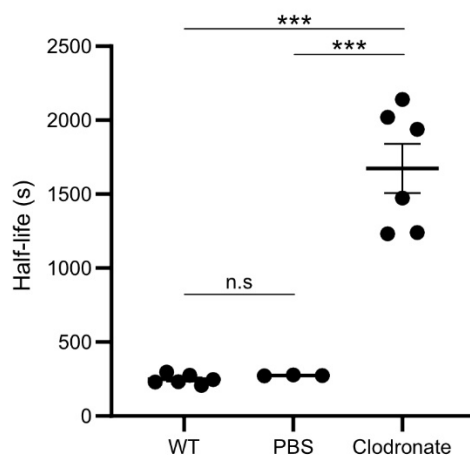


**Figure 3-S1:** Circulation half-life of GVs, as measured by Doppler signal enhancement. Half-life was calculated as the time required for normalized signal enhancement to decline from its maximum at 1 to 0.5. Error bars represent  $\pm$  SEM. N=6 (WT), 3 (PBS liposomes), 6 (clodronate liposomes). Welch's t-test (\*\*\*: $p < 0.001$ ; n.s.:  $p > 0.05$ ).

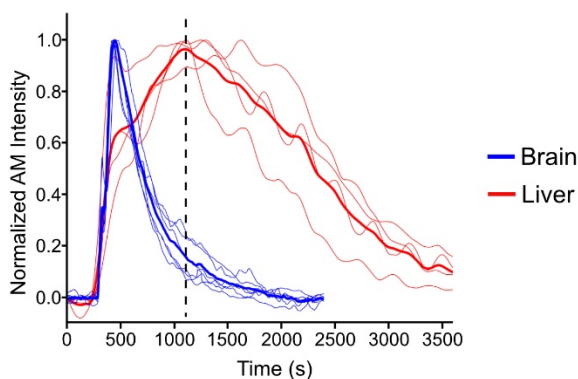


**Figure 3-S2:** Time courses of ultrasound contrast in the brain (blue,  $n = 6$ ) and liver (red,  $n = 4$ ) of healthy C57BL/6 mice. Ultrasound contrast is essentially transferred from the brain to the liver, with liver contrast reaching its maximum (dashed line) after brain contrast dissipates. Thin lines, individual trials; thick lines, mean.

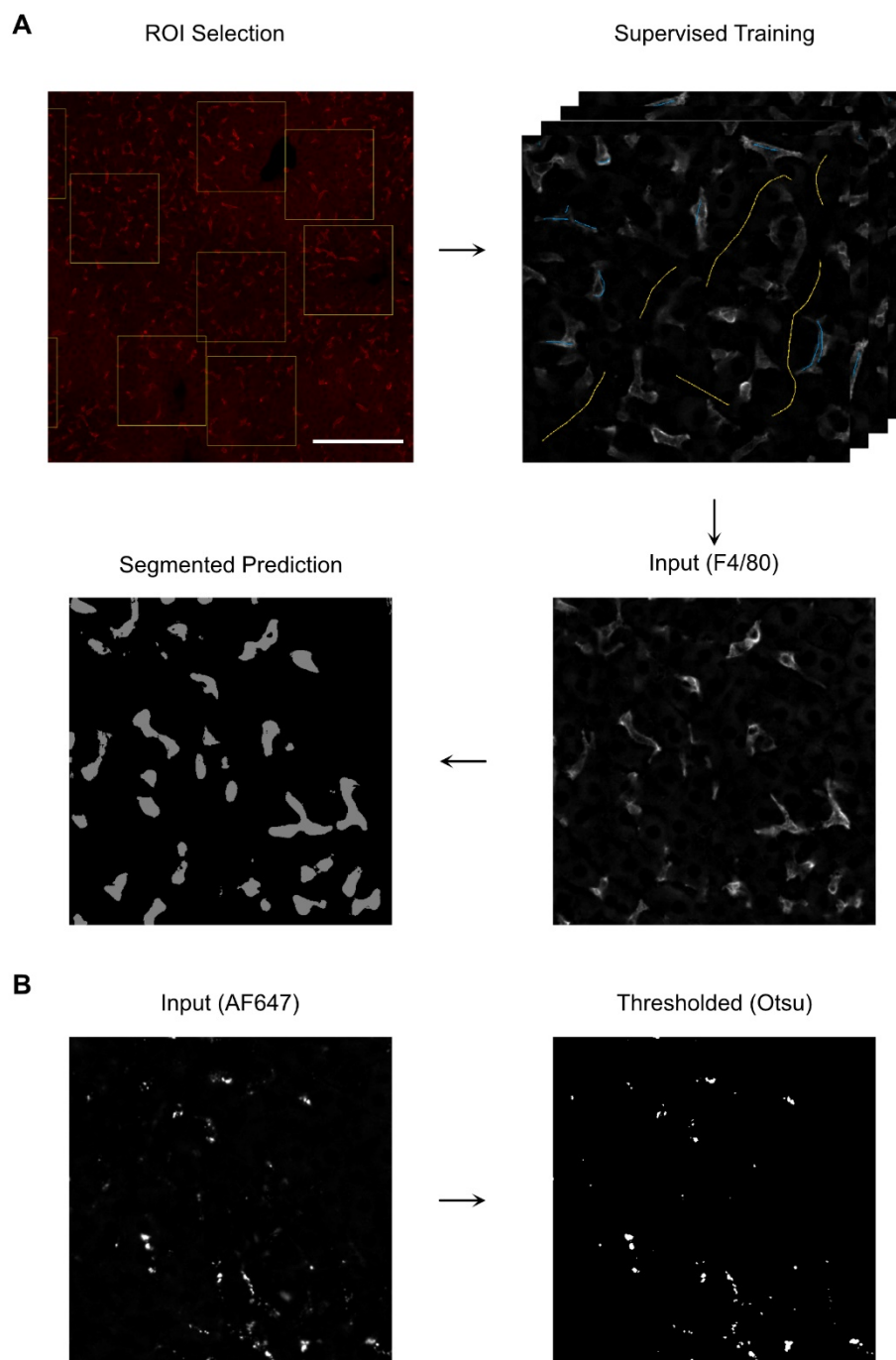


**Figure 3-S3:** Segmentation protocol. **A)** Non-overlapping 500 px x 500 px (approx. 200  $\mu$ m) ROIs were extracted from confocal micrographs of liver slices stained with anti-F4/80 (acquired with 20x objective, scale bar: 200  $\mu$ m). We trained our Pixel Classification algorithm in ilastik by labeling background and macrophage regions on a subset of our images. Then, we segmented the remaining images by processing with the trained network. **B)** The corresponding images in the

AF647 (GV) channel were automatically thresholded by Otsu's method, and colocalization was assessed in MATLAB.

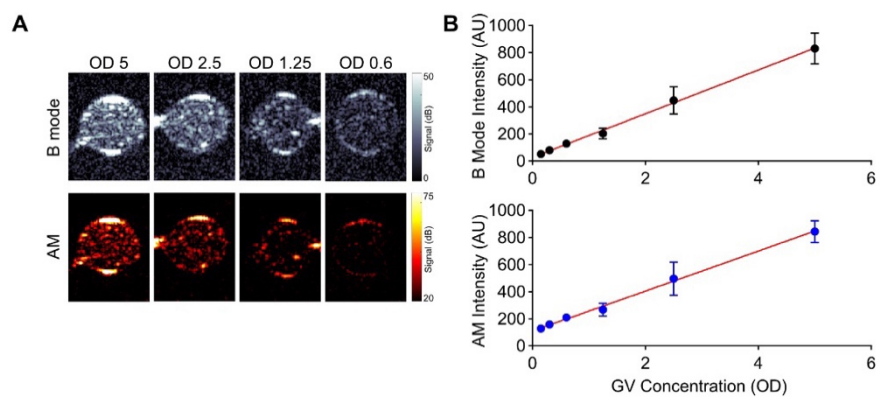


**Figure 3-S4:** Ultrasound contrast is linear with respect to GV concentration. **A)** Representative B mode and AM images of non-linear GVs embedded in 1% agarose. Wells are approx. 2 mm in diameter. **B)** B mode (top) and AM (bottom) signal intensities.  $N = 12$ .

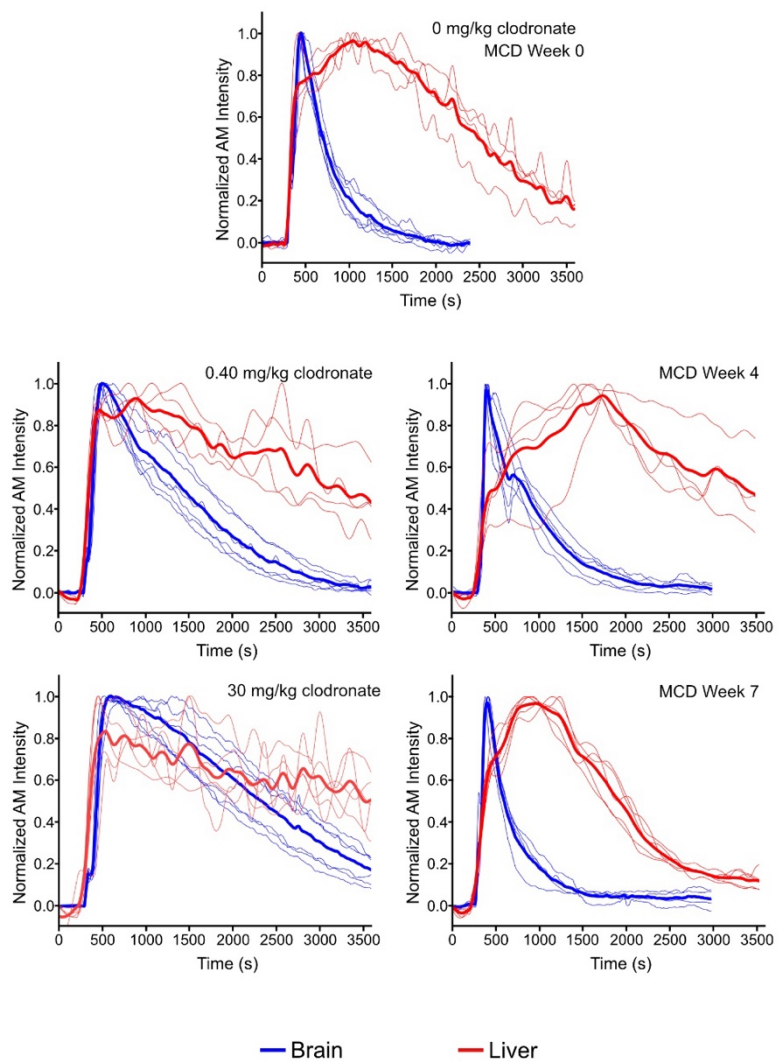


**Figure 3-S5:** Ultrasound signal time courses used for estimating pharmacokinetic parameters. Brain, blue lines; liver, red lines; thin lines, individual trials; thick lines, mean.

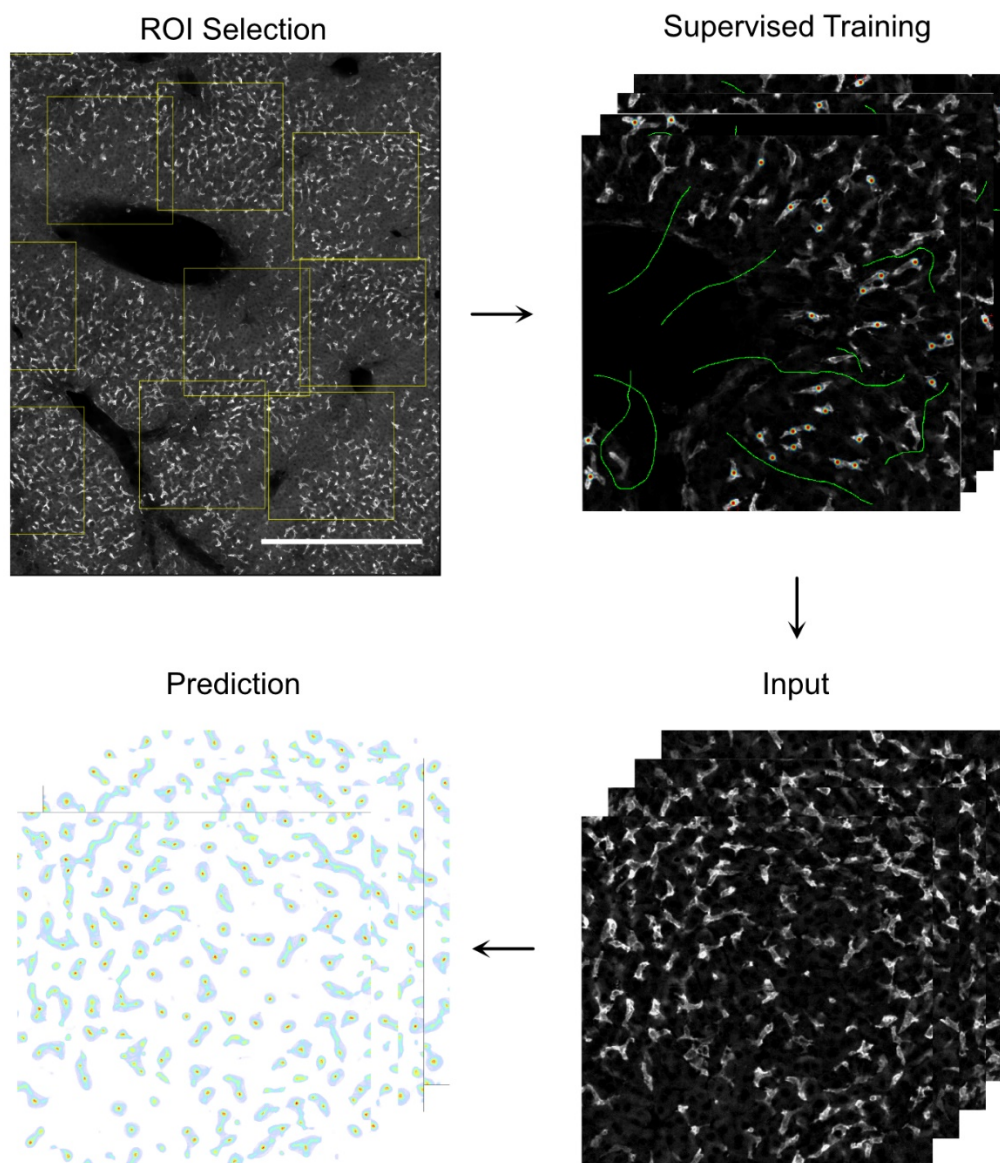


**Figure 3-S6:** Processing for macrophage counting. Non-overlapping 500 px x 500 px (approx. 400  $\mu\text{m}$ ) ROIs were extracted from confocal micrographs of liver slices stained with anti-F4/80 (acquired with 10x objective, scale bar: 500  $\mu\text{m}$ ). Using the Density Counting workflow in ilastik, we annotated a subset of these images for background and cell bodies. Then, we processed the remaining images with our trained algorithm to predict macrophage density.

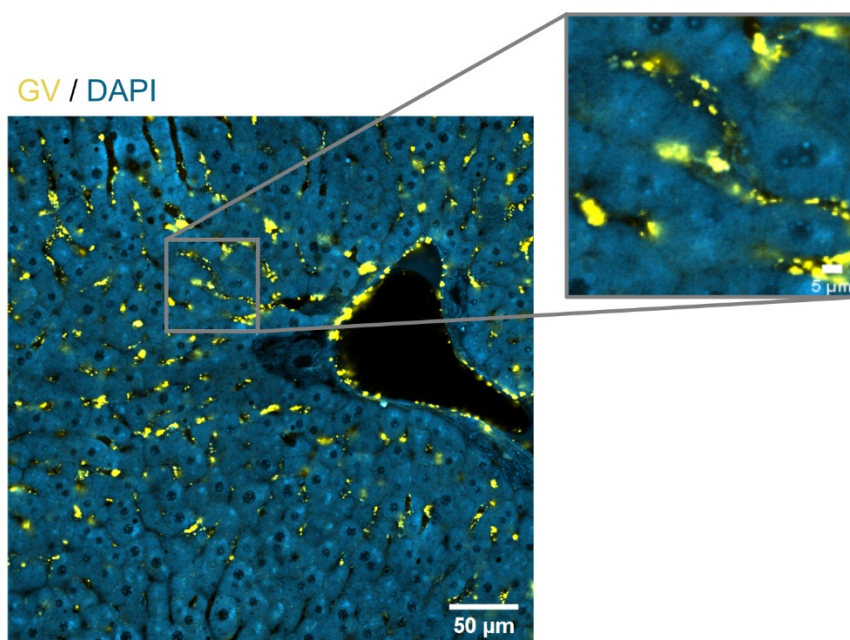


**Figure 3-S7:** Confocal microscopy image of a liver section from a mouse treated with 30 mg/kg clodronate demonstrating localization of GVs to the sinusoidal periphery. Scale bars: 50  $\mu\text{m}$ . Inset: 5  $\mu\text{m}$ .

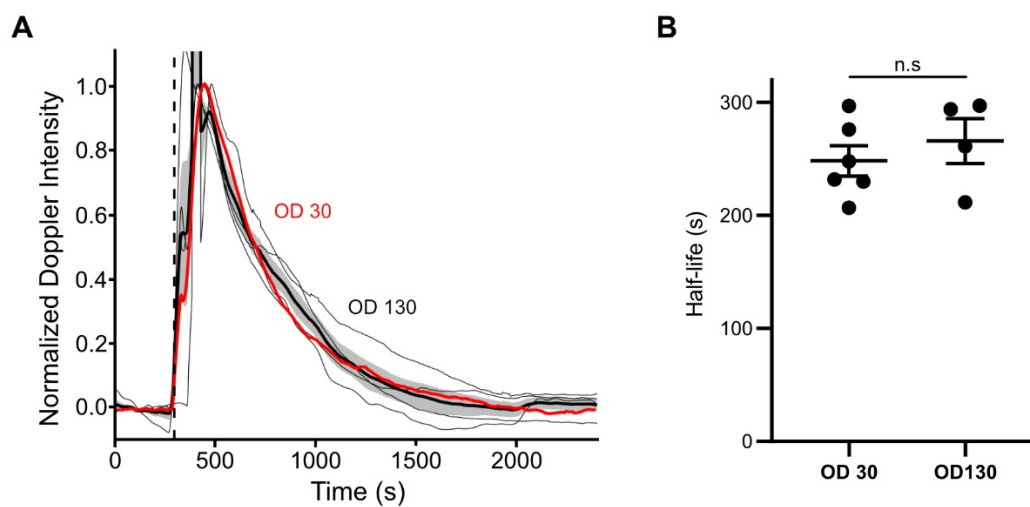


**Figure 3-S8:** Hepatic clearance does not saturate under experimental conditions. **A)** Time course of ultrafast Doppler signal enhancement following IV injection of purified GV<sub>s</sub> at 300 s (dashed line). Individual traces, shown as thin lines, were normalized to their respective maxima. The thick line represents the mean of N = 4 biological replicates. Shaded area represents  $\pm$  SEM. **B)** Half-lives of signal enhancement following IV injection of 100  $\mu$ L GV<sub>s</sub> at OD30 or OD130. Welch's t-test(n.s:  $p > 0.05$ ).

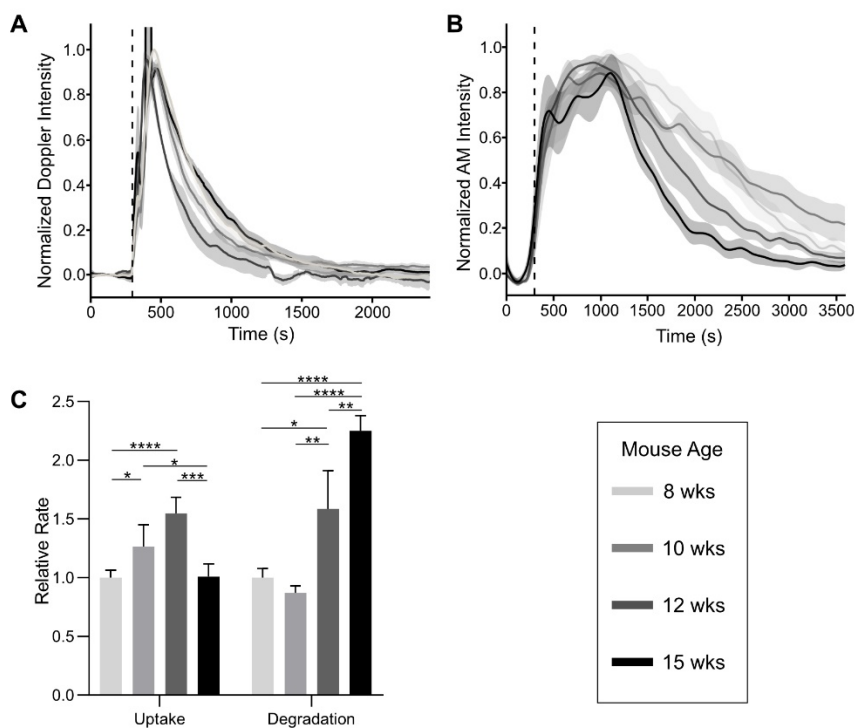


**Figure 3-S9:** Hepatic macrophage activity changes with age. **A)** Time course of Doppler signal enhancement in mice of different ages following GV injection. Shaded areas represent  $\pm$  SEM. N = 4-6 **B)** Time course of liver AM signal. Shaded areas represent  $\pm$  SEM. N=3-5 **C)** Rates of GV uptake and degradation relative to those of 8 week old mice. Error bars represent  $\pm$  SD. N=3-5. Welch's t-test(\*: $p < 0.05$ ; \*\*: $p < 0.01$ ).

Condition	Uptake Rate ( $\text{min}^{-1}$ , $\pm$ SD)	Degradation Rate ( $\text{min}^{-1}$ , $\pm$ SD)	$k_c$ ( $\pm$ SD)
0 mg/kg clodronate	$0.1667 \pm 0.0107$	$0.0407 \pm 0.0032$	$0.7572 \pm 0.2328$
0.40 mg/kg clodronate	$0.0574 \pm 0.0045$	$0.0299 \pm 0.0053$	$0.6073 \pm 0.2587$
30 mg/kg clodronate	$0.0299 \pm 0.0010$	$0.0175 \pm 0.0012$	$0.3843 \pm 0.4507$
MCD: 0 weeks	$0.1667 \pm 0.0107$	$0.0407 \pm 0.0032$	$0.7572 \pm 0.2328$
MCD: 4 weeks	$0.1087 \pm 0.0108$	$0.0172 \pm 0.0019$	$0.7268 \pm 0.2899$
MCD: 7 weeks	$0.1818 \pm 0.0068$	$0.0612 \pm 0.0017$	$1.0000 \pm 0.0000$
Age: 8 weeks	$0.1667 \pm 0.0107$	$0.0407 \pm 0.0032$	$0.7572 \pm 0.2328$
Age: 10 weeks	$0.2108 \pm 0.0310$	$0.0354 \pm 0.0025$	$0.6478 \pm 0.0859$
Age: 12 weeks	$0.2577 \pm 0.0229$	$0.0645 \pm 0.0132$	$0.9576 \pm 0.0752$
Age: 15 weeks	$0.1681 \pm 0.0181$	$0.0916 \pm 0.0052$	$0.8879 \pm 0.1546$

**Table 3-S1:** Constants derived from fitting pharmacokinetic model to ultrasound data.  $k_1$ , uptake rate;  $k_2$ , degradation rate;  $k_c$ , conversion constant.

## References

1. Tavares, A. J.; Poon, W.; Zhang, Y.-N.; Dai, Q.; Besla, R.; Ding, D.; Ouyang, B.; Li, A.; Chen, J.; Zheng, G.; Robbins, C.; Chan, W. C. W., Effect of Removing Kupffer Cells on Nanoparticle Tumor Delivery. *Proc. Natl. Acad. Sci. U. S. A.* **2017**, *114*, E10871-E10880.
2. Berg, R. D.; Levitte, S.; O'Sullivan, M. P.; O'Leary, S. M.; Cambier, C.; Cameron, J.; Takaki, K. K.; Moens, C. B.; Tobin, D. M.; Keane, J.; Ramakrishnan, L., Lysosomal Disorders Drive Susceptibility to Tuberculosis by Compromising Macrophage Migration. *Cell* **2016**, *165*, 139-152.
3. Block, M. L.; Zecca, L.; Hong, J.-S., Microglia-Mediated Neurotoxicity: Uncovering the Molecular Mechanisms. *Nat. Rev. Neurosci.* **2007**, *8*, 57-69.
4. Wang, C.; Yue, H.; Hu, Z.; Shen, Y.; Ma, J.; Li, J.; Wang, X.-D.; Wang, L.; Sun, B.; Shi, P.; Wang, L.; Gu, Y., Microglia Mediate Forgetting *via* Complement-Dependent Synaptic Elimination. *Science* **2020**, *367*, 688-694.
5. Kazankov, K.; Jørgensen, S. M. D.; Thomsen, K. L.; Møller, H. J.; Vilstrup, H.; George, J.; Schuppan, D.; Grønbaek, H., The Role of Macrophages in Nonalcoholic Fatty Liver Disease and Nonalcoholic Steatohepatitis. *Nat. Rev. Gastroenterol. Hepatol.* **2019**, *16*, 145-159.
6. Netea, M. G.; Balkwill, F.; Chonchol, M.; Cominelli, F.; Donath, M. Y.; Giamarellos-Bourboulis, E. J.; Golenbock, D.; Gresnight, M. S.; Heneka, M. T.; Hoffman, H. M.; Hotchkiss, R.; Joosten, L. A. B.; Kastner, D. L.; Korte, M.; Latz, E.; Libby, P.; Mandrup-Poulsen, T.; Mantovani, A.; Mills, K. H. G.; Nowak, K. L., *et al.*, A Guiding Map for Inflammation. *Nat. Immunol.* **2017**, *18*, 826-831.
7. Poon, W.; Zhang, Y.-N.; Ouyang, B.; Kingston, B. R.; Wu, J. L. Y.; Wilhelm, S.; Chan, W. C. W., Elimination Pathways of Nanoparticles. *ACS Nano* **2019**, *13*, 5785-5798.
8. Tsoi, K. M.; MacParland, S. A.; Ma, X.-Z.; Spetzler, V. N.; Echeverri, J.; Ouyang, B.; Fadel, S. M.; Sykes, E. A.; Goldaracena, N.; Kathis, J. M.; Conneely, J. B.; Alman, B. A.; Selzner, M.; Ostrowski, M. A.; Adeyi, O. A.; Zilman, A.; McGilvray, I. D.; Chan, W. C. W., Mechanism of Hard-Nanomaterial Clearance by the Liver. *Nat. Mater.* **2016**, *15*, 1212-1221.
9. Chow, A.; Brown, B. D.; Merad, M., Studying the Mononuclear Phagocyte System in the Molecular Age. *Nat. Rev. Immunol.* **2011**, *11*, 788-798.
10. Blanco, E.; Shen, H.; Ferrari, M., Principles of Nanoparticle Design for Overcoming Biological Barriers to Drug Delivery. *Nat. Biotechnol.* **2015**, *33*, 941-951.
11. Anstee, Q. M.; Reeves, H. L.; Kotsiliti, E.; Govaere, O.; Heikenwalder, M., From NASH to HCC: Current Concepts and Future Challenges. *Nat. Rev. Gastroenterol. Hepatol.* **2019**, *16*, 411-428.
12. Maresca, D.; Lakshmanan, A.; Abedi, M.; Bar-Zion, A.; Farhadi, A.; Lu, G. J.; Szablowski, J. O.; Yoo, S.; Shapiro, M. G., Biomolecular Ultrasound and Sonogenetics. *Annu. Rev. Chem. Biomol. Eng.* **2018**, *9*, 229-252.
13. MacParland, S. A.; Tsoi, K. M.; Ouyang, B.; Ma, X.-Z.; Manuel, J.; Fawaz, A.; Ostrowski, M. A.; Alman, B. A.; Chan, W. C. W.; McGilvray, I. D., Phenotype Determines Nanoparticle Uptake by Human Macrophages from Liver and Blood. *ACS Nano* **2017**, *11*, 2428-2443.

14. Russell, D. G.; VanderVen, B. C.; Glennie, S.; Mwandumba, H.; Heyderman, R. S., The Macrophage Marches on its Phagosome: Dynamic Assays of Phagosome Function. *Nat. Rev. Immunol.* **2009**, *9*, 594-600.
15. Canton, J.; Khezri, R.; Glogauer, M.; Grinstein, S., Contrasting Phagosome pH Regulation and Maturation in Human M1 and M2 Macrophages. *Mol. Biol. Cell* **2014**, *25*, 3330-3341.
16. Iijima, H.; Moriyasu, F.; Tsuchiya, K.; Suzuki, S.; Yoshida, M.; Shimizu, M.; Sasaki, S.; Nishiguchi, S.; Maeyama, S., Decrease in Accumulation of Ultrasound Contrast Microbubbles in Non-Alcoholic Steatohepatitis. *Hepatol. Res.* **2007**, *37*, 722-730.
17. Yoshikawa, S.; Iijima, H.; Saito, M.; Tanaka, H.; Imanishi, H.; Yoshimoto, N.; Yoshimoto, T.; Futatsugi-Yumikura, S.; Nakanishi, K.; Tsujimura, T.; Nishigama, T.; Kudo, A.; Arii, S.; Nishiguchi, S., Crucial Role of Impaired Kupffer Cell Phagocytosis on the Decreased Sonazoid-Enhanced Echogenicity in a Liver of a Nonalcoholic Steatohepatitis Rat Model. *Hepatol. Res.* **2010**, *40*, 823-831.
18. Walsby, A. E., Gas Vesicles. *Microbiol. Rev.* **1994**, *58*, 94-144.
19. Shapiro, M. G.; Goodwill, P. W.; Neogy, A.; Yin, M.; Foster, F. S.; Schaffer, D. V.; Conolly, S. M., Biogenic Gas Nanostructures as Ultrasonic Molecular Reporters. *Nat. Nanotechnol.* **2014**, *9*, 311-316.
20. Lakshmanan, A.; Lu, G. J.; Farhadi, A.; Nety, S. P.; Kunth, M.; Lee-Gosselin, A.; Maresca, D.; Bourdeau, R. W.; Yin, M.; Yan, J.; Witte, C.; Malounda, D.; Foster, F. S.; Schröder, L.; Shapiro, M. G., Preparation of Biogenic Gas Vesicle Nanostructures for Use as Contrast Agents for Ultrasound and MRI. *Nat. Protoc.* **2017**, *12*, 2050-2080.
21. Bourdeau, R. W.; Lee-Gosselin, A.; Lakshmanan, A.; Farhadi, A.; Ravindra Kumar, S.; Nety, S. P.; Shapiro, M. G., Acoustic Reporter Genes for Noninvasive Imaging of Microorganisms in Mammalian Hosts. *Nature* **2018**, *553*, 86-90.
22. Farhadi, A.; Ho, G. H.; Kunth, M.; Ling, B.; Lakshmanan, A.; Lu, G. J.; Bourdeau, R. W.; Schröder, L.; Shapiro, M. G., Recombinantly Expressed Gas Vesicles as Nanoscale Contrast Agents for Ultrasound and Hyperpolarized MRI. *AIChE J.* **2018**, *64*, 2927-2933.
23. Farhadi, A.; Ho, G. H.; Sawyer, D. P.; Bourdeau, R. W.; Shapiro, M. G., Ultrasound Imaging of Gene Expression in Mammalian Cells. *Science* **2019**, *365*, 1469-1475.
24. Maresca, D.; Lakshmanan, A.; Lee-Gosselin, A.; Melis, J. M.; Ni, Y.-L.; Bourdeau, R. W.; Kochmann, D. M.; Shapiro, M. G., Nonlinear Ultrasound Imaging of Nanoscale Acoustic Biomolecules. *Appl. Phys. Lett.* **2017**, *110*, 073704.
25. Maresca, D.; Payen, T.; Lee-Gosselin, A.; Ling, B.; Malounda, D.; Demene, C.; Tanter, M.; Shapiro, M. G., Acoustic Biomolecules Enhance Hemodynamic Functional Ultrasound Imaging of Neural Activity. *NeuroImage* **2020**, *209*, 116467.
26. Maresca, D.; Sawyer, D. P.; Renaud, G.; Lee-Gosselin, A.; Shapiro, M. G., Nonlinear X-Wave Ultrasound Imaging of Acoustic Biomolecules. *Phys. Rev. X* **2018**, *8*, 041002.
27. Lakshmanan, A.; Farhadi, A.; Nety, S. P.; Lee-Gosselin, A.; Bourdeau, R. W.; Maresca, D.; Shapiro, M. G., Molecular Engineering of Acoustic Protein Nanostructures. *ACS Nano* **2016**, *10*, 7314-7322.
28. Santiesteban, D. Y.; Hallam, K. A.; Yarmoska, S. K.; Emelianov, S. Y., Color-Coded Perfluorocarbon Nanodroplets for Multiplexed Ultrasound and Photoacoustic Imaging. *Nano Res.* **2019**, *12*, 741-747.

29. Sheeran, P. S.; Dayton, P. A., Phase-Change Contrast Agents for Imaging and Therapy. *Curr. Pharm. Des.* **2012**, *18*, 2152-2165.
30. Ferrara, K.; Pollard, R.; Borden, M., Ultrasound Microbubble Contrast Agents: Fundamentals and Application to Gene and Drug Delivery. *Annu. Rev. Biomed. Eng.* **2007**, *9*, 415-447.
31. Cox, D. J.; Thomas, J. L., Ultrasound-Induced Dissolution of Lipid-Coated and Uncoated Gas Bubbles. *Langmuir* **2010**, *26*, 14774-14781.
32. Le Floc'h, J.; Zlitni, A.; Bilton, H. A.; Yin, M.; Farhadi, A.; Janzen, N. R.; Shapiro, M. G.; Valliant, J. F.; Foster, F. S., *In Vivo* Biodistribution of Radiolabeled Acoustic Protein Nanostructures. *Mol. Imaging Biol.* **2018**, *20*, 230-239.
33. Yan, J.; Yin, M.; Foster, F. S.; Démoré, C. E. M., Tumor Contrast Imaging with Gas Vesicles by Circumventing the Reticuloendothelial System. *Ultrasound Med. Biol.* **2020**, *46*, 359-368.
34. Cheong, H.; Lee, S. S.; Lee, J. S.; Kim, J.; Kim, S. W.; Lee, W. J., Phagocytic Function of Kupffer Cells in Mouse Nonalcoholic Fatty Liver Disease Models: Evaluation with Superparamagnetic Iron Oxide. *J. Magn. Reson. Imaging* **2014**, *41*, 1218-1227.
35. Smits, L.; Coolen, B.; Panno, M.; Runge, J.; Nijhof, W.; Verheij, J.; Nieudorp, M.; Stoker, J.; Beuers, U.; Nederveen, A.; Stroes, E., Noninvasive Differentiation between Hepatic Steatosis and Steatohepatitis with MR Imaging Enhanced with USPIOs in Patients with Nonalcoholic Fatty Liver Disease: A Proof-Of-Concept Study. *Radiology* **2016**, *278*, 782-791.
36. Miyata, Y.; Miyahara, T.; Moriyasu, F., Decreased Accumulation of Ultrasound Contrast in the Liver of Nonalcoholic Steatohepatitis Rat Model. *World J. Gastroenterol.* **2011**, *17*, 4191-4198.
37. Macé, E.; Montaldo, G.; Cohen, I.; Baulac, M.; Fink, M.; Tanter, M., Functional Ultrasound Imaging of the Brain. *Nat. Methods* **2011**, *8*, 662-664.
38. Oh, Y.-K.; Swanson, J. A., Different Fates of Phagocytosed Particles After Delivery Into Macrophage Lysosomes. *J. Cell Biol.* **1996**, *132*, 585-593.
39. Davidson, S. J., Proteolytic Activity Within Lysosomes and Turnover of Pinocytic Vesicles. A Kinetic Analysis. *Biochim. Biophys. Acta, Gen. Subj.* **1975**, *411*, 282-290.
40. Harashima, H.; Hirai, N.; Kiwada, H., Kinetic Modelling of Liposome Degradation in Peritoneal Macrophages. *Biopharm. Drug Dispos.* **1995**, *16*, 113-123.
41. Berg, S.; Kutra, D.; Kroeger, T.; Straehle, C. N.; Kausler, B. X.; Haubold, C.; Schiegg, M.; Ales, J.; Beier, T.; Rudy, M.; Eren, K.; Cervantes, J. I.; Xu, B.; Beuttenmueller, F.; Wolny, A.; Zhang, C.; Koethe, U.; Hamprecht, F. A.; Kreshuk, A., Ilastik: Interactive Machine Learning for (Bio)image Analysis. *Nat. Methods* **2019**, *16*, 1226-1232.
42. van Rooijen, N.; Hendrikx, E., Liposomes for Specific Depletion of Macrophages from Organs and Tissues. *Methods Mol. Biol.* **2010**, *605*, 189-203.
43. Kinchen, J. M.; Ravichandran, K. S., Phagosome Maturation: Going through the Acid Test. *Nat. Rev. Mol. Cell Biol.* **2008**, *9*, 781-795.
44. Yoshimori, T.; Yamamoto, A.; Moriyama, Y.; Futai, M.; Tashiro, Y., Bafilomycin A1, a Specific Inhibitor of Vacuolar-Type H<sup>+</sup>-ATPase, Inhibits Acidification and Protein Degradation in Lysosomes of Cultured Cells. *J. Biol. Chem.* **1991**, *266*, 17707-17712.
45. Guo, M.; Hartlova, A.; Dill, B. D.; Prescott, A. R.; Gierlinski, M.; Trost, M., High-Resolution Quantitative Proteome Analysis Reveals Substantial Differences between

- Phagosomes of RAW264.7 and Bone Marrow Derived Macrophages. *Proteomics* **2015**, *15*, 3169-3174.
46. Kassel, K. M.; Guo, G. L.; Tawfik, O.; Luyendyk, J. P., Monocyte Chemoattractant Protein-1 Deficiency Does Not Affect Steatosis or Inflammation in Livers of Mice Fed a Methionine-Choline-Deficient Diet. *Lab. Invest.* **2010**, *90*, 1794-1804.
  47. Asanuma, T.; Ono, M.; Kubota, K.; Hirose, A.; Hayashi, Y.; Saibara, T.; Inanami, O.; Ogawa, Y.; Enzan, H.; Onishi, S.; Kuwabara, M.; Oben, J. A., Super Paramagnetic Iron Oxide MRI Shows Defective Kupffer Cell Function in Non-Alcoholic Fatty Liver Disease. *Gut* **2010**, *59*, 258-266.
  48. Heymann, F.; Peusquens, J.; Ludwig-Portugall, I.; Kohlhepp, M.; Ergen, C.; Niemietz, P.; Martin, C.; Van Rooijen, N.; Ochando, J. C.; Randolph, G. K.; Luedde, T.; Ginhoux, F.; Kurts, C.; Trautwein, C.; Tacke, F., Liver Inflammation Abrogates Immunological Tolerance Induced by Kupffer Cells. *Hepatology* **2015**, *62*, 279-291.
  49. Hebbard, L.; George, J., Animal Models of Nonalcoholic Fatty Liver Disease. *Nat. Rev. Gastroenterol. Hepatol.* **2011**, *8*, 35-44.
  50. Itagaki, H.; Shimizu, K.; Morikawa, S.; Ogawa, K.; Ezaki, T., Morphological and Functional Characterization of Non-Alcoholic Fatty Liver Disease Induced by a Methionine-Choline-Deficient Diet in C57BL/6 mice. *Int. J. Clin. Exp. Pathol.* **2013**, *6*, 2683-2696.
  51. Dill, B. D.; Gierlinski, M.; Hartlova, A.; Gonzalez, A. A.; Guo, M.; Clarke, R. G.; Trost, M., Quantitative Proteome Analysis of Temporally Resolved Phagosomes Following Uptake *Via* Key Phagocytic Receptors. *Mol. Cell. Proteomics* **2015**, *14*, 1334-1349.
  52. Abu Lila, A. S.; Kiwada, H.; Ishida, T., The Accelerated Blood Clearance (ABC) Phenomenon: Clinical Challenge and Approaches to Manage. *J. Controlled Release* **2013**, *172*, 38-47.
  53. Lu, G. J.; Chou, L.-d.; Malounda, D.; Patel, A. K.; Welsbie, D. S.; Chao, D. L.; Ramalingam, T.; Shapiro, M. G., Genetically Encodable Contrast Agents for Optical Coherence Tomography. *ACS Nano* **2020**.
  54. Ai, H.-w.; Olenych, S. G.; Wong, P.; Davidson, M. W.; Campbell, R. E., Hue-Shifted Monomeric Variants of *Clavularia* Cyan Fluorescent Protein: Identification of the Molecular Determinants of Color and Applications in Fluorescence Imaging. *BMC Biol.* **2008**, *6*, 13.
  55. Piraner, D. I.; Wu, Y.; Shapiro, M. G., Modular Thermal Control of Protein Dimerization. *ACS Synth. Biol.* **2019**, *8*, 2256-2262.

*Chapter 4***ENGINEERING MONOCYTES AS ULTRASOUND REPORTER CELLS  
FOR CANCER DETECTION**

Lee, J.; Ling, B.; Liu, A.; Criado-Hidalgo, E.; You, M.Y.; Jin, Z.; Shapiro, M. G.

*Manuscript in Preparation*

This chapter is a manuscript in preparation for peer review. My contributions to the work were conceiving the study, performing experiments, analyzing data, and preparing the manuscript together with the other authors.

**4.1 Introduction**

There has been increasing interest in leveraging cells' natural ability to migrate towards areas of disease, respond to local environmental cues, and carry out useful behaviors to diagnose and treat disease.<sup>1</sup> Macrophages, and the circulating monocytes they differentiate from, are an interesting chassis for cellular therapy and diagnostics in cancer as they are actively recruited to tumors and can form up to 50% of a tumor's mass.<sup>2</sup> Depending on their environment and the immune signaling, macrophages play a variety of roles in solid tumors including phagocytosis of cancer cells, extracellular matrix remodeling, and cytokine secretion.<sup>3</sup> Because of their recruitment and potential to mediate tumor destruction, macrophages have become increasingly studied as potential targets for tumor therapies.<sup>4,5</sup> Their active recruitment also supports their use for cancer detection. While other cancer detection tools rely on biomarkers like circulating tumor DNA or systemic delivery of tumor-activated probes, these strategies face obstacles like short circulating half-life of endogenous biomarkers or inefficient delivery of probes to tumor stroma.<sup>6-9</sup> Unlike these strategies,

macrophages are actively recruited to tumors, and they are capable of sensing and amplifying tumor signals. These advantages have been leveraged in previous works to engineer a murine macrophage cell line as a potential cancer diagnostic tool using a bioluminescent reporter gene, but human tumors often develop deep within the body these markers cannot be detected due to scattering and absorption of light by tissue.<sup>10</sup>

To improve the potential for macrophages as reporter cells, a modality capable of imaging tissues at depth is required. Gas vesicles (GVs) are genetically encoded, air-filled nanoproteins capable of producing ultrasound contrast in deep tissue and have been used in mammalian cells to produce non-linear ultrasound contrast, thus distinguishing GV expressing cells from surrounding tissue.<sup>11-13</sup> In this work, we engineer monocytes with the potential to respond to certain environmental cues by producing GVs and functioning as ultrasound reporter cells. We demonstrate a human monocyte cell line's ability to produce ultrasound contrast through GV expression and carry out critical functions like migration and phagocytosis while expressing GV. Furthermore, as GV are genetically encoded, we demonstrate the potential to activate GV production in response to two disease signals: tissue hypoxia and the presence of specific tumor antigen.

## **4.2 Results**

### **4.2.1 Optimization of gas vesicle production in THP-1 monocytes**

Mammalian ARGs have been used to produce both collapse and non-collapse based nonlinear ultrasound signal in a range of cell types. Plasmid delivery for monocyte and macrophage transfection remains a significant challenge, so in this study, we turned to lentiviral transduction methods in order to deliver mARG into THP-1 monocytes. Two

mARG systems were tested: a (3P) system consisting of the major GV structural protein (GvpA), the GV chaperones (GvpNV), and tetracycline-dependent transactivator (rtTA) on three separate plasmids in addition to a condensed 2 plasmid system (2P) where GvpA and rtTA are on the same plasmid (**Fig. 4-1A**). We hypothesized that decreasing the number of plasmids in the system would improve transduction and subsequent transgene expression as the GvpA-RFP and GvpA-minEF1a-rtTA plasmid are similar in size (3114 and 2924 LTR-LTR bp, respectively).

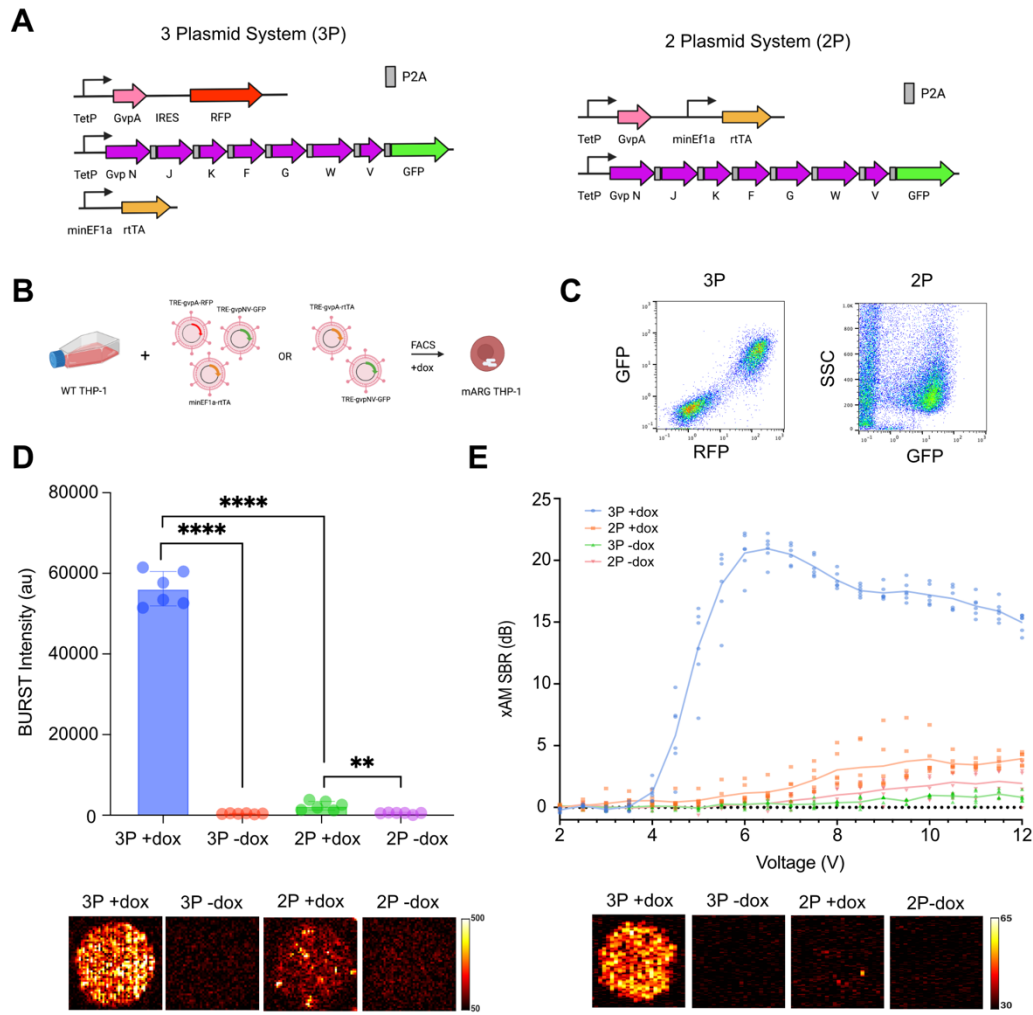


**Fig 4-1:** Testing GV expression in THP-1 cells using two expression systems. **A)** Illustration of the viral constructs being tested which includes a 3 plasmid (3P, left) and 2 plasmid (2P, right) system. **B)** Illustration of the workflow used to transduce THP-1 cells with lentivirus, sort, and induce with doxycycline to produce a GV expressing THP-1 cell line. (Created with BioRender.com and FloJo) **C)** Flow cytometry results measuring RFP and GFP or GFP only to determine successful transduction and activation in the 3P and 2P systems, respectively. **D)** BURST intensity (top) and representative images (bottom) to compare GV contrast produced by the 3P and 2P systems. **E)** xAM SBR quantification (top) and representative images at 6V (bottom) to compare xAM contrast produced by 3P and 2P systems at various voltages. N=6 technical replicates for ultrasound imaging. Where not seen, error bars ( $\pm$ SEM) are smaller than the symbol.

Following lentiviral transduction and sorting of the brightest 0.25% of RFP and GFP positive cells or GFP positive cells for the 3P and 2P system, respectively, and induction with doxycycline (dox) (**Fig. 4-1B, C**), cells were taken for both BURST and xAM imaging, which rely on GV collapse and buckling, to distinguish GV from surrounding tissue.<sup>14,15</sup> The cells yielded both BURST and xAM signal, although the 3P system performed significantly better in THP-1 cells for both imaging modalities (**Fig. 4-1D, E**). To attempt further improvements of 3P system GV production, THP-1 cells were transduced with various stoichiometries of each plasmid (**Fig. 4-S1**). Flow cytometry was used to determine efficiency of transduction. As the rtTA containing plasmid is required for expression of the other two Tet response element (TRE) promoter controlled GV plasmids, cells that are both RFP<sup>+</sup> and GFP<sup>+</sup> were successfully transduced with all three plasmids. Previous studies showed that increasing GvpA ratio improved ultrasound signal.<sup>13</sup> To determine optimal transduction stoichiometry, we evaluated two parameters on flow cytometry: mean fluorescence intensity (MFI) and percentage of triple positive cells. While increasing GvpNV concentration to 1:3:1 GvpA, GvpNV, rtTA resulted in the highest triple positive cells (**Fig. 4-S1**), it also decreased RFP mean fluorescence intensity and lower ultrasound contrast production when compared to that of 1:1:1 GvpA, GvpNV, rtTA (**Fig. 4-S2**). This suggests

higher mean expression of GvpA by RFP MFI is more important than increasing the number of cells containing all three plasmids. We then tested cell viability during GV expression using the Sytox Blue nucleic acid stain and found that cell death reached 9.93% on day one and peaked at 34.03% by day three following dox induction (**Fig. 4-S3**). We also THP-1 GV expression kinetics and found that one day following dox induction resulted in half the maximum expression xAM signal while reaching maximum signal by day 2 and plateaued between days 2-4 (**Fig. 4-S4**).

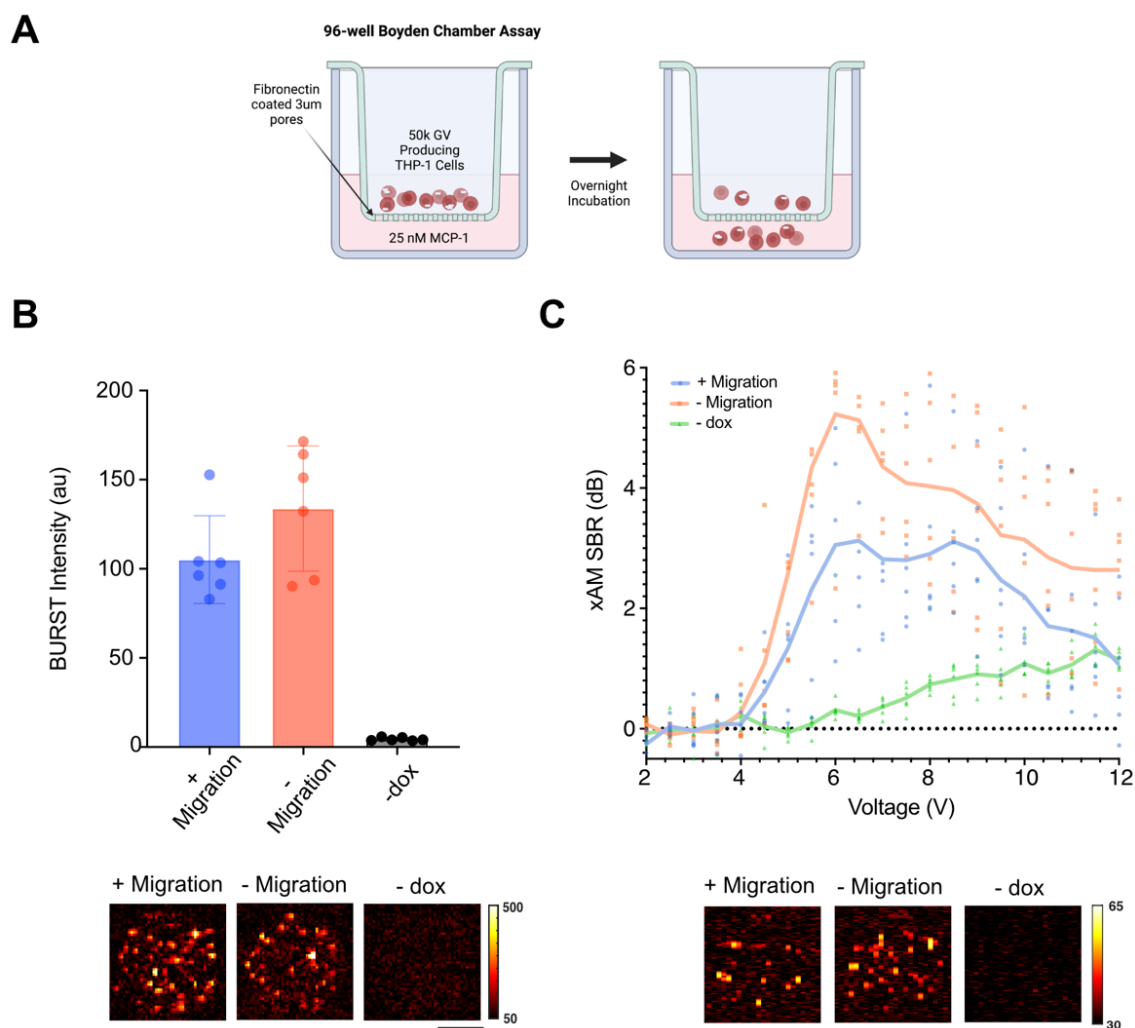


**Fig 4-2:** Determining the potential for GV-containing THP-1 cells to successfully migrate. **A)** Illustration of the transwell experiments where GV containing THP-1 cells migrate through a 3 $\mu$ m pore towards a MCP-1 chemoattractant. (created with BioRender.com) **B)** BURST Intensity quantification (top) comparing cells following migration and unmigrated control cells adjusted to the same cell count (**4-S6**) **C)** xAM SBR quantification at various voltages (top) and representative images at 6V (bottom) comparing THP-1 cells following migration and cell count-adjusted unmigrated controls. N=6 technical replicates for ultrasound imaging. Where not seen, error bars ( $\pm$ SEM) are smaller than the symbol.

#### **4.3.2 Effects of gas vesicle production on THP-1 monocyte and macrophage phenotypes**

Following the development of a GV producing THP-1 cell line, we sought to evaluate the effects of GV production and their intracellular presence on critical functions of monocytes and macrophages. Monocytes form in the bone marrow from pluripotent stem cells after which they enter the blood stream where they travel to areas on inflammation or infection. Upon arrival to tissue they differentiate into macrophages to carry out a range of functions including phagocytosis of foreign materials and debris in addition to secreting immune modulators.<sup>16,17</sup>

To test migration capability, GV containing THP-1 cells were placed in the top well transwell migration assay where the bottom well contained MCP-1, a monocyte chemoattractant. 3  $\mu$ m pores separated the two chambers and after an overnight incubation, 4% of the plated cells migrated through these pores into the bottom wells (**Fig. 4-2A**). This represented ~200k total cells (**Fig. 4-S1**). These post-migration cells and 200k cells that did not undergo migration were taken for ultrasound imaging. Both cell populations demonstrated BURST and xAM contrast (**Fig. 4-2B, C**). The unmigrated cells showed higher average BURST and xAM signal, suggesting there may be some selection against GV containing cells in the migration process, but this decrease was not statistically significant.

After migration, monocytes differentiate into macrophages to carry out effector functions like phagocytosis of cell debris and remodeling of ECM. To determine the effects of differentiation on GV production, we used phorbol 12-myristate 13-acetate (PMA) to differentiate GV-producing THP-1 monocytes into macrophages. PMA-stimulated THP-1 cells become adherent and begin to express CD11 and CD14, and this differentiation protocol has been widely used to model macrophage phenotypes *in vitro*.<sup>18</sup> Following PMA-stimulation, adherent THP-1 macrophages were allowed a rest period of 2 days in culture media and then induced with dox for 4 days. Induced macrophage THP-1 cells were capable of producing GV clusters visible under light microscopy like undifferentiated THP-1 monocytes (**Fig. 4-3A, S5**). Differentiation did not change BURST signal between PMA differentiated cells and DMSO control cells. On xAM imaging however, there was a modest but statistically significant decrease in signal between PMA and DMSO treated cells at 6V ( $16.01 \pm 1.897$  and  $19.59 \pm 1.8$ ). Overall, these results confirm that differentiated THP-1 macrophages are still capable of producing both BURST and xAM ultrasound signal.

After confirming the ability for monocytes to migrate while containing intracellular GV and the capability for THP-1 cells to produce GVs following differentiation into a macrophage phenotype, we next sought to test GV-containing macrophages to successfully perform phagocytosis. We co-incubated  $2\mu\text{m}$  BFP<sup>+</sup> polystyrene beads with differentiated macrophages after induction and production of GV. After a one-day incubation, the cells were fixed and taken for confocal imaging. We located cells containing visible GV clusters on brightfield and the used fluorescence imaging of GV-containing cells to develop 3D renderings. BFP<sup>+</sup> polystyrene beads were found at various heights within the cell and their distance to the nearest cell membrane was calculated in the representative cell shown (**Fig.**

**4-3D, S6).** Taken in conjunction, these experiments suggest that critical cellular functions like migration and phagocytosis are possible by cells containing intracellular GV, and that GV production is robust to differentiation.

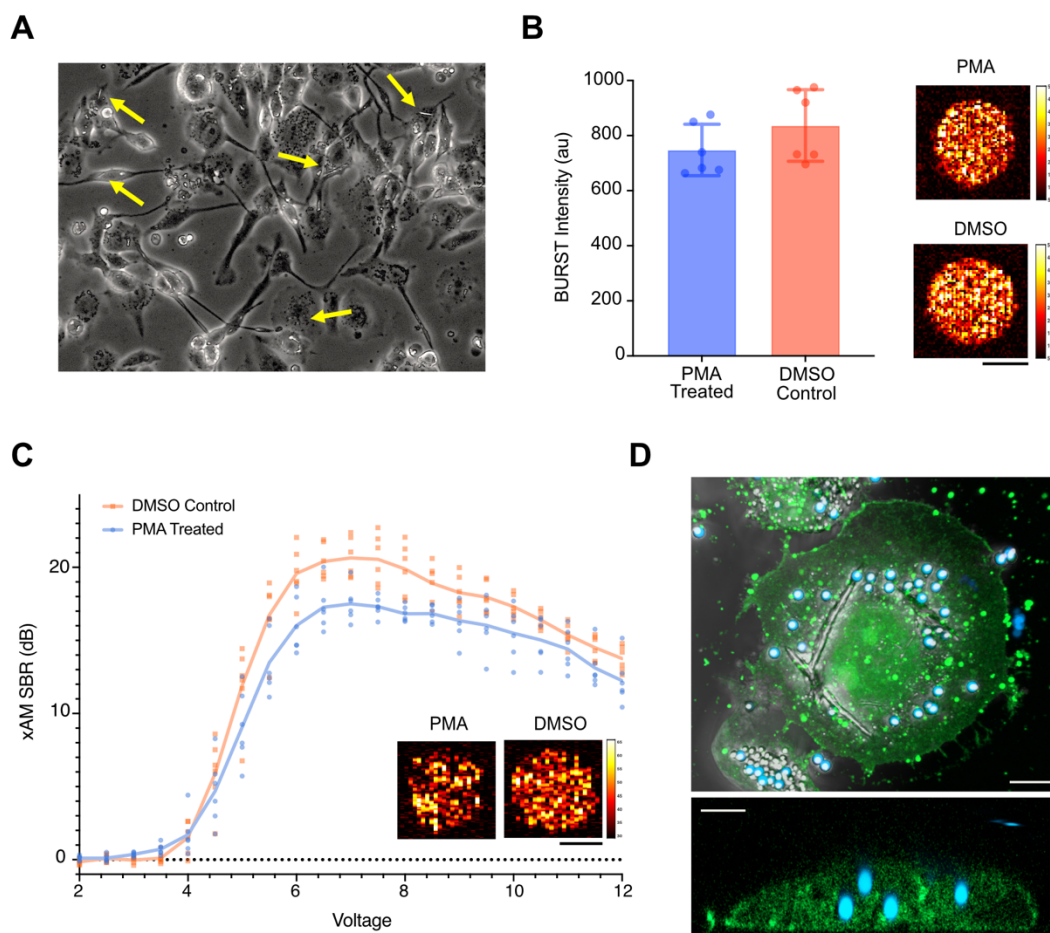


**Fig 4-3:** Determining the effects of differentiation into a macrophage-like phenotype on GV production and the potential for GV containing THP-1 macrophages to complete phagocytosis. **A)** Microscopy image demonstrating GV cluster formation (yellow arrows) following differentiation with PMA. **B)** BURST ultrasound contrast intensity quantification (left) and representative BURST images (right) comparing the contrast produced by THP-1 cells following differentiation with DMSO treated control cells. **C)** xAM SBR quantification at various voltages following differentiation with THP-1 treated with PMA or with DMSO, including representative xAM images of both samples at 6V. N=6 technical replicates for ultrasound imaging. Where not seen, error bars ( $\pm$ SEM) are smaller than the symbol. Ultrasound scale bar: 1mm. **D)** Confocal imaging following GV expression by THP-1 macrophages and incubation with 2µm BFP polystyrene beads showing a GV containing cell (above) and a cross section (below) demonstrating presence of 2µm beads within the cell cytoplasm (green due to the GFP produced during GV expression). Confocal scale bar: 3µm.

### 4.3.3 Hypoxia Induced Gas Vesicle Expression

After confirming robust GV expression and maintenance of both monocyte and macrophage function in GV-expressing THP-1 cells, we sought to connect GV expression to specific stimuli associated with disease states. A common feature in cancers is tumor hypoxia. As tumor cells proliferate uncontrollably, oxygen demand outpaces supply, and as vasculature growth becomes increasingly dysregulated, oxygen levels decrease within solid tumors. Median percent O<sub>2</sub> levels range from 1-2% with tumor cores, often reaching closer to anoxic levels.<sup>19</sup> Physoxia, on the other hand, ranges between 5%-10% depending on the organ and tissue type and atmospheric O<sub>2</sub> is roughly 21%. In mammals, sufficient O<sub>2</sub> is required for aerobic cellular respiration, and in response to low oxygen stress, mammalian cells rely on hypoxia-inducible factors (HIFs) that activate transcription of genes like vascular endothelial growth factor (VEGF) and erythropoietin.<sup>20</sup> This transcriptional response has been leveraged to create synthetic hypoxia responsive elements (HREs) by taking promoter sequences upstream of genes induced in hypoxia. These HREs activate transgenes specifically in the presence of hypoxia.<sup>21,22</sup>

To develop hypoxia induced gas vesicle expression, we used a promoter sequence comprised of five repeats of the VEGF HRE sequence and minimal human cytomegalovirus upstream of the rtTA protein in addition to the GvpA and GvpNV plasmids used previously.<sup>23</sup> In this system, hypoxic conditions initiate production of rtTA, and in the presence of dox, rtTA begins GV expression. Two versions of the HRE rtTA plasmid were produced shown in **Fig. 4A** to test the impact of increasing rtTA production while decreasing transduction efficiency as plasmid size increases.

Before testing hypoxia induced GV expression, we sought to determine the effects of hypoxia on GV production. We used the 3P system that was previously optimized and incubated cells with dox in either 20% O<sub>2</sub> as done in previous experiments or 1% O<sub>2</sub> to represent hypoxic growth conditions. These cells were then taken for BURST and xAM imaging, which both demonstrated no significant difference between cells grown in atmospheric O<sub>2</sub> or hypoxic conditions (**Fig. 4-S7**). This suggests that culture in low oxygen does not in itself hinder GV production.

We then tested both systems, HRE1x and HRIR, and their potential to enable hypoxia-induced GV production. As this system requires an initial step of rtTA production before GV expression can begin, we induced these cells for one week with dox. Additionally, while the previously used 20% O<sub>2</sub> incubator setting represents atmospheric O<sub>2</sub>, tissue normoxia is lower. To test relevant physiologic O<sub>2</sub> pressures, we also incubated the cells containing the HRE circuit at 7.5% O<sub>2</sub> to determine any potential leaky expression in normoxic conditions. We compared both 1% and 7.5% O<sub>2</sub> incubations with a 20% O<sub>2</sub> condition, since we have only one O<sub>2</sub>-controlled incubator. Both HRE1x and HRIR circuits showed contrast on BURST only at 1% O<sub>2</sub> after seven days of dox induction (13.5-fold and 30.8-fold increase in BURST intensity when compared to 7.5% O<sub>2</sub>, respectively) (**Fig. 4-4B**). On xAM imaging, HRE1x and HRIR circuits demonstrated increased xAM SBR contrast at 1% O<sub>2</sub> (17.3-fold and 8.2-fold increase in SBR at 6V when compared to 7.5% O<sub>2</sub>, respectively) (**Fig. 4-4C**). These results suggest that transcriptional controls leveraging synthetic HRE promoters can enable distinguishing a hypoxic 1% O<sub>2</sub> environment and normoxic 7.5% O<sub>2</sub> environment.

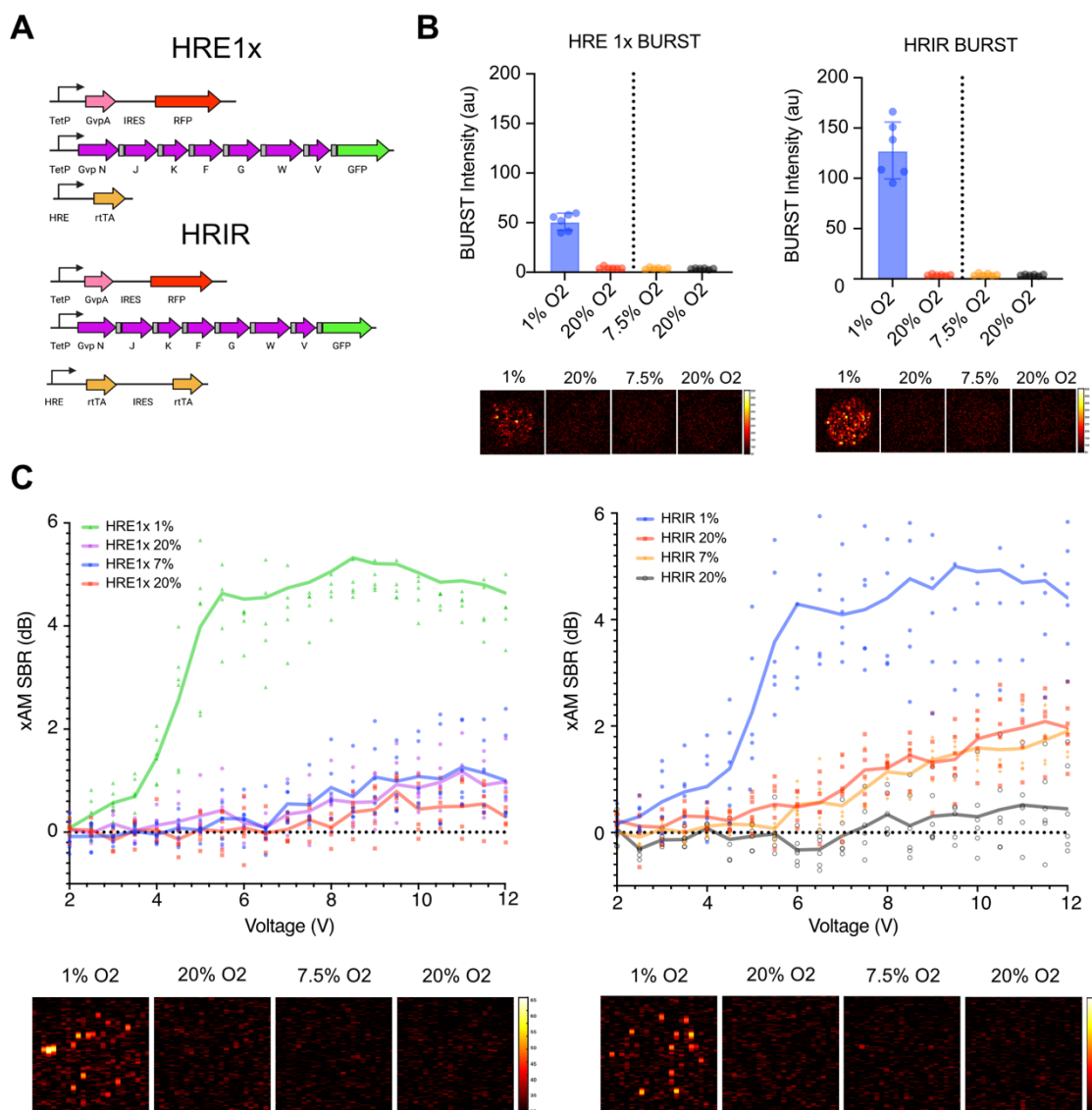


**Fig 4-4:** Developing hypoxia-inducible GV expression in THP-1 cells **A)** Illustration of the viral constructs being tested which includes a HRE1x and HRIR transactivator plasmid. **B)** BURST intensity quantification (top) comparing the ultrasound contrast produced by HRE1x and HRIR THP-1 with representative images (bottom) of cells following sorting and induction with doxycycline and 1% and 7.5% O<sub>2</sub> incubator for seven days. Both 1% and 7.5% O<sub>2</sub> conditions were controlled by induction with doxycycline at atmospheric (20%) O<sub>2</sub>. **C)** xAM SBR quantification following induction parameters the parameters above to compare the xAM contrast produced by HRE1x and HRIR transduced THP-1 cells at various voltages with representative images (below). N=6 technical replicates for ultrasound imaging. Where not seen, error bars ( $\pm$ SEM) are smaller than the symbol. Scale bar: 1mm.

To develop hypoxia induced gas vesicle expression, we used a promoter sequence comprised of five repeats of the VEGF HRE sequence and minimal human cytomegalovirus upstream of the rtTA protein in addition to the GVpA and GV chaperone plasmids used previously.<sup>24</sup> In this system, hypoxic conditions initiate production of rtTA, and in the presence of doxycycline, rtTA begins GV expression. Two versions of the HRE rtTA plasmid were produced, shown in **Fig. 4A**, to test the impact of increasing rtTA production while decreasing transduction efficiency as plasmid size increases.

However, before testing hypoxia induced GV expression, we sought to determine the effects of hypoxia on GV production. We used the 3P system that was previously optimized, and we incubated these cells with doxycycline in either 20% O<sub>2</sub> as done in previous experiment or 1% O<sub>2</sub> to represent hypoxic growth conditions. These cells were then taken for BURST and xAM imaging which both demonstrated no significant difference between cells grown in atmospheric O<sub>2</sub> or hypoxic conditions (**Fig. 4-S7**). This suggests that culture in low oxygen does not in itself hinder GV production.

We then tested both systems, HRE1x and HRIR and their potential to enable hypoxia induced GV production. As this system requires an initial step of rtTA production before GV expression can begin, we incubated these cells for one week with doxycycline. Additionally, while the previously used 20% O<sub>2</sub> incubator setting represents atmospheric O<sub>2</sub>, tissue normoxia is lower. To test relevant physiologic O<sub>2</sub> pressures, we also incubated the cells containing the HRE circuit at 7.5% O<sub>2</sub> to determine any potential leaky expression in normoxic conditions and compared both 1% and 7.5% O<sub>2</sub> incubations with a 20% O<sub>2</sub> condition. Both HRE1x and HRIR circuits showed contrast on BURST only at 1% O<sub>2</sub> after seven days of doxycycline production, but the HRIR cells performed better, showing slightly

more than a 2-fold increase in hypoxic conditions when compared to the HRE1x cells (**Fig. 4-4B**). However, on xAM imaging, there was no significant difference between contrast produced at 1% O<sub>2</sub> (**Fig. 4-4C**). Importantly, on xAM, no contrast was produced at either 7.5% or 20% O<sub>2</sub>. These results suggest that transcriptional controls leveraging synthetic HRE promoters can enable distinguishing a hypoxic 1% O<sub>2</sub> environment and normoxic 7.5% O<sub>2</sub> environment.

#### 4.3.4 synNotch Induced Gas Vesicle Expression

In addition to sensing signals from extracellular cues like hypoxia, the ability to initiate GV response to extracellular antigen may also be useful in the setting of detecting solid tumors. The synNotch system was developed using the Notch receptor as a template in order to engineer cells with customizable sensing and response behaviors to extracellular cues.<sup>24</sup> We sought to leverage the anti-CD19 synNotch TetRVP64 transmembrane receptor to drive GV production specifically in THP-1 cells in contact with CD19 antigen expressing cells. This system would provide a proof-of-principle that monocytes can produce GVs when in contact with tumor-associated antigen.

The system we leveraged is similar to the previous 3P and HRE-GV expression systems (**Fig. 4-5A**). Anti-CD19 synNotch TetRVP64 is constitutively expressed and the tTA transactivator is released to initiate GV production once the anti-CD19 synNotch binds to CD19 antigen on another cell (**Fig. 4-5B**). As induction of this GV expression requires incubation with other CD19<sup>+</sup> bait cells, sorting out a pure population of successfully transduced THP-1 cells was challenging. As a result, the cells were sorted first only leaky expression resulting from non-specific synNotch cleavage and downstream transcriptional

activation. This increased the percentage of triple positive cells on flow cytometry, but we further increased the percentage of cells containing all three plasmids required for GV expression by reinfected this sorted population with each plasmid (**Fig. 4-S8**). Following reinfection, the induced cells showed improved in the percentage of cells containing all three plasmids (0.05% to 2.97%) and improved contrast with BURST imaging (2-fold increase over incubation with CD19<sup>-</sup> cells) (**Fig. 4-5A**). This result demonstrates the potential for controlling GV expression by interaction with cancer antigen.

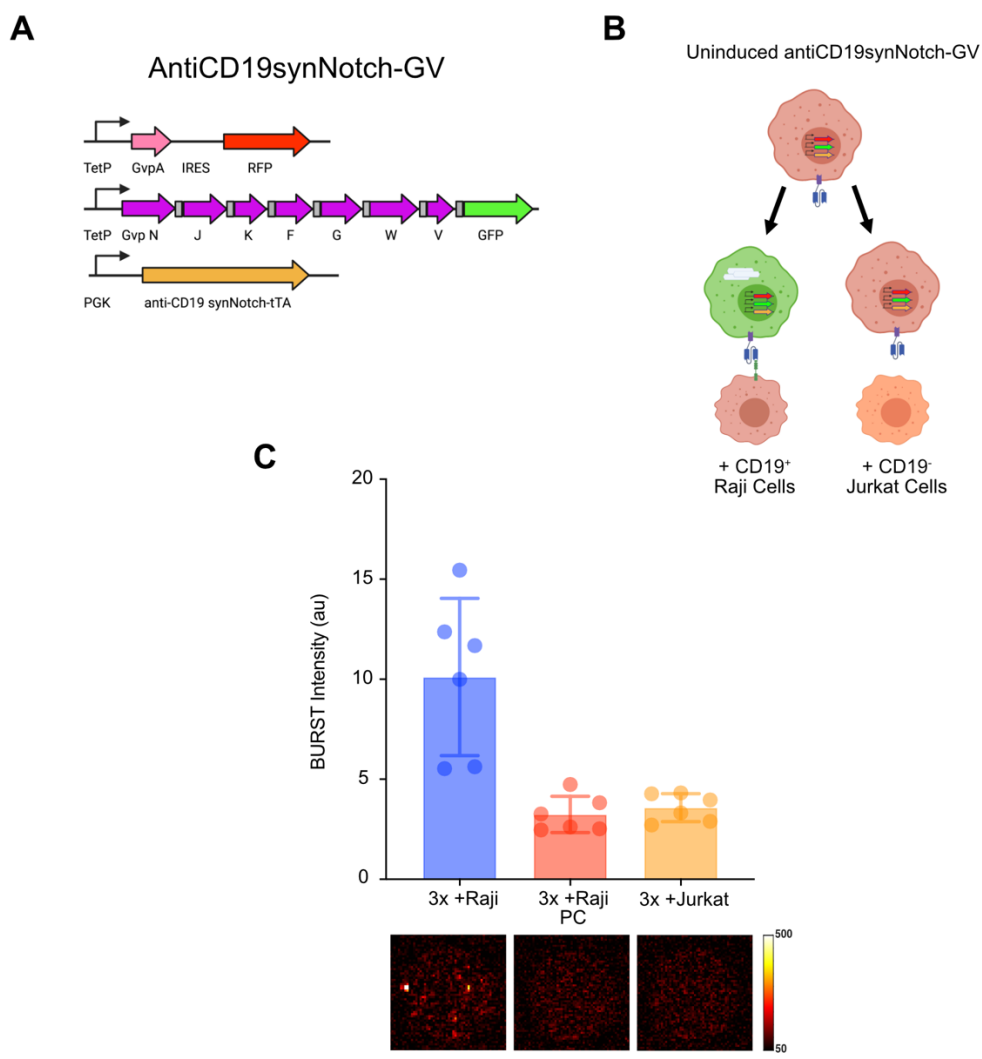


**Fig 4-5:** Developing antigen-inducible GV expression in THP-1 cells using the anti-CD19synNotch system **A)** Illustration of the viral construct being utilized utilizes a constitutively expressed the anti-CD19synNotch tTA where TetP activation is initiated upon synNotch engagement with the CD19 antigen. **B)** Diagram of antiCD19synNotch induced GV expression. (created with BioRender.com) **C)** BURST intensity quantification (top) of ultrasound imaging and representative BURST images (bottom) of cells transduced, sorted, and reinfected with antiCD19 synNotch and GV genes. These reinfected cells were coincubated with CD19<sup>+</sup> Raji cells or CD19<sup>-</sup> Jurkat cells at a 1:1 ratio for four days and loaded into phantoms at a concentration of 30M cells per mL. Post-collapse (PC) refers to BURST imaging conducted on the same frame after initial BURST imaging. Scale bar: 1mm.

#### 4.4 Discussion

Our results use the THP-1 monocyte cell line to establish proof of concept studies demonstrating that both monocytes and macrophages are capable of expressing GVs as cellular ultrasound contrast agents. Furthermore, monocytes can migrate in a 3µm transwell assay towards a chemokine while carrying intracellular GV cargo, and macrophages are capable of phagocytosis following expression of GV. These results suggest that GV expression does not abrogate critical cellular functions that may be useful in downstream applications leveraging GV expressing macrophages as ultrasound contrast agents.

Additionally, as gas vesicles are genetically encoded ultrasound contrast agents, their production can be transcriptionally controlled through a variety of methods. In this study, we demonstrate that GV production can be tethered to the machinery used by cells to sense low oxygen environments. GV expression can also be constrained to binding of extracellular antigen through the synNotch system. As a result, GV expression can be combined with mammalian cells' ability to sense and respond to environmental cues to molecularly confine ultrasound contrast production to these two cancer-associated signals.

While this study demonstrates the potential for immune cells to function as cellular ultrasound contrast agents, ultimately, these circuits and the effects of GV production will

need to be tested in primary monocytes. While using the THP-1 cell lines have widely been used to model monocyte function, testing these systems in monocytes will be required in order to further validate these technologies for translational purposes including *in vivo* testing.

## **4.5 Methods**

### **Plasmid Construction and Molecular Biology**

All plasmids were designed using SnapGene (GSL Biotech) and were assembled via reagents from New England Biolabs for KLD mutagenesis (E0554s) or Gibson Assembly (E2621L). Genes were subcloned into Lenti backbones as previously described. After assembly, NEB Turbo (C2984I) and NEB Stable (C3040I) E Coli were transformed for plasmid preparation. Plasmid was then isolated using the Promega PureYield™ Plasmid Midiprep System (A2492). Cloning primers and DNA sequences were synthesized by Integrated DNA Technologies. The 5xHRE-minCMV TATA (46926) anti-CD19 synNotch TetRVP64 (79126) plasmids were ordered from Addgene.

### **Cell Culture**

THP-1 (TIB-202) and Raji cells (CCL-86) were obtained from ATCC. They were cultured in RPMI 1640 media (Thermo Fischer Scientific) with 10% Tet tested FBS (R&D Systems, S10350) and 1x penicillin/streptomycin (Corning, 30-002-CI) or Supplemented RPMI 1640 media with 10% Tet tested FBS with 1x penicillin/streptomycin, 1x GlutaMAX (Thermo Fisher Scientific, 35050061), 1x MEM Non-Essential Amino Acids Solution (Thermo Fisher Scientific, 11140050), and 20 mM HEPES buffer (Gibco, 15630080). Unless otherwise stated, cells were cultured at 37°C, 5% CO<sub>2</sub> in a humidified incubator. Cells were sorted using the MACSQuant Tyto system when appropriate or analyzed with the MACSQuant VYB flow cytometer. Cell viability was determined using the SYTOX blue cell stain (Thermo Fischer, S34857) and subsequent flow cytometry.

### **Viral Transduction**

Lentivirus was prepared using a third-generation viral vector and packaging plasmids (gifts of D. Baltimore). HEK293T cells (ATCC, CLR-2316) were used for viral packaging. The HEK293T cells were cultured in DMEM (Corning, 10-013-CV) supplemented with 1x penicillin/streptomycin, 1x GlutaMAX, 1x MEM Non-Essential Amino Acids, and 20 mM HEPES buffer. Briefly, transfection mixtures were created by mixing 50 ug of plasmid with polyethyleneimine (Polysciences, 23966-2) at 2.58 ug PEI per ug of DNA. The mixture was incubated for 12 minutes at room temperature and added dropwise to HEK293T cells. PEI media was removed after 12 hours and replaced with fresh media supplemented with 10 mM sodium butyrate. After 8 hours, the sodium butyrate media was removed and replaced with 10mL of fresh DMEM. Virus was collected after 48 hours and concentrated using Lenti-X Concentrator (Takara Bio, 631231). Infection was performed using the Retronectin (Takara Bio, T100B) protocol. All experiments were performed at least 2 weeks after infection. Successful transduction was determined via flow cytometry.

### **GV Production and Imaging**

GV transduced THP-1 cells were induced with doxycycline (1000 ng/mL) for 12 hours and the brightest 0.5% RFP and GFP positive population was sorted and grown out. To initiate GV production, sorted cells were induced with doxycycline which was refreshed every other day. After 4 days of expression, cells were counted using the Countess 3 system (Thermo Fischer), and centrifuged at 150g for 5 minutes at room temperature. Cells were resuspended in 1% agarose (Bio-Rad) in PBS at 42°C at ~30 million cells/mL unless otherwise noted. The cell agarose mixture was then loaded into wells of preformed phantoms made of 1% agarose in PBS.

Phantoms were imaged using a L22-14vX transducer (Verasonics) on top of an acoustic absorber pad while submerged in PBS. BURST and xAM ramp imaging and image quantification was conducted as previously described. Briefly, the sample focus was set to 8mm, and for BURST imaging, the acoustic pressure was set to 1.6 V for the first 10 frames and 10V for the remaining frames. xAM ramps were acquired using the same parameters except the transducer voltage varied from 2 to 12V in 0.5V steps. Image quantification was

conducted using sample ROIs were drawn within the well and background ROIs were drawn around an empty region in the agarose phantom for SBR calculated. All xAM images were normalized and plotted on a dB scale.

### **THP-1 Migration, Differentiation, and Phagocytosis**

Chemotaxis was assayed in a 96-well transwell assay plate with 3µm pore size (Corning, 351161). Each well was coated with 100µg of fibronectin. THP-1 cells were cultured in complete RPMI media and induced with 1µg doxycycline to complete gas vesicle production. Cell concentration was adjusted to  $1 \times 10^6$  cells/mL in fresh RPMI and 50µL/well of the cell suspension was added into the upper compartment. The remaining cells were saved for ultrasound imaging. 200µL of 25nM MCP-1 (R&D, 279-MC-010) in RPMI was added to the bottom plate and the cell-containing insert was lowered into the plate containing chemoattractant. The plate was incubated overnight at 37°C, 5% CO<sub>2</sub> in a humidified incubator. Cells in the bottom compartment of 3 wells were used to obtain cell counts. The other 93 wells were pooled and counted. Cells from the original induced population were adjusted to match the total count of cells in the bottom plate following migration and both post-migration cells and unmigrated cells adjusted to the same cell count were taken for BURST and xAM imaging as described above.

Phorbol 12 myristate 13-acetate (PMA) was used to differentiate THP-1 cells into an adherent macrophage-like phenotype. THP-1 cells were cultured in RPMI supplemented with 500 ng/mL PMA for 2 days in tissue culture treated plates. The PMA supplemented RPMI was then removed and fresh RPMI. The cells were allowed to recover for two days before induction with doxycycline to initiate GV production. Following 4 days of induction, differentiated and undifferentiated THP-1 cells were adjusted to ~30 million cells/mL and taken for BURST and xAM imaging as described above.

To determine the capability of GV containing macrophages to carry out phagocytosis, THP-1 cells were differentiated using the protocol above and plated on fibronectin coated glass bottom dishes (MatTek, P35G-1.5-14-C) and induced with doxycycline. Following four days of induction, 2µm diameter BFP polystyrene beads

(Thermo Fischer, B0200) were added to the dishes and incubated with the cells for 24 hours. The cells were fixed with 2% PFA and taken for confocal imaging.

### **Hypoxia and Anti-CD19 synNotch Assay**

Synthetic circuits enabling HRE responsive GV production were cloned and transduced into THP-1 cells via lentivirus, induced with doxycycline at 1% O<sub>2</sub> for 24 hours before sorted as described above. These sorted cells were then grown out at 20% O<sub>2</sub>. Sorted cells were doxycycline induced at 1% and 7.5% O<sub>2</sub> and compared to a concurrent induction 20% O<sub>2</sub> for each condition for 7 days in supplemented RPMI at a concentration of 0.5 million cells/mL. Additional media equilibrated to 1%, 7.5% or 20% O<sub>2</sub> depending on experimental condition was added at day 4 to maintain a cell concentration of 0.5 million cells/mL. THP-1 cells were adjusted to ~30 million cells/mL and taken for BURST and xAM imaging as described above.

anti-CD19 synNotch TetRVP64 was transduced via lentivirus alongside GV genes into THP-1 cells. These cells were grown out, and without induction, were sorted on the brightest RFP and GFP population resulting from leaky synNotch activation. The sorted cells were grown and and reinfected with each plasmid in the system: anti-CD19 synNotch, GVpA, and GV chaperones. Cells were induced with CD19<sup>+</sup> Raji cells at a 1:1 ratio for 4 days before adjusting to ~30 million cells/mL for BURST and xAM imaging as described above.

## 4.6 Supplementary Figures

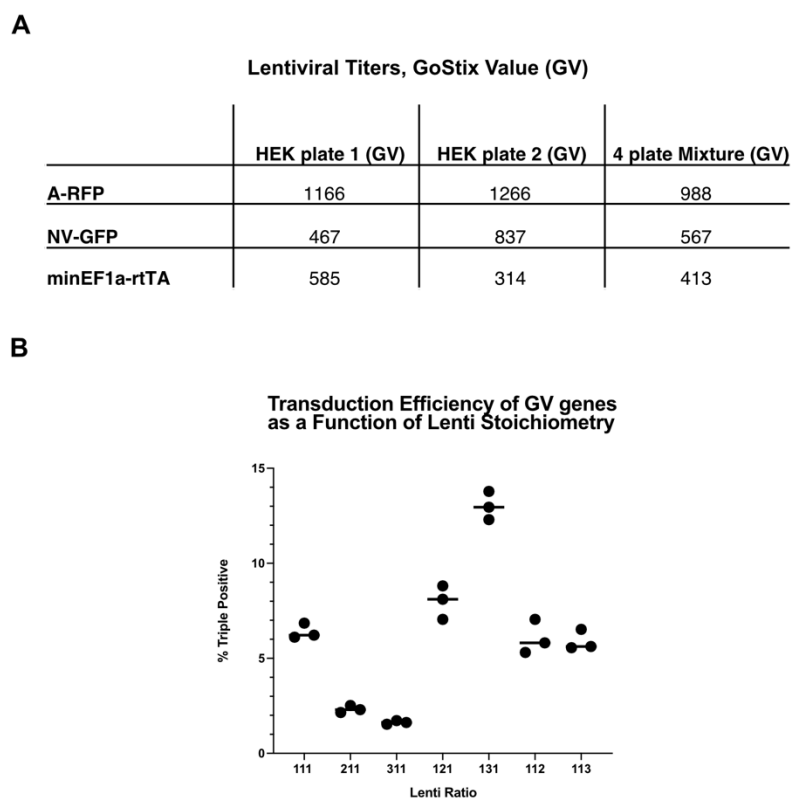


**Figure 4-S1:** Lentiviral titers to test effects of 3P transduction using varying plasmid stoichiometries. **A)** Titers resulting from lentiviral packing using a single 10-cm plate of HEK293T cells and a pool of 4 plates. **B)** Percentage of cells that are triple positive (RFP and GFP positive) on flow cytometry as a function of transduction using varying ratios of lenti. For labeling nomenclature, 1XX refers to the multiple of A-RFP, X1X refers to NV-GFP, and XX1 refers to minEFa-rtTA. For example, 131 THP-1 cells were transduced with lentivirus harvested from a single 10-cm plate of A-RFP and minEF1a-rtTA and three 10-cm plates of NV-GFP. By titer, this is roughly equivalent to a 2:3:1 ratio of A:NV:rtTA plasmids.

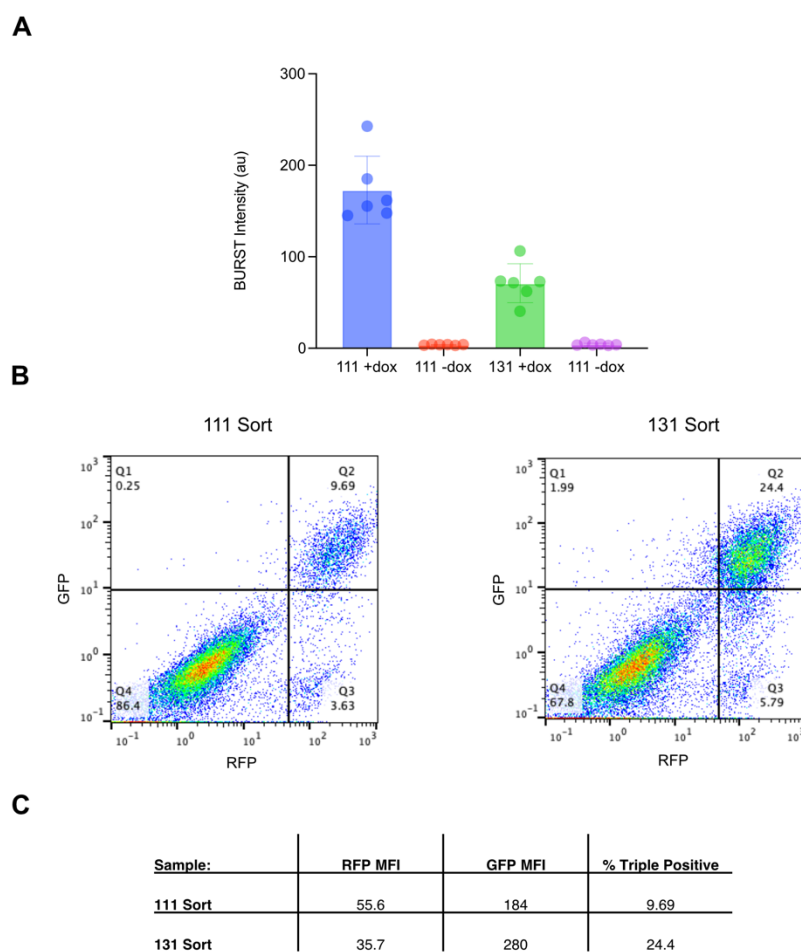


**Figure 4-S2:** Analysis on two of transduced THP-1 lines from **4-S1** including the brightest RFP cells (111) and highest percentage of triple positive cells (131). **A)** BURST intensity quantification to compare BURST contrast produced by sorted 111 and 131 cells for the brightest 0.25% triple positive population. **B)** RFP and GFP expression of 111 and 131 measured by flow cytometry. Imaging done using 30M cells/mL. **C)** RFP and GFP mean fluorescence intensity (MFI) and percentage triple positive cells of sorted 111 and 131 cells used for ultrasound imaging. N=6 technical replicates for ultrasound imaging. Where not seen, error bars ( $\pm$ SEM) are smaller than the symbol. By titer, this is roughly equivalent to a 2:3:1 ratio of A:NV:rtTA plasmids.

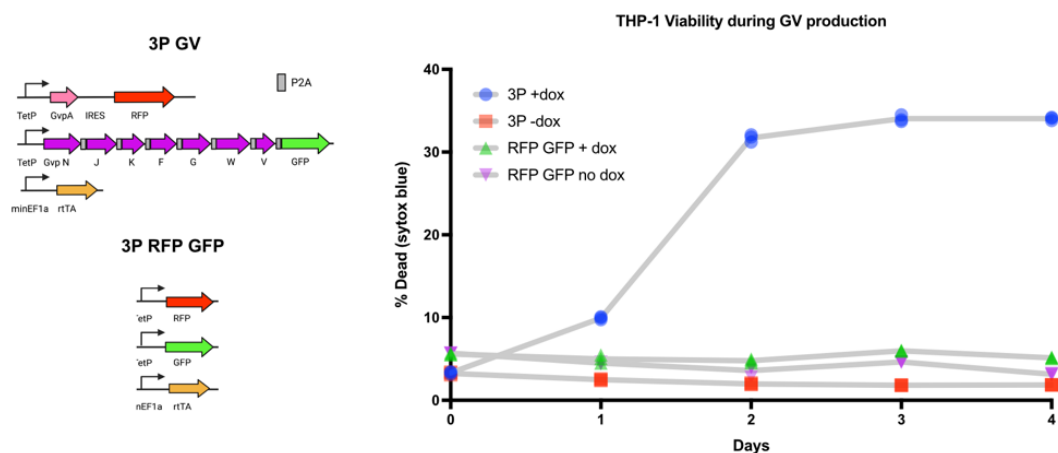


**Figure 4-S3:** Analysis of THP-1 viability during GV production. 3P GV and 3P RFP GFP transduced THP-1 cells were induced with doxycycline or PBS for 4 days and Sytox Blue nuclear stain was used to measure viability.

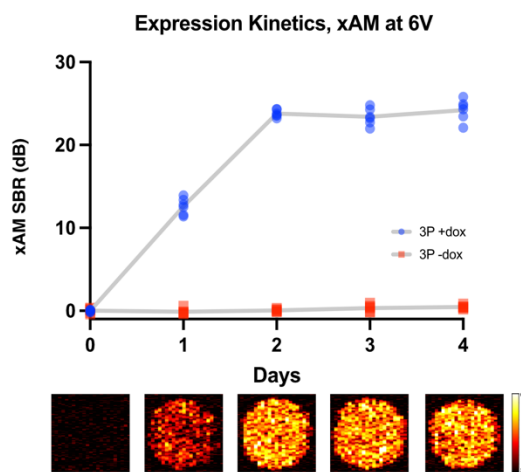


**Figure 4-S4:** Analysis of 3P THP-1 GV expression kinetics. SBR xAM quantification at 6V of doxycycline induced THP-1 cells at 6V were completed daily for 4 days (top) with representative images of xAM contrast at 6V (bottom). N=6. Where not seen, error bars ( $\pm$ SEM) are smaller than the symbol. Scale bar: 1mm.

### Migration Cell Counts

	Well 1	Well 2	Well 3	Estimated Total
+GV THP-1	2030	2620	2410	220,000
WT THP-1	1904	1237	1372	140,000

**Table 4-S1:** Representative cell counts taken from three wells of THP-1 cells containing GV (+GV) and WT THP-1 cells of the migration assay and estimated total migrated cells across the remaining 93 wells for both conditions

### GV Clusters Visible under Light Microscopy

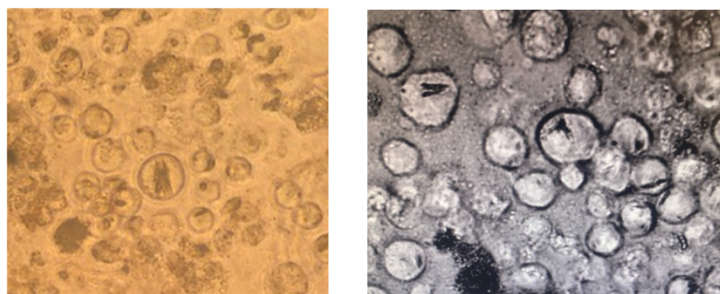


**Figure 4-S5:** Images of GV clusters visible under light microscopy. Scale bar: 10 $\mu$ m.

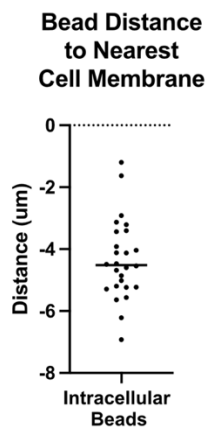


**Figure 4-S6:** Measured polystyrene bead distance from the nearest cell membrane inside the representative cell shown in Fig. 4-3D.

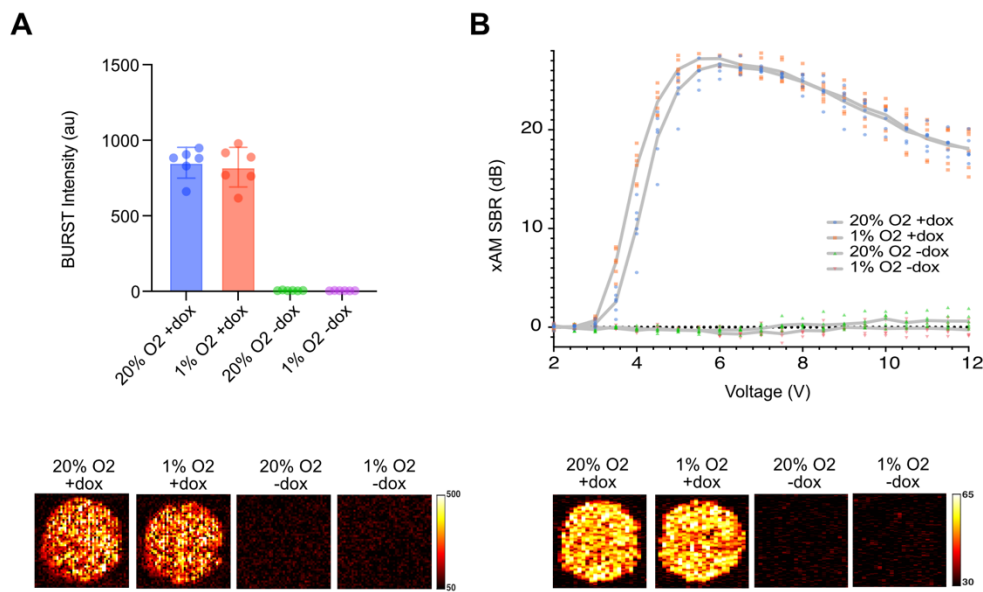


**Figure 4-S7:** Effects of hypoxia on GV expression and ultrasound contrast production in THP-1 cells. **A)** BURST intensity (top) and representative BURST images (bottom) of THP-1 cells induced and cultured in either 20% or 1% O<sub>2</sub>. **B)** SBR quantifications of xAM imaging at various voltages (top) and representative images of xAM contrast at 6V (bottom) of THP-1 cells induced and cultured in either 20% or 1% O<sub>2</sub>. N=6. Where not seen, error bars ( $\pm$ SEM) are smaller than the symbol. Scale bar: 1mm.

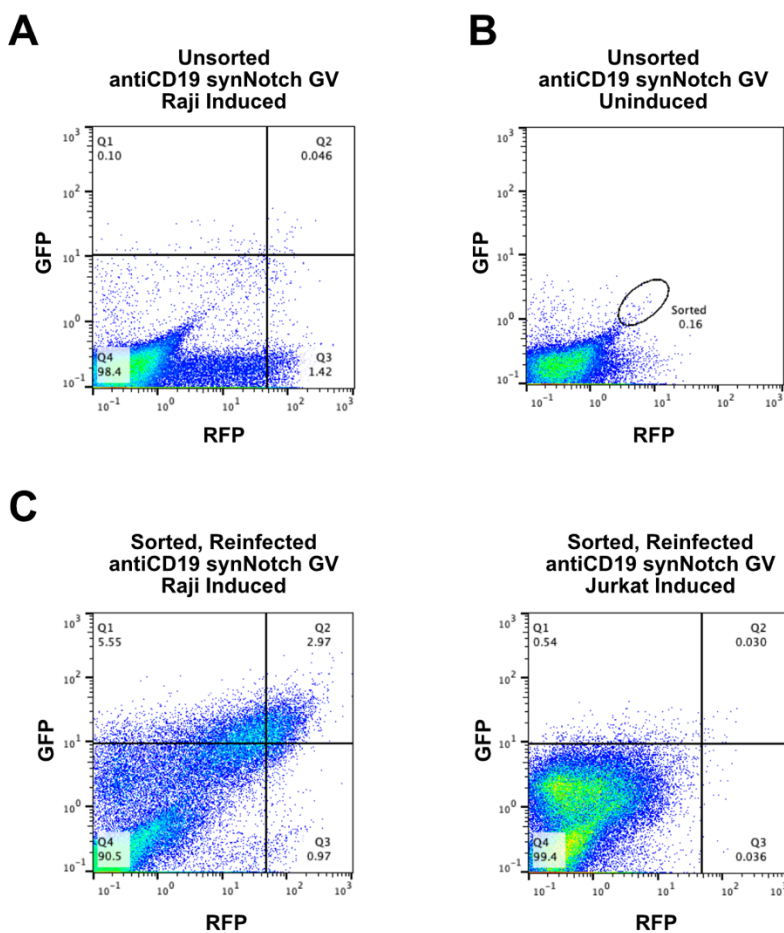


**Figure 4-S8:** Flow cytometry analysis of antiCD19-synNotch-tTA controlled GV expression before sorting and reinfection. **A)** RFP and GFP quantification of unsorted antiCD19-synNotch-tTA controlled GV expression following incubation with CD19<sup>+</sup> Raji cells for 4 days. **B)** Sorted population of uninduced antiCD19-synNotch-tTA controlled GV expression relying on non-specific, low level activation of synNotch. **C)** RFP and GFP quantification of antiCD19-synNotch-tTA controlled GV expression following sorting and reinfection with all three required plasmids and coincubation with CD19<sup>+</sup> Raji cells (left) and CD19<sup>-</sup> Jurkat cells (right).

## References

- 1.P Teixeira, A. & Fussenegger, M. Engineering mammalian cells for disease diagnosis and treatment. *Curr. Opin. Biotechnol.* **55**, 87–94 (2019).
- 2.Solinas, G., Germano, G., Mantovani, A. & Allavena, P. Tumor-associated macrophages (TAM) as major players of the cancer-related inflammation. *J. Leukoc. Biol.* **86**, 1065–1073 (2009).
- 3.Mantovani, A., Allavena, P., Marchesi, F. & Garlanda, C. Macrophages as tools and targets in cancer therapy. *Nat. Rev. Drug Discov.* **21**, 799–820 (2022).
- 4.Vinogradov, S., Warren, G. & Wei, X. Macrophages associated with tumors as potential targets and therapeutic intermediates. *Nanomed.* **9**, 695–707 (2014).
- 5.Duan, Z. & Luo, Y. Targeting macrophages in cancer immunotherapy. *Signal Transduct. Target. Ther.* **6**, 1–21 (2021).
- 6.Park, S.-M. *et al.* Molecular profiling of single circulating tumor cells from lung cancer patients. *Proc. Natl. Acad. Sci. U. S. A.* **113**, E8379–E8386 (2016).
- 7.Hori, S. S. & Gambhir, S. S. Mathematical Model Identifies Blood Biomarker-Based Early Cancer Detection Strategies and Limitations. *Sci. Transl. Med.* **3**, 109ra116 (2011).
- 8.Kwong, G. A. *et al.* Mass-encoded synthetic biomarkers for multiplexed urinary monitoring of disease. *Nat. Biotechnol.* **31**, 63–70 (2013).
- 9.Ronald, J. A., Chuang, H.-Y., Dragulescu-Andrasi, A., Hori, S. S. & Gambhir, S. S. Detecting cancers through tumor-activatable minicircles that lead to a detectable blood biomarker. *Proc. Natl. Acad. Sci. U. S. A.* **112**, 3068–3073 (2015).
- 10.Aalipour, A. *et al.* Engineered immune cells as highly sensitive cancer diagnostics. *Nat. Biotechnol.* **37**, 531–539 (2019).
- 11.Shapiro, M. G. *et al.* Biogenic gas nanostructures as ultrasonic molecular reporters. *Nat. Nanotechnol.* **9**, 311–316 (2014).
- 12.Farhadi, A., Ho, G. H., Sawyer, D. P., Bourdeau, R. W. & Shapiro, M. G. Ultrasound imaging of gene expression in mammalian cells. *Science* (2019) doi:10.1126/science.aax4804.
- 13.Hurt, R. C. *et al.* Genomically Mined Acoustic Reporter Genes Enable In Vivo Monitoring of Tumors and Tumor-Homing Bacteria. 2021.04.26.441537 <https://www.biorxiv.org/content/10.1101/2021.04.26.441537v2> (2021) doi:10.1101/2021.04.26.441537.
- 14.Sawyer, D. P. *et al.* Ultrasensitive ultrasound imaging of gene expression with signal unmixing. *Nat. Methods* **18**, 945–952 (2021).
- 15.Phys. Rev. X **8**, 041002 (2018) - Nonlinear X-Wave Ultrasound Imaging of Acoustic Biomolecules. <https://journals.aps.org/prx/abstract/10.1103/PhysRevX.8.041002>.
- 16.Geissmann, F. *et al.* Development of monocytes, macrophages and dendritic cells. *Science* **327**, 656–661 (2010).
- 17.Shi, C. & Pamer, E. G. Monocyte recruitment during infection and inflammation. *Nat. Rev. Immunol.* **11**, 762–774 (2011).
- 18.Tsuchiya, S. *et al.* Induction of Maturation in Cultured Human Monocytic Leukemia Cells by a Phorbol Diester1. *Cancer Res.* **42**, 1530–1536 (1982).
- 19.Muz, B., de la Puente, P., Azab, F. & Azab, A. K. The role of hypoxia in cancer progression, angiogenesis, metastasis, and resistance to therapy. *Hypoxia* **3**, 83–92 (2015).

20. Lee, P., Chandel, N. S. & Simon, M. C. Cellular adaptation to hypoxia through hypoxia inducible factors and beyond. *Nat. Rev. Mol. Cell Biol.* **21**, 268–283 (2020).
21. Wenger, R. H., Stiehl, D. P. & Camenisch, G. Integration of oxygen signaling at the consensus HRE. *Sci. STKE Signal Transduct. Knowl. Environ.* **2005**, re12 (2005).
22. Kaluz, S., Kaluzová, M. & Stanbridge, E. J. Regulation of gene expression by hypoxia: integration of the HIF-transduced hypoxic signal at the hypoxia-responsive element. *Clin. Chim. Acta Int. J. Clin. Chem.* **395**, 6–13 (2008).
23. Vordermark, D., Shibata, T. & Brown, J. M. Green Fluorescent Protein is a Suitable Reporter of Tumor Hypoxia Despite an Oxygen Requirement for Chromophore Formation. *Neoplasia N. Y. N* **3**, 527–534 (2001).
24. Morsut, L. *et al.* Engineering Customized Cell Sensing and Response Behaviors Using Synthetic Notch Receptors. *Cell* **164**, 780–791 (2016).

## CONCLUSIONS AND FUTURE DIRECTIONS

This thesis describes early efforts to expand the translational potential for both therapeutic and diagnostic ultrasound using synthetic biology strategies to engineer immune cells. Chapter 2 detailed the development and characterization of heat shock promoter (HSP)-controlled CAR or cytokine expression in primary T-cells. These genetic circuits unlock the potential to spatiotemporally control protein expression by using focused ultrasound heating as an energy signal to communicate with engineered T-cells. Chapter 3 describes initial attempts to create a macrophage-based ultrasound reporter cell. While phagocytosis of GV generated macrophages which produced ultrasound contrast, GV degradation by the phagolysosomal system proved more useful in potentially monitoring liver disease. In Chapter 4, we leveraged the ability to express gas vesicles in mammalian cells to engineer a monocyte ultrasound reporter cell line and characterized the ability of these monocytes to carry out critical functions while carrying intracellular GV cargo. We also developed genetic circuits to specifically activate GV expression in certain disease-associated contexts like hypoxia and presence of tumor antigen to illustrate the potential for a monocyte-based ultrasound cancer reporter.

While these works demonstrate the potential for using genetic engineering and synthetic biology to couple both therapeutic and diagnostic ultrasound to immune cell activation and cell state, tremendous work is required for further development of these technologies' translational potential. These challenges include broad outstanding obstacles

in synthetic biology including genetic circuit design considerations, the cost of immunotherapies and feasibility of immune cell-based diagnostic tools, and the need to test GV circuits in primary monocytes for further validation.

### **5.1 Genetic Circuit Design Considerations**

Designing genetic circuits has leveraged cells' innate ability to navigate their environments, sense surrounding signals, and respond through complex pattern of gene expression.<sup>1</sup> We are now able to program cells with novel capabilities like T-cells that alter gene expression in response to elevations in temperature or monocytes capable of producing ultrasound contrast agents in hypoxia. However, there are certain trade-offs that should be considered.

The first includes the use of tetracycline-controlled gene expression systems. Both Tet-Off and Tet-On gene expressions have been used in a variety of applications due to low background activity and strong activation in the presence of the tetracycline (Tet) effector.<sup>2</sup> Within the projects illustrated within this thesis, they successfully amplify weak promoters like HSPs and HREs into strong transcriptional activators through a 'feedforward' mechanism as the proteins of interest are controlled by the pTet promoter. Additionally, the Tet requirement for gene activation may benefit some applications as it serves as an additional pharmacologic control before protein production and masks leaky production of the gene of interest prior to drug activation. However, the potential obstacle includes additional consideration for the pharmacodynamics and pharmacokinetics of Tet administration *in vivo*. For example, in cancer applications where the cell of interest is to be activated in the tumor, the vasculature changes may decrease Tet available to activate transcription, and frequency of dosing to maintain circuit activation is a consideration.<sup>3</sup>

While other orthogonal strong transactivator systems like Gal4VP64 may be used to amplify cellular response from weak promoters, these do not benefit from the additional pharmacologic control which may be important when considering application where runaway circuit activation may lead to adverse outcomes.<sup>4</sup>

In addition, it is generally easier to decrease protein production. By using weaker Kozak sequences, decreasing multiplicity of infection, or changing upstream promoters, tuning down expression is possible.<sup>5,6</sup> However, increasing expression while maintaining tolerable levels of off-target expression is more challenging. For example, when evaluating the number of optimal HRE repeats to create a hypoxia sensitive promoter, a saturation effect was observed for vectors with more than five copies of HRE.<sup>7</sup> Other genes like the NDRG1 are inducible by a variety of environmental stressors including hypoxia, and the cis-elements inducible by hypoxia were identified. However, using these promoters in series with other HREs or in place of them may face issues with hypoxia specificity as the NDRG1 promoter was found to also activate in response to androgens and okadaic acid.<sup>8</sup> If greater protein production is required for downstream applications, promoter selection and circuit design should be carefully considered.

## **5.2 Cost Considerations for Adoptive Cell Transfer**

While engineered immune cell therapies like CAR T-cells have demonstrated remarkable outcomes, their current cost remains a significant barrier for using similar technologies for diagnosis and treatment for other therapies. The acquisition cost of a single CAR T-cell is between \$373,000 and \$475,000 per infusion.<sup>9</sup> While this includes the costs associated with T-cell harvesting, transduction, expansion and reinfusion, these therapies are administered in

inpatient settings due to monitoring requirements which incur additional costs.<sup>10</sup> And if there are serious adverse effects like life-threatening cytokine release syndrome (CRS), treatments costs continue to rise. Unfortunately, adverse events like CRS are not rare in the context of CAR T-cell immunotherapy. In the phase 1 and 2 clinical study of tisagenlecleucel, CRS occurred in 58 of 75 patients and 35 of these patients were admitted to the ICU for management.<sup>11</sup>

While addressing cost considerations and the ethical questions regarding value and affordability are outside the scope of the studies presented in this thesis, they remain important questions for consideration in both the development of therapeutic and diagnostic immune cells. Multiple approaches are being explored to decrease costs including the development of ‘off-the-shelf’ allogeneic immune therapies manufactured from donor cells as opposed to patients’ own cells.<sup>12</sup> The potential for scaled-up manufacturing process where a high number of CAR T-cells may be produced from a single donor and cryopreserved to make treatments immediately available would decrease costs. The major obstacle for this therapy is graft-versus-host disease (GVHD) where HLA mismatches between donor and recipient trigger immune recognition leading to graft rejection. Gene editing immunogenic receptors on the surface of donor cells may decrease the potential for GVHD, but this remains an active area of research and an critical innovation for widespread use of adoptive cell transfer for disease detection and treatment.<sup>13</sup>

### **5.3 Future Directions for Monocyte-based Ultrasound Reporter Cells**

THP-1 cells were used as a model for GV production in a human monocyte. This cell line was originally isolated from the peripheral blood of a 1-year old male patient suffering from

acute monocytic leukemia.<sup>14</sup> Studies demonstrate similarities between THP-1 cells and primary monocytes and macrophages in both morphology and functional properties including differentiation markers and has been used extensively to study both monocyte and macrophage function *in vitro*.<sup>15-18</sup> THP-1 cells are an important model cell line as there may be feasibility or financial contrasts to using primary monocytes for study. PBMC-derived monocytes cannot be stocked in liquid nitrogen and require inflammatory mediators like L-1 $\beta$ , TNF- $\alpha$  or LPS to prevent apoptosis in culture.<sup>19</sup> While THP-1 cells have been widely characterized and used, to truly determine translational potential of GV-expressing monocytes as ultrasound reporters for disease, testing in PBMC derived monocytes will be required.

Gene transfer into primary human macrophages has been historically challenging, but with increasing interest in using monocytes as immunotherapies, replication-incompetent chimeric adenoviral vectors have been developed and used to successfully transduce primary human macrophages.<sup>20</sup> Validation of GV expression in primary monocytes remains an important step in increasing translational potential. Furthermore, to our knowledge, THP-1 cells have not been used for *in vivo* monocyte migration studies to tumor stroma. However, both primary mouse and human monocytes have been studied in syngeneic and xenograft models.<sup>20,21</sup> These studies suggest that primary monocytes are capable of penetrating and accumulating in tumors, but combining this tumor accumulation of macrophages with GV expression and subsequent ultrasound construct production is a critical next step.

While more research will be required to realize the potential of monocytes as ultrasound reporters for disease detection, this work demonstrates the new possibilities for noninvasive disease diagnosis. Continued development of GV expression in mammalian systems will

unlock new avenues of leveraging ultrasound imaging to improve human health and the work presented here is an exciting first step towards realizing noninvasive immune cell-based cancer diagnostic tools.

## References

1. Ausländer, S. & Fussenegger, M. Engineering Gene Circuits for Mammalian Cell-Based Applications. *Cold Spring Harb. Perspect. Biol.* **8**, a023895 (2016).
2. Das, A. T., Tenenbaum, L. & Berkhout, B. Tet-On Systems For Doxycycline-inducible Gene Expression. *Curr. Gene Ther.* **16**, 156–167 (2016).
3. Azzi, S., Hebda, J. K. & Gavard, J. Vascular Permeability and Drug Delivery in Cancers. *Front. Oncol.* **3**, 211 (2013).
4. Roybal, K. T. *et al.* Engineering T Cells with Customized Therapeutic Response Programs Using Synthetic Notch Receptors. *Cell* **167**, 419–432.e16 (2016).
5. Ferreira, J. P., Overton, K. W. & Wang, C. L. Tuning gene expression with synthetic upstream open reading frames. *Proc. Natl. Acad. Sci.* **110**, 11284–11289 (2013).
6. Huang, D., Kosentka, P. Z. & Liu, W. Synthetic biology approaches in regulation of targeted gene expression. *Curr. Opin. Plant Biol.* **63**, 102036 (2021).
7. Shibata, T., Giaccia, A. J. & Brown, J. M. Development of a hypoxia-responsive vector for tumor-specific gene therapy. *Gene Ther.* **7**, 493–498 (2000).
8. Zhang, P., Tchou-Wong, K.-M. & Costa, M. Egr-1 mediates hypoxia-inducible transcription of the NDRG1 gene through an overlapping Egr-1/Sp1 binding site in the promoter. *Cancer Res.* **67**, 9125–9133 (2007).
9. Fiorenza, S., Ritchie, D. S., Ramsey, S. D., Turtle, C. J. & Roth, J. A. Value and affordability of CAR T-cell therapy in the United States. *Bone Marrow Transplant.* **55**, 1706–1715 (2020).
10. Lyman, G. H., Nguyen, A., Snyder, S., Gitlin, M. & Chung, K. C. Economic Evaluation of Chimeric Antigen Receptor T-Cell Therapy by Site of Care Among Patients With Relapsed or Refractory Large B-Cell Lymphoma. *JAMA Netw. Open* **3**, e202072 (2020).
11. Maude, S. L. *et al.* Tisagenlecleucel in Children and Young Adults with B-Cell Lymphoblastic Leukemia. *N. Engl. J. Med.* **378**, 439–448 (2018).
12. Depil, S., Duchateau, P., Grupp, S. A., Mufti, G. & Poirot, L. ‘Off-the-shelf’ allogeneic CAR T cells: development and challenges. *Nat. Rev. Drug Discov.* **19**, 185–199 (2020).
13. Torikai, H. *et al.* A foundation for universal T-cell based immunotherapy: T cells engineered to express a CD19-specific chimeric-antigen-receptor and eliminate expression of endogenous TCR. *Blood* **119**, 5697–5705 (2012).
14. Tsuchiya, S. *et al.* Establishment and characterization of a human acute monocytic leukemia cell line (THP-1). *Int. J. Cancer* **26**, 171–176 (1980).
15. Hjort, M. R. *et al.* Alveolar Epithelial Cell-Macrophage Interactions Affect Oxygen-Stimulated Interleukin-8 Release. *Inflammation* **27**, 137–145 (2003).
16. Kramer, P. R. & Wray, S. 17- $\beta$ -Estradiol regulates expression of genes that function in macrophage activation and cholesterol homeostasis. *J. Steroid Biochem. Mol. Biol.* **81**, 203–216 (2002).
17. Sakamoto, H. *et al.* Biomechanical Strain Induces Class A Scavenger Receptor Expression in Human Monocyte/Macrophages and THP-1 Cells. *Circulation* **104**, 109–114 (2001).
18. Tsuchiya, S. *et al.* Induction of Maturation in Cultured Human Monocytic Leukemia Cells by a Phorbol Diester. *Cancer Res.* **42**, 1530–1536 (1982).

19. Mangan, D. F., Welch, G. R. & Wahl, S. M. Lipopolysaccharide, tumor necrosis factor-alpha, and IL-1 beta prevent programmed cell death (apoptosis) in human peripheral blood monocytes. *J. Immunol. Baltim. Md 1950* **146**, 1541–1546 (1991).
20. Klichinsky, M. *et al.* Human chimeric antigen receptor macrophages for cancer immunotherapy. *Nat. Biotechnol.* **38**, 947–953 (2020).
21. Combes, F., McCafferty, S., Meyer, E. & Sanders, N. N. Off-Target and Tumor-Specific Accumulation of Monocytes, Macrophages and Myeloid-Derived Suppressor Cells after Systemic Injection. *Neoplasia N. Y. N* **20**, 848–856 (2018)